

# 学位論文

Study of Resonance Crossing in Strong Focusing Accelerators

強収束加速器における共鳴横切りに関する研究

平成16年12月 博士（理学）申請

東京大学大学院理学系研究科

物理学専攻

相場 政光





## Contents

Abstract .....	1
1 Introduction.....	2
1.1 Background of the study, FFAG accelerator .....	2
1.2 Purpose of the study .....	3
1.3 Resonance crossing in 150MeV proton FFAG.....	4
1.4 Organization of the paper.....	5
2 Dynamics of resonance crossing .....	6
2.1 Betatron oscillation.....	6
2.1.1 Betatron oscillation and resonance .....	6
2.1.2 Driving term of resonance .....	7
2.2 Resonance crossing .....	7
2.2.1 Variation of betatron tune .....	7
2.2.2 General discussion on major parameters .....	8
2.3 Crossing without nonlinear detuning .....	8
2.4 Crossing with nonlinear detuning.....	10
2.4.1 “Particle trapping” .....	10
2.4.2 Reverse crossing.....	16
3 Beam studies .....	20
3.1 Resonance Crossing Experiment at PoP FFAG.....	20
3.1.1 PoP.....	20
3.1.2 Remodeling of magnet .....	23
3.1.3 Betatron tune measurement .....	24
3.1.4 Longitudinal beam handling .....	27
3.1.5 Driving term and nonlinear detuning.....	28
3.1.6 Beam injection .....	31
3.1.7 COD confirmation.....	34
3.1.8 Measurement of beam before and after crossing.....	35
3.1.9 Data analysis .....	35
3.1.10 Beam emittance just before crossing .....	38
3.1.11 Results.....	40
3.2 Resonance crossing experiment at HIMAC synchrotron .....	46
3.2.1 HIMAC Accelerator.....	46
3.2.2 Observation of beam profile .....	47
3.2.3 Driving term and nonlinear detuning source .....	47
3.2.4 Tune variation.....	48
3.2.5 Parameters for the beam study .....	48
3.2.6 Experimental results .....	49

4	Discussion and Conclusion .....	52
4.1	Discussion on experimental results at PoP FFAG.....	52
4.2	Discussion on experimental results at HIMAC .....	65
4.3	Conclusions .....	75
	Acknowledgements.....	77
	Bibliography .....	78
	Appendix.....	80
A	Overview of 150MeV FFAG synchrotron .....	80
B	Particle tracking in three-dimensional magnetic field.....	96
C	Driving term and nonlinear detuning.....	98
D	Beam loss due to residual gas in PoP FFAG.....	101
E	Particle tracking with tune varying transfer matrix .....	104



## Abstract

We have studied beam dynamics of resonance crossing for further development of FFAG accelerators. FFAG has in principle constant betatron tunes with a scaled radial dependence of the magnetic field having nonlinear components. However, betatron tunes slightly change and may cross resonance because it is very hard to make perfect magnetic field. Once we give up constant tunes, different designs of FFAG become possible. Those machines are called non-scaling FFAG in contrast to the original scaling FFAG. For both scaling and non-scaling FFAG, resonance crossing, which has not been studied sufficiently in past, has become an important issue of beam dynamics.

Generally speaking, beam dynamics of resonance crossing has been treated in a rather crude manner regardless of whether nonlinear detuning i.e., the dependence of betatron tunes on the oscillation amplitudes is significant or not. In FFAG, one should be more concerned about resonance crossing with dominant nonlinear detuning. A.W. Chao and M. Month have proposed a model of “particle trapping” in which some particles of a beam are trapped and transported to large amplitudes through resonance crossing when nonlinear detuning is dominant. However, there was no experimental confirmation of this phenomenon for a long time. We have observed particle trapping in detail and also investigated a crossing in which tune crosses in the reverse direction of particle trapping.

With analytical approaches, we discuss details of particle trapping and reverse crossing. An analytical expression of possible emittance growth in reverse crossing is developed in this study quantitatively for the first time. Beam studies of resonance crossing have been performed in PoP FFAG and HIMAC synchrotron. The ones in this paper and another at CERN-PS carried out at about the same time are the first experimental observations of particle trapping. In PoP beam study, trapping efficiency, that is, the ratio of trapped particle for various parameters are obtained. In HIMAC experiment, we have observed the difference due to crossing direction.

We discuss several factors relevant to trapping efficiency including the effects of two-dimensional transverse motion and longitudinal motion that are not included in the original model of particle trapping. The results for trapping efficiency by the beam study and tracking simulation show a good agreement. Furthermore, we have observed that no particle is trapped when crossing speed is fast enough. It has become evident that reverse crossing is less critical than particle trapping since trapped particles are eventually lost finally whereas reverse crossing results in emittance growth only. Through this study, we are convinced that it is possible to cross resonance without considerable damage when the parameters are appropriate.

In this work, I developed an analytical expression for reverse crossing. And I planned beam studies and acquired data with the collaborator’s helping. The experimental data were analyzed by myself.

# **Chapter 1**

## **Introduction**

### **1.1 Background of the study, FFAG accelerator**

FFAG (Fixed Field Alternating Gradient) focusing scheme was originally proposed by Ohkawa in 1953 [ 1 ], a short time after the discovery of strong focusing by Christofilos, Courant, Livingston and Snyder[ 2 ][ 3 ]. At that time, FFAG was studied and two model machines of electron FFAG accelerator were constructed in MURA project [ 4 ]. FFAG accelerator has in principle constant tunes since scaling law is satisfied with nonlinear field components [ 5 ]. However, it is very hard to make perfect magnetic field satisfying scaling law in practice because of strong nonlinear components. Then betatron tunes slightly change and may cross resonance during acceleration. On the other hand, different designs of FFAG become possible once we give up constant tunes. Those machines are called non-scaling FFAG in contrast to the original scaling FFAG. By abandoning constant tunes, other advantages are obtained such as nearly isochronous and flexibility of optics design. For this new type of FFAG, resonance crossing has become an important issue of beam dynamics.

FFAG had not been constructed for a long time after MURA project. One reason is technical difficulties of those days and this will be discussed later. Another reason for giving up FFAG is that synchrotrons are better suited as high-energy accelerators. However, nowadays, there are high demands not only for high-energy accelerators but also for high power machines, especially for industrial applications, energy productions, and so on. High repetition pulsed beam is also demanded for new technique of charged beam cancer therapy [ 6 ].

In comparison with synchrotrons, FFAG has a definite advantage as the one for high power beams because of its rapid cycling capability. In fact, a repetition rate of FFAG is not limited by ramping time of magnet as in synchrotrons. It is determined by the available rfc voltage. Cyclotrons have also fixed field and its DC beam current is very high. For a few hundred MeV proton beam, cyclotron must be superior as high power machine than other circular accelerators. However, it is hard to construct a higher energy cyclotron because of its magnet size if the isochronous property is to be maintained. FFAG, on the other hand, is available in all energy regions because of the

synchrotron acceleration. The size of FFAG magnets is modest compared with cyclotrons since alternating gradients of magnetic field are used to realize strong focusing. In summary, FFAG utilizes both advantages of synchrotron and cyclotron.

When FFAG was proposed, there were mainly two technical problems. One was to construct the magnetic field of FFAG focusing with sufficient accuracy. The other was a problem associated with rf cavity that must have a large aperture due to the orbit shift in FFAG. Furthermore, a high gradient rf field is desirable in order to take advantage of FFAG accelerator, i.e. rapid cycling. When a repetition rate is very high, it is difficult to change resonant frequency of cavity rapidly. Therefore a cavity must be broadband since the revolution frequency of low energy proton or heavy ion beams changes in a wide range.

These problems are resolved with technical advances in recent years. Three-dimensional field calculations are now possible because of the recent advance in computer technology. Furthermore, a broadband and high gradient rf cavity using magnetic alloy core (MA core) has been developed [ 7 ]. These factors allowed the construction of the world's first proton FFAG accelerator, PoP FFAG synchrotron [ 8 ]. It was built at KEK in 2000 and demonstrated fast acceleration of proton beam from 50keV to 500keV within 1ms. With the success of PoP FFAG synchrotron, several projects to construct FFAG accelerators are now in progress [ 9 ][ 10 ][ 11 ].

FFAG accelerator should be useful not just a tool for high intensity beams but also for particles having very short lifetime as muons. Fixed magnetic field enables a very fast acceleration within particle lifetime. In order to realize neutrino factory based on a muon FFAG accelerator, design studies of scaling and non-scaling muon FFAG [ 12 ] have been undertaken. The beam dynamics of resonance crossing has become an important subject also for this application of FFAG accelerator.

## 1.2 Purpose of the study

Since having constant tune is the basic strategy to avoid resonance, beam dynamics of resonance crossing was not essence in past accelerator development and it has not been studied sufficiently. Therefore, criteria for allowable effect on beam due to resonance crossing are not clear. That is, how fast crossing speed should be, how much driving term is permitted, and so on. The purpose of the study is to clarify these points, specifically for resonance crossing in FFAG accelerator.

Resonance crossing in circular accelerator seems rare. However, in cyclotron, a beam must cross resonances to be accelerated up to relativistic regions. There is one experimental study of resonance crossing in cyclotron by R. Baartman et al., in Ref. [ 13 ]. It details with a half integer resonance crossing.

We can find some analytical studies, by Lysenko, Sturrock and Guignard in Ref.

[ 14 ], [ 15 ] and [ 16 ] respectively, to find an expression of the maximum amplitude growth through resonance crossing. One common feature in these works is that the maximum amplitude growth is expressed by a scaling parameter driving-term divided by  $\text{sqrt}(\text{crossing speed})$ . This is confirmed experimentally in Ref.[ 13 ] for half integer resonance and by recent studies by Machida for third integer resonance in Ref.[ 17 ].

In these studies, the effect of nonlinear detuning i.e., the dependence of betatron tunes on the oscillation amplitudes is regarded as negligible since it is not strong in cyclotrons or synchrotrons. However, a nonlinear detuning should be considered in FFAG accelerator since nonlinear component of magnetic field is significant. Even if non-scaling FFAG ring is composed of linear elements only, fringing field may introduce nonlinear component because particle orbit changes during acceleration in fixed magnetic field and does not cross magnet edges perpendicularly anymore. Then we must take into account the effect of nonlinear detuning.

Chao and Month proposed a model for resonance crossing with nonlinear detuning in Ref.[ 18 ]. They showed an idea of “particle trapping” in which a part of beam particles is trapped and transported to infinite amplitude through resonance crossing when nonlinear detuning is dominant. They also developed an analytical expression for trapping efficiency. However, there was no experimental confirmation of “particle trapping” phenomenon for a long time. The beam studies in this paper and another study at CERN-PS in Ref.[ 19 ] performed at about the same time are the first experimental observation of “particle trapping”. But the latter is for beam extraction technique in synchrotrons. Therefore the motivation of the study is quite different from ours. We must understand “particle trapping” experimentally including many factors for real accelerator and confirm that there is no trapped particle when crossing speed is fast enough.

It will be also evident from our study that “particle trapping” occurs only in one crossing direction and a crossing in reverse direction leads to another phenomenon. Crossing in reverse direction was discussed by Sturrock only. Although his observation on the reverse crossing is qualitatively correct, it may cause a misunderstanding and this has been clarified in this work by simulation as well as by experimental observation.

### 1.3 Resonance crossing in 150MeV proton FFAG

Resonance crossing in a 150MeV proton FFAG is also discussed. After the success of PoP FFAG, this machine has been constructed at KEK to investigate the possibility for practical use. During commissioning machine studies, we have experienced an unexpected third integer resonance crossing. However, from the present study, we found that its effect on the beam is negligible. The machine construction and commissioning study as well as its third integer resonance crossing are described in Appendix A.

## **1.4 Organization of the paper**

In Chapter 2, beam dynamics of resonance crossing is discussed. In Chapter 3, beam experiments at PoP FFAG and HIMAC synchrotron are described. In Chapter 4, results of beam studies are discussed together with simulation and theoretical predictions. Finally, the summary of the main conclusions of this study is presented.

## Chapter 2

# Dynamics of resonance crossing

In this chapter, we discuss dynamics of resonance crossing. In Sec.2.1, betatron oscillation, resonances and its driving terms are introduced. In Sec.2.2, general considerations of the resonance crossing are presented. In Sec.2.3 and Sec.2.4, resonance crossing with or without nonlinear detuning is considered respectively.

### 2.1 Betatron oscillation

#### 2.1.1 Betatron oscillation and resonance<sup>1</sup>

In alternating gradient focusing, linear transverse motion is expressed by Hill's equation,

$$z'' + K(s)z = 0, \quad (2-1)$$

where  $z$  is the transverse coordinate,  $z''$  denotes the second derivative of  $z$  with respect to the orbit length  $s$  and  $K(s)$  is the coefficient of focusing force. In Eq.( 2-1 ), it is assumed that  $z'^2 \ll 1$ .

Here  $K(s)$  satisfies periodic condition,

$$K(s) = K(s + 2\pi R), \quad (2-2)$$

where  $R$  is the equivalent radius of ring, which is defined as the pass length divided by  $2\pi$ . Furthermore when a ring has super-periodicity, a more restrictive condition is imposed,

$$K(s) = K(s + L), \quad (2-3)$$

where  $L$  is the orbit length of a super-period.

It is well known that a solution of Hill's equation can be written as

---

<sup>1</sup> There are many textbooks, for instance [ 20 ] and [ 21 ].

$$z(s) = \sqrt{2J\beta(s)} \cos(\phi(s) + \delta), \quad (2-4)$$

where  $J$  is the amplitude constant of oscillation,  $\beta(s)$  is the beta function of Courant-Snyder,  $\phi(s)$  is the phase advance and  $\delta$  is the initial phase. An oscillation expressed by Eq.( 2-4 ) is the betatron oscillation.

Betatron tune is defined as the number of oscillations per revolution, i.e.

$$\nu = \frac{\phi(2\pi R) - \phi(0)}{2\pi} = \oint \frac{ds}{\beta(s)}. \quad (2-5)$$

Actually, transverse motion has two degrees-of-freedom, horizontal and vertical, so that beta function and betatron tune are defined in each direction unless the motion is linearly coupled. In general, motion may not be stable if tunes satisfy the following condition,

$$m\nu_x + n\nu_y = p, \quad (2-6)$$

where subscripts  $x$  and  $y$  denote the horizontal and vertical motion respectively, while  $m, n$  and  $p$  are positive or negative integers including zero. This is called resonance and it is excited when driving term exists as described in the next subsection.

### 2.1.2 Driving term of resonance

In an ideal machine with superperiod  $N$ , there is no resonance unless  $p$  in Eq.( 2-6 ) is either zero or multiples of  $N$ , the so-called structural resonance. In real machines, constructional errors and other factors are unavoidable so that resonances with any integer value of  $p$  will be excited. For instance, third integer resonance  $3\nu_x=p$  is excited by a driving term of the form

$$G_{3,0,p} \exp(i\eta) = \frac{\sqrt{2}}{24\pi} \oint \beta_x(s)^{3/2} S(s) \exp\{i[3\phi_x(s) - (3\nu_x - p)\theta]\} ds, \quad (2-7)$$

where  $G_{3,0,p}$  is the Fourier amplitude of driving term,  $S(s)$  is proportional to the strength of sextupole field,  $\beta_x(s)$  is the horizontal beta function,  $\theta$  is the azimuthal angle,  $\eta$  is the phase factor and  $\phi_x(s)$  is the phase advance of horizontal betatron oscillation.

## 2.2 Resonance crossing

### 2.2.1 Variation of betatron tune

When a focusing strength  $K(s)$  is constant in time, tunes are also constant. In alternating gradient synchrotron, a focusing strength is kept effectively constant because magnetic field is increased proportionally to increased momentum of the beam during

acceleration. However, once the focusing force changes, tunes also change as a consequence and may cross a resonance. Here, we confine our consideration of resonance crossing to FFAG. Unlike in synchrotron, beam orbit in FFAG moves radially outward or inward during acceleration since magnetic field is constant in time, but the focusing strength does not change in time when scaling law is satisfied, keeping tunes constant for all momentum. However, when it is violated unexpectedly or intentionally, focusing strengths for different momentum particles are not the same and tunes are varied during acceleration.

As described above, the cause of the change in focusing strength is different between synchrotron and FFAG. Nevertheless, the dynamics of resonance crossing is essentially the same in any circular accelerators.

### 2.2.2 General discussion on major parameters

Crossing speed, driving term, nonlinear detuning and beam emittance are the major parameters in beam dynamics of resonance crossing. It is generally believed that faster crossing and weaker driving term decreases a damage to beam. Obviously, these two parameters must be treated together. That is, even if driving term is large, damage is not considerable when crossing is fast enough. We consider crossing that may cause an acceptable beam loss or a small change in the beam emittance only, since it may not make sense to discuss a crossing in which damage is critical. Nonlinear detuning, i.e. the dependence of betatron tune on the oscillation amplitude, changes dynamics of crossing drastically since it works as a stabilizing term that makes sufficiently small amplitude motion always stable. When nonlinear detuning is introduced to be dominant, a variation of phase space topology becomes relatively slow. For instance, the fixed points in phase space move slowly when nonlinear detuning is strong. (Eq.( 2-43 ) shows this.) Then a quasi-static treatment may be applicable. Beam emittance and distribution of particles are also significant parameters in nonlinear resonance because motion of particle depends on its oscillation amplitude in the existence of nonlinear components of field. Two cases, one with dominant nonlinear detuning and another without, will be discussed. In FFAG, we should be more concerned about resonance crossing with dominant nonlinear detuning.

## 2.3 Crossing without nonlinear detuning

We start the discussion with one-dimensional motion and exclude non-linear detuning. The maximum growth of betatron amplitude due to resonance crossing can be obtained with integration of Hamiltonian equations of motion. The analytical treatment given

below is based on references [ 13 ] and [ 16 ].

Specifically, a resonance  $m\nu_x=p$  is treated. It is one-dimensional uncoupled resonance excited by  $m$ -th order of  $p$ -th harmonic driving term. When driving term exists, Eq.( 2-1 ) becomes

$$x'' + \nu_x^2 x = -mG_{m,0,p}x^{m-1} \cos(p\theta + \eta) , \quad (2-8)$$

where  $x''$  denotes the second derivative of  $x$  with respect to the azimuthal angle  $\theta$ .

Hamiltonian for this is

$$H = \frac{p^2}{2} + \frac{\nu_x^2 x^2}{2} + G_{m,0,p}x^m \cos(p\theta + \eta) , \quad (2-9)$$

where  $x$  and  $p$  are a pair of canonical variables.

With a canonical transformation from  $(x, p)$  to action-angle  $(J, \psi)$ , Hamiltonian is transformed as

$$H = \nu_x J + G_{m,0,p} \left( \frac{2J}{\nu_x} \right)^{m/2} \cos^m \psi \cos(p\theta + \eta) , \quad (2-10)$$

where

$$x = \sqrt{2J/\nu_x} \cos \psi , \quad (2-11)$$

$$p = -\sqrt{2J\nu_x} \sin \psi . \quad (2-12)$$

Hamilton's equations of motion are obtained with Eq.( 2-10 ),

$$\psi' = \frac{\partial H}{\partial J} = \nu_x + \text{fast varying terms} , \quad (2-13)$$

$$J' = -\frac{\partial H}{\partial \psi} = mG_{m,0,p} \left( \frac{2J}{\nu_x} \right)^{m/2} \cos^{m-1} \psi \sin \psi \cos(p\theta + \eta) . \quad (2-14)$$

For a linear variation of the tune, we have

$$\nu(\theta) = \nu_{x0} + \frac{\varepsilon\theta}{2\pi} , \quad (2-15)$$

where  $\nu_0$  is the tune of  $m\nu_{x0}=p$  and  $\varepsilon$  is the change of tune per revolution.

Substitute Eq.( 2-15 ) to Eq.( 2-13 ) and take integral,

$$\psi \approx \int \nu(\theta) d\theta = \nu_0 \theta + \frac{\varepsilon\theta^2}{4\pi} . \quad (2-16)$$

On the other hand, Eq.( 2-14 ) becomes

$$\begin{aligned} J' &= \frac{mG_{m,0,p}}{2^m} \left( \frac{2J}{\nu_{x0}} \right)^{m/2} \sin(m\psi - p\theta - \eta) + \text{fast varying terms} \\ &= \frac{mG_{m,0,p}}{2^m} \left( \frac{2J}{\nu_{x0}} \right)^{m/2} \sin\left(\frac{m\varepsilon\theta^2}{4\pi} - \eta\right) + \text{fast varying terms} , \end{aligned} \quad (2-17)$$

since

$$m\psi - p\theta = m \left( v_{x0}\theta + \frac{\varepsilon\theta^2}{4\pi} \right) - p\theta = \frac{m\varepsilon\theta^2}{4\pi}. \quad (2-18)$$

Separate variables of Eq.( 2-17 ),

$$\frac{A'}{A^{m-1}} = \frac{mG_{m,0,p}}{2^m v_{x0}} \sin\left(\frac{m\varepsilon\theta^2}{4\pi} - \eta\right) + \text{fast varying terms}, \quad (2-19)$$

where  $A$  is defined by

$$A \equiv \sqrt{2J/v_{x0}}. \quad (2-20)$$

Taking integral of Eq.( 2-19 ), we get the change of  $A^{2-m}$ ,

$$\Delta(A^{2-m}) = (2-m) \frac{mG_{m,0,p}}{2^m v_{x0}} \int \sin\left(\frac{m\varepsilon\theta^2}{4\pi} - \eta\right) d\theta \quad \text{for } (m \neq 2), \quad (2-21)$$

$$\Delta(\log A) = \frac{mG_{m,0,p}}{2^m v_{x0}} \int \sin\left(\frac{m\varepsilon\theta^2}{4\pi} - \eta\right) d\theta \quad \text{for } (m = 2). \quad (2-22)$$

An integral appearing on the right hand side of Eq.( 2-21 ) and ( 2-22 ) contains Fresnel integral. When tune is far away from resonance before and after crossing, the invariant  $\theta$  is regarded as changing from  $-\infty$  to  $\infty$ . Then, the largest amplitude gain occurs for phase  $\eta = -\pi/4$ ,

$$\Delta(A^{2-m}) = (2-m) \frac{\pi G_{m,0,p}}{2^{m-1} v_{x0}} \sqrt{\frac{m}{\varepsilon}} \quad \text{for } (m \neq 2), \quad (2-23)$$

$$\Delta(\log A) = \frac{\pi G_{m,0,p}}{2^{m-1} v_{x0}} \sqrt{\frac{m}{\varepsilon}} \quad \text{for } (m = 2). \quad (2-24)$$

We see from Eq.( 2-23 ) and ( 2-24 ) that the maximum growth is proportional to driving-term divided by sqrt(crossing-speed). This scaling is common to any resonance.

## 2.4 Crossing with nonlinear detuning

### 2.4.1 “Particle trapping”

When nonlinear detuning is dominant, dynamics of crossing is quite different from one in the absence of nonlinear detuning. Chao and Month proposed a model of “Particle Trapping”. Their theory shows how “islands” in phase space trap particles and transport to larger amplitude, and they also developed an analytical expression of trapping efficiency. An “island” is a stable area in phase space isolated by separatrix and number of islands is as many as the order of resonance. They specifically treated fifth integer

resonance. For further discussion and comparison to experimental results we have obtained, analytical expressions for the uncoupled third order resonance have been derived following their treatment and a difference due to resonance order is to be discussed.

First we consider phase space topology of third integer resonance under the existence of nonlinear detuning due to octupole. Single particle motion of betatron oscillation can be written as

$$y(\theta) = [a(\theta)\beta(\theta)]^{1/2} \cos[\nu\theta + \varphi(\theta)], \quad (2-25)$$

where  $y$  is the displacement from closed orbit,  $\theta$  is the independent variable of azimuthal angle,  $\nu$  is the betatron tune and  $\beta$  is the beta-function.

Variables  $a$  and  $\varphi$  are canonical variables satisfying Eq. ( 2-26 )

$$a' = -\frac{2}{\nu\beta} \frac{\partial H^{(1)}}{\partial \varphi}, \quad \varphi' = \frac{2}{\nu\beta} \frac{\partial H^{(1)}}{\partial a}, \quad (2-26)$$

where  $a'$  and  $\varphi'$  are the derivatives respect to  $\theta$ ,  $H^{(1)}$  is the perturbation term of Hamiltonian. Obviously,  $a$  and  $\varphi$  are constants of motion in the absence of perturbation term.

For third integer resonance, the perturbation term  $H^{(1)}$  is

$$H^{(1)} = O(\theta)y^4 + S(\theta)y^3, \quad (2-27)$$

where  $S(\theta)$  and  $O(\theta)$  are proportional to the strength of octupole and sextupole respectively.

By using Eq.( 2-25 ) for  $y$  in Eq.( 2-27 ), we find the phase-independent term and the term slowing varying in time:

$$H^{(1)} = \nu\beta \left( 3B_0a^2 + |A_p|a^{3/2} \cos 3\psi \right), \quad (2-28)$$

where

$$B_0 = \frac{\langle \beta \rangle}{16\pi\nu} \int_0^{2\pi} d\theta O(\theta), \quad (2-29)$$

$$|A_p| = \frac{\langle \beta \rangle^{1/2}}{8\pi\nu} \int_0^{2\pi} d\theta e^{-ip\theta} S(\theta), \quad (2-30)$$

$$\psi = \left( \frac{1}{3}p - \nu \right) \theta - \varphi + \frac{1}{3}\eta, \quad (2-31)$$

and  $\eta$  is the phase factor,  $\langle \beta \rangle$  is the average value of beta-function; for simplicity, “smooth approximation” in which beta-function is assumed constant is employed here and the tune is close to the third integer resonance excited by p-th harmonic sextupole component.

With Eq.( 2-26 ) and Eq.( 2-28 ),

$$a' = -6|A_p|a^{3/2} \sin 3\psi , \quad (2-32)$$

$$\varphi' = 12B_0a + 3|A_p|a^{1/2} \cos 3\psi . \quad (2-33)$$

For further convenience, we define

$a_0$ : the average emittance of the initial particle distribution,

$\alpha = a/a_0$ : the relative emittance,

$\Delta_L = \frac{1}{3}p - v$ : the linear tune shift,

$\Delta_{NL} = -12B_0a_0$ : the nonlinear tune shift at emittance  $a_0$ ,

$\Delta_e = -3|A_p|a_0^{\frac{1}{2}}$ : the excitation width at emittance  $a_0$ ,

$B_0$ : the nonlinear detuning source (simply the nonlinear detuning),

$|A_p|$ : the resonance driving term (simply the driving term)<sup>2</sup>,

$$\xi = 3\Delta_L/2\Delta_e ,$$

$$\kappa = 3\Delta_{NL}/4\Delta_e .$$

With these symbols, the above equations for  $a$  and  $\varphi$  then become

$$(\alpha^{1/2})' = \Delta_e \alpha \sin 3\psi , \quad (2-34)$$

$$\psi' = \Delta_L + \Delta_{NL}\alpha + \alpha^{1/2}\Delta_e \cos 3\psi . \quad (2-35)$$

An invariant of the motion is

$$C = \xi\alpha + \kappa\alpha^2 + \alpha^{3/2} \cos 3\psi . \quad (2-36)$$

The invariant should be constant in each phase space trajectory. The fixed points can be obtained by solving following equations,

$$\left. \frac{\partial C}{\partial \alpha} \right|_f = 0 , \left. \frac{\partial C}{\partial \psi} \right|_f = 0 , \quad (2-37)$$

and whether these points are stable or unstable is determined as follows;

$$\begin{aligned} \left. \frac{\partial C^2}{\partial^2 \alpha} \right|_f \cdot \left. \frac{\partial C^2}{\partial^2 \psi} \right|_f &> 0 : \text{stable} , \\ \left. \frac{\partial C^2}{\partial^2 \alpha} \right|_f \cdot \left. \frac{\partial C^2}{\partial^2 \psi} \right|_f &< 0 : \text{unstable} . \end{aligned} \quad (2-38)$$

The fixed points are summarized in Table 2-1 and Fig. 2-1 shows a phase space topology for various parameter  $\xi$ .

---

<sup>2</sup> The definition of the driving term differs slightly from the one in Sec.2.1.2.

Table 2-1. Fixed points for third integer resonance ( $\kappa > 0$ ).

	Stable	Unstable	Origin
$\xi > \frac{9}{32\kappa}$	—	—	stable
$\xi = \frac{9}{32\kappa}$	$\alpha_s^{\frac{1}{2}} = \frac{3}{8\kappa}$	—	stable
$\frac{9}{32\kappa} > \xi > 0$	$\alpha_s^{\frac{1}{2}} = \frac{3}{8\kappa} \left( 1 + \sqrt{1 - \frac{32\kappa}{9}\xi} \right)$	$\alpha_u^{\frac{1}{2}} = \frac{3}{8\kappa} \left( 1 - \sqrt{1 - \frac{32\kappa}{9}\xi} \right)$	stable
$\xi = 0$	$\alpha_s^{\frac{1}{2}} = \frac{3}{4\kappa}$	—	unstable
$\xi < 0$	$\alpha_s^{\frac{1}{2}} = \frac{3}{8\kappa} \left( 1 + \sqrt{1 - \frac{32\kappa}{9}\xi} \right)$	$\alpha_u^{\frac{1}{2}} = \frac{3}{8\kappa} \left( -1 + \sqrt{1 - \frac{32\kappa}{9}\xi} \right)$	stable

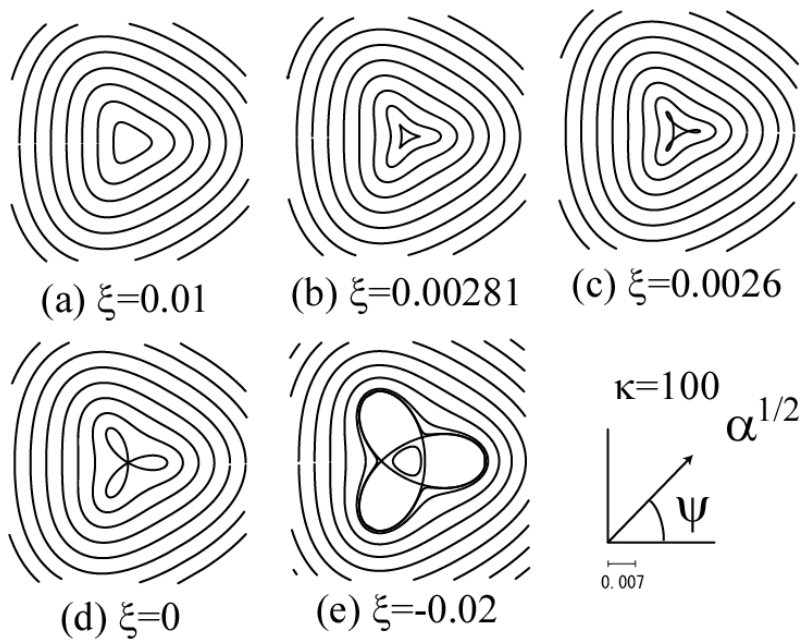


Figure 2-1. Phase space topology for third integer resonance.

During crossing third integer resonance, the phase space topology changes as shown in Fig. 2-1. It is seen that three islands are created and become larger as  $\xi$  decreases.

As shown in the last line of Table 2-1, stable and unstable fixed points are almost at the same amplitude when  $\kappa \gg 1$  and  $\xi$  is not close to zero. Since the islands are too small to trap particle when  $\xi$  is nearly zero, particles are mostly trapped at the amplitude for which the above approximation is valid.

Then,  $\alpha_s^{1/2}$  and  $\alpha_u^{1/2}$  are approximately

$$\alpha_s^{1/2} \approx \alpha_u^{1/2} \approx \left| \frac{\xi}{2\kappa} \right|^{\frac{1}{2}}. \quad (2-39)$$

The equation for separatrix, which is the border of islands, is

$$C = \xi\alpha_u + \kappa\alpha_u^2 + \alpha_u^{3/2} = \xi\alpha + \kappa\alpha^2 + \alpha^{3/2} \cos 3\psi. \quad (2-40)$$

Set  $\cos 3\psi = 1$  and  $\alpha = \alpha_u + \delta$ , and solve for  $\delta$ . Then the difference between two solutions  $\delta_+ - \delta_-$  is the width of the island along the radial direction multiplied by  $2\alpha_u^{1/2}$ ,

$$\delta_+ - \delta_- \approx 2\alpha_u^{1/2} (\alpha_+^{1/2} - \alpha_-^{1/2}). \quad (2-41)$$

The island width of phase direction is simply  $\frac{1}{3}\pi\alpha_u^{1/2}$ . Hence the total area of three islands is approximately

$$A \approx \frac{\pi^2}{\sqrt{2}} \kappa^{-\frac{1}{2}} \alpha_s^{\frac{3}{4}}. \quad (2-42)$$

When  $\xi$  changes dynamically, the stable fixed points of island center is moving outward at the rate

$$\left( \alpha_s^{1/2} \right)' = \frac{\xi'}{3/2 - 4\kappa\alpha_s^{1/2}}. \quad (2-43)$$

From Eqs.( 2-34 ) and ( 2-43 ), a criterion for adiabaticity is

$$\Delta_e \alpha > \frac{\xi'}{3/2 - 4\kappa\alpha^{1/2}}. \quad (2-44)$$

If we replace the inequality by the equality in Eq.( 2-44 ), we can define adiabatic parameter, which describes how crossing speed is fast compared to fully adiabatic condition;

$$\alpha_1 = \left( \frac{\varepsilon}{4\pi\Delta_{NL}\Delta_e} \right)^{\frac{2}{3}}, \quad (2-45)$$

where  $\varepsilon$  is the change of  $\Delta_L$  per revolution and  $\kappa \gg 1$  is assumed again.

To follow island center, in other words to be trapped, a particle must have sufficiently rapid amplitude change, i.e.

$$\alpha \geq \alpha_1. \quad (2-46)$$

If a Gaussian amplitude distribution is assumed for the trapping efficiency, the particle density is given by

$$D(\alpha^{1/2})d\alpha^{1/2} = 2\alpha^{1/2}d\alpha^{1/2}e^{-\alpha}, \quad (2-47)$$

$$\int_0^\infty D(\alpha^{1/2})d\alpha^{1/2} = 1, \quad (2-48)$$

where the second equation is the normalization in which total density is unity.

With Eqs. ( 2-46 ) and ( 2-48 ), trapping efficiency is

$$P_T = \frac{A}{\pi(\alpha_s^{1/2})^2} \exp(-\alpha_1). \quad (2-49)$$

where  $\alpha_s$  is “typical trapping amplitude”,

$$\alpha_s^{1/2} \approx \begin{cases} \alpha_1^{1/2}, & \text{if } \alpha_1 > 1, \\ 1, & \text{if } \alpha_1 < 1 \end{cases}. \quad (2-50)$$

The reason for Eq.( 2-50 ) is as follows. When  $\alpha_1 > 1$ , a typical particle being trapped will be around the lower limit of  $\alpha_1^{1/2}$ . When  $\alpha_1 < 1$ , the denser distribution satisfying  $\alpha > \alpha_1$  is around  $\alpha = 1$ .

In Eq.( 2-49 ), the factor  $\frac{A}{\pi(\alpha_s^{1/2})^2}$  represents a normalization by total island area divided by beam radius of “typical trapping amplitude”.

For third integer resonance crossing, Eq. ( 2-49 ) can be expressed as

$$P_T = \frac{\pi}{\sqrt{2}} \kappa^{-1/2} \alpha_s^{-1/4} \exp(-\alpha_1). \quad (2-51)$$

We now examine a difference between third and fifth integer resonances.

Figure 2-2 shows phase space topology for fifth integer resonance.

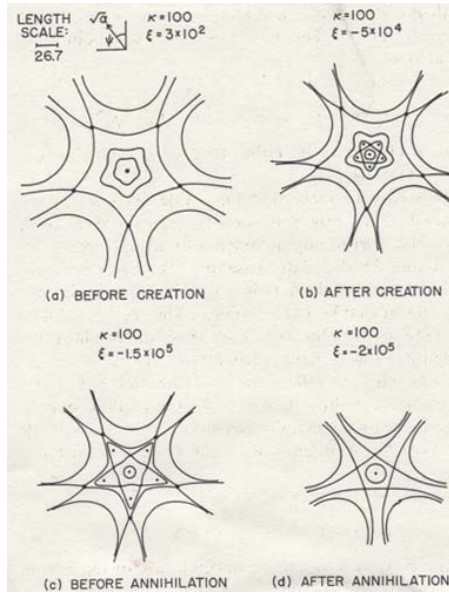


Figure 2-2. Phase space topology of fifth integer resonance (taken from Ref.[ 18 ]).

An important point is whether phase space trajectory is “open” or “closed”. It is always “closed” in third integer resonance, in fact trajectories outer islands make loops but they are “open” in fifth integer resonance. As is said in Ref.[ 18 ], in fifth integer resonance, if beam emittance is larger than outer unstable fixed points, an explosion of particle distribution immediately occurs. This is because nonlinear detuning is relatively weak. Contrary to that, there would not be an explosion in third integer resonance.

#### 2.4.2 Reverse crossing

Particle trapping due to resonance crossing in one direction is discussed so far. However, a completely different picture emerges when a resonance is crossed in the reverse direction. When amplitude dependence of tune is positive and tune decreases as the resonance is crossed, islands move outward and “particle trapping” occurs. When amplitude dependence of tune is negative and tune increases as the resonance is crossed, it also results in “particle trapping”. However, if amplitude dependence of tune or direction of tune change is reversed, islands move inward. As shown in Fig. 2-1, in the order from (e) to (a), islands that are initially far away approach close to the beam and finally disappear after crossing resonance. In this subsection, reverse crossing is discussed.

We assume that the crossing can be regarded as an adiabatic process so that a quasi-static description in phase space is valid. A potentially complex issue of the dependence on crossing speed is then avoided in the following discussion. Even if crossing speed is infinitely slow, one can predict that there is no particle to be taken away infinite amplitude because trajectory outside islands chain is closed.

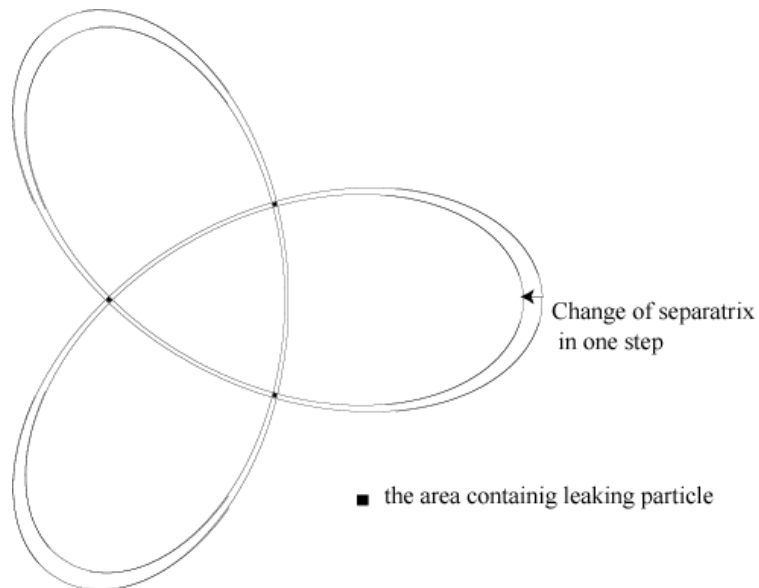
Consider the behavior of particles in a beam going through a reverse crossing of an uncoupled third integer resonance assuming that the beam initially occupy an elliptic area in phase space as defined by the linear lattice parameters. The central stable area is much larger than the beam emittance. As the tune comes close to resonance, the beam is deformed from an ellipse to a triangular shape as shown in Fig. 2-1(e). The deformation continues until the central area is completely filled by the beam. Since the process is adiabatic, the deformed area occupied by the beam is the same as the initial beam emittance. As the central stable area continues to shrink, some particles must exit from this area since the particle density cannot be increased in the absence of some external cooling mechanism.

Figure 2-3 shows the separatrices of central area and three outer islands in phase space as they continue to move inward. Particles near three unstable fixed points, dark spots at the apexes of triangular shape, hardly move so that they leak out of the shrinking central area. Once out, they stream along a trajectory just outside of three islands that exist at that moment. This closed trajectory surrounds all three islands.

Particles near the border of the central area, the black bands in Fig. 2-4, also move out of the area and they may enter the neighboring island. Since outer islands and the central area continue to shrink and eventually disappear altogether, as shown in Fig. 2-1(b) and (c), all particles of the beam will be within an enclosed area in phase space.

Based on this qualitative description, we can surmise that this area is equal to the combined area of three islands and the central area that existed at the moment when the central area was completely filled with particles and the leaking process commenced. It is also clear that the net effect of reverse crossing is simply a growth in the beam emittance and, in general, not a beam loss. One would have a question why beam emittance grows due to adiabatic crossing. Although local density of particles must not change after crossing because of Liouville's theorem, the amplitude of particles that get out the central area becomes large. Since particle near the fixed points move very slowly, adiabatic condition is violated even if crossing is infinitely slow. Therefore, beam emittance grows due to reverse crossing.

Based on this model, we can find an analytic form of the final emittance as follows.



**Figure 2-3. Schematic figure of leaking.**

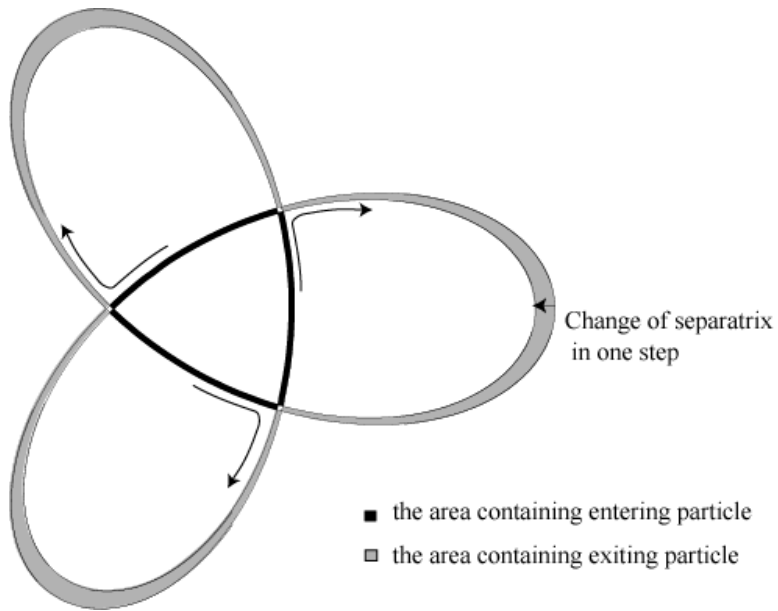


**Figure 2-4. Schematic figure of entering and exiting island.**

First, we take the initial beam emittance to be  $R\alpha_0$ , where  $\alpha_0$  is the average emittance,  $R$  is the constant of  $R>1$  and all particles are assumed to be within  $R\alpha_0$ . Then the relative emittance becomes  $\alpha=R$ . When the islands contact the beam, the particle distribution is deformed. If driving term is relatively large, deformed beam becomes almost triangle and when driving term is relatively small, it is just slightly deformed and keeps the elliptic shape. However, the area occupied by initial beam is constant if crossing is assumed to be adiabatic.

Total area of island is given by (see Eq.( 2-42 ))

$$A \approx \frac{\pi^2}{\sqrt{2}} \kappa^{-1/2} \alpha_s^{3/4}. \quad (2-52)$$

Since we exclude a large growth in the beam emittance, we are assuming a relatively small driving term that causes a growth of not much more than, say, 30%. Then,  $\alpha_s$  in Eq.( 2-52 ) can be replaced by  $R$ . Finally, the relative emittance growth of adiabatic crossing can be represented as

$$\frac{R + A/\pi}{R} = 1 + \frac{\pi}{\sqrt{2}} \kappa^{-1/2} R^{-1/4}. \quad (2-53)$$

The only discussion we find in the past studies regarding reverse crossing is by Sturrock (p144 line11-14 of Ref.[ 15 ]). He says that ‘If the radius of beam is initially less than  $K_0$ , the amplitude of the “elbow”, the final radius will exceed  $K_0$ ; however, if the radius is initially larger than  $K_0$ , the final radius may be not very different from the

initial radius.' where  $K_0$  is the annihilating point of islands. The statement is correct qualitatively. In fact, very large  $\kappa$  in Eq.( 2-53 ) means small  $K_0$  (see Table 2-1) and leads negligible growth. However, unlike our finding of the quantitative estimate, Eq.( 2-53 ), the emittance growth was not discussed in a quantitative manner.

## **Chapter 3**

# **Beam Studies**

In order to study dynamics of resonance crossing, beam studies were performed using PoP FFAG accelerator and HIMAC synchrotron. The reasons for the use of these accelerators are as follows.

- PoP: At present it is the only proton FFAG accelerator in the world.  
Its compact size is especially convenient for many types of beam studies.  
Through commissioning and subsequent machine studies, we have come to understand its properties.
- HIMAC: It is possible to examine both directions of crossing in the machine (not possible with PoP). Furthermore, this has a gas sheet monitor that can be used for a direct observation of beam profiles.

In Sec.3.1 and Sec.3.2, beam studies with PoP and HIAMC are described, respectively.

### **3.1 Resonance Crossing Experiment at PoP FFAG**

Beam studies of resonance crossing were performed with PoP. Various crossing speeds and driving terms were examined. In this section, details and results of experiments are described.

#### **3.1.1 PoP**

Figure 3-1 is a picture of PoP and the machine parameters are summarized in Table 3-1.

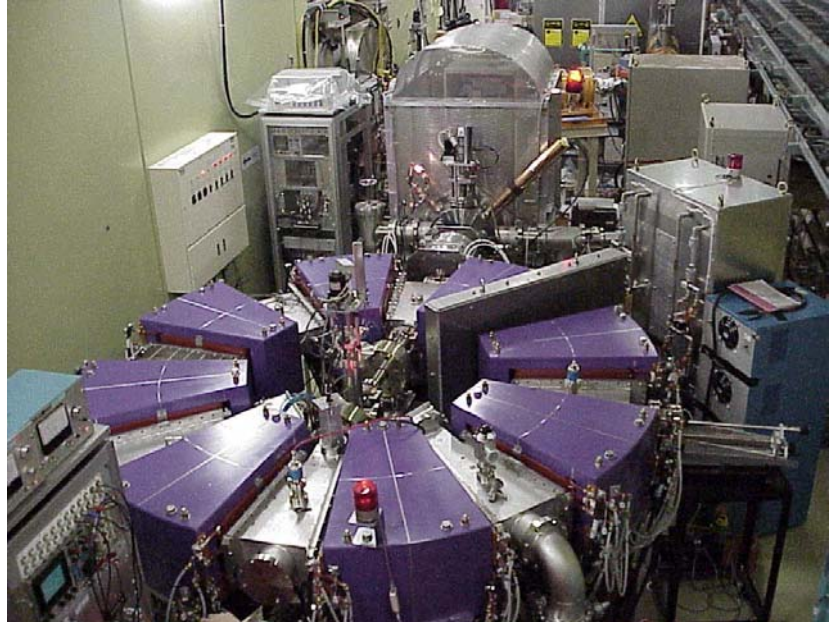


**Figure 3-1. PoP.**

**Table 3-1. Parameters of PoP.**

Number of sector	8
k value	2.5
Kinetic energy	50keV~500keV
Magnetic field	0.14T~0.32T (F magnet) 0.04T~0.13T (D magnet)
Average radius	0.81m~1.14m
Betatron tune	2.22~2.16 (Horizontal) 1.26~1.23 (Vertical)
Repetition	1kHz
Frequency / RF voltage	0.61MHz~1.40MHz / 4kVpp

PoP-FFAG is the world's first proton FFAG accelerator constructed at KEK in 2000. Commissioning of PoP was successfully achieved [ 22 ]. After commissioning, the machine has been used for beam studies [ 23 ][ 24 ][ 25 ], education and training of accelerator operation.

PoP was designed as a radial sector type scaling FFAG whose magnetic field on the median plane in focusing and defocusing magnet are, respectively,

$$B_F = B_{F0} \left( \frac{r}{r_0} \right)^k , \quad (3-1)$$

$$B_D = B_{D0} \left( \frac{r}{r_0} \right)^k , \quad (3-2)$$

where  $r$  is the machine radius,  $r_0$  is the reference radius,  $B_{F0}$  and  $B_{D0}$  are the field strengths at the reference radius and  $k$  is the field index or the so-called k-value. In order to realize strong focusing, the direction of field in focusing and defocusing magnet are opposite,

$$B_{F0}B_{D0} < 0 . \quad (3-3)$$

In PoP, focusing magnets are normal bending and defocusing magnets are reverse bending.

Figure 3-2 shows a top plan of PoP. Proton beam from the ion source goes to the injection septum through the injection line. A beam chopper is installed at the injection line. The electrostatic septum and electro-pulsed bumps inject beam into the ring. Multi-turn injection mode allows injecting beam during about 10 revolutions. Lattice of the ring is D-F-D triplet [ 26 ]. One focusing magnet and two defocusing magnets are combined to be one magnet, but coil current of focusing and defocusing magnet are supplied independently to control a ratio of focusing and defocusing strengths. The rf cavity is a broadband cavity using MA core [ 7 ]. Even though the revolution frequency changes in a wide range from injection to final, it is not necessary to tune the resonant frequency of cavity. Arbitrary waveform generator makes low-level signal of rf voltage. With very high rf voltage compared with the beam energy, one special feature of the machine is a fast acceleration with period less than 1ms. It is possible to take a wide range of acceleration rate in beam studies. A beam position monitor (BPM) and a scraper are installed to measure the beam position and profile. (The scraper is moved to the straight section of injection septum temporarily for this experiment.) Fig. 3-3 shows a picture of BPM in the vacuum chamber and the geometry of electrodes schematically.

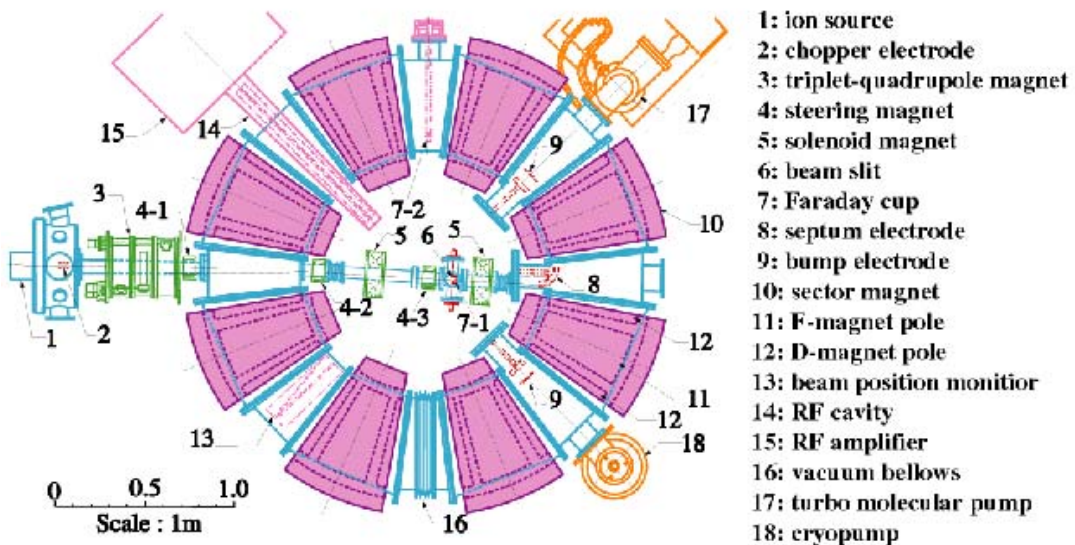


Figure 3-2. Top plan of PoP.

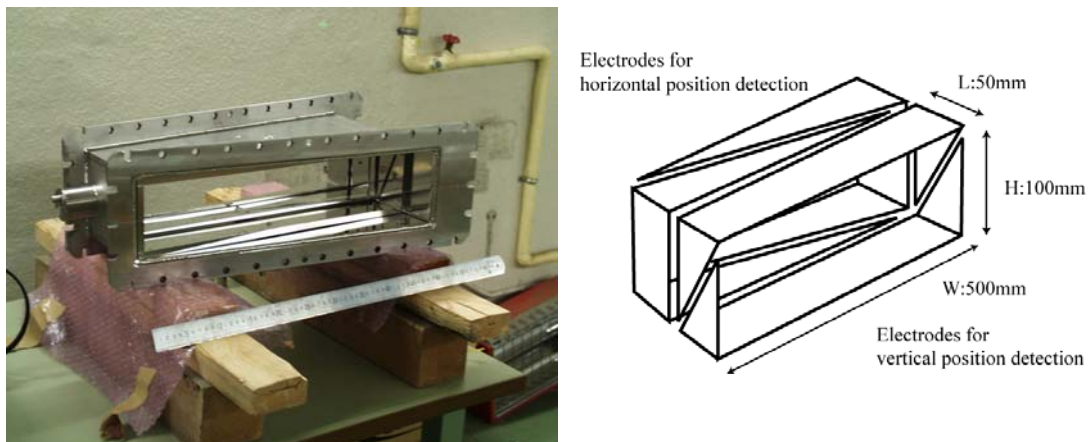


Figure 3-3 Beam Position Monitor (BPM).

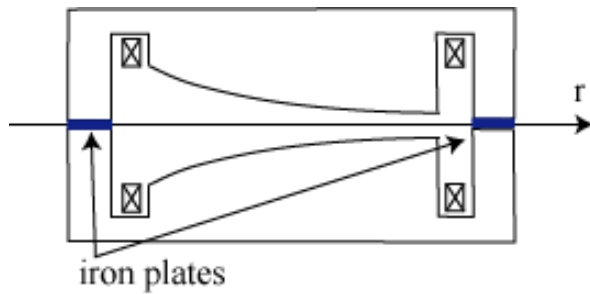
### 3.1.2 Remodeling of magnet

PoP is designed as a scaling FFAG with almost constant tunes from the injection energy to the final energy as shown in Table 3-1. Therefore, it is necessary for crossing

experiment to introduce time-varying (energy-varying) tune. Magnets of PoP were remodeled for this purpose. The method used here is to insert iron plates between upper and lower parts of magnet as shown in Fig. 3-4. With the iron plates of 4mm thickness, the gap of magnet is widened. Since the gap is decreasing as the radius increases, relative change of gap becomes larger in outer radius and magnetic field also has a larger relative change in outer radius. This creates k-value changes along the radius and mainly a variation of horizontal tune is introduced. Iron plates were installed in all eight magnets so that super-periodicity remains the same.



(a) Picture of installed iron plate



(b) Cross section of magnet with iron plate

Figure 3-4. Remodeling of magnet.

### 3.1.3 Betatron tune measurement

After remodeling of magnet, energy dependence of betatron tune was measured. Once energy dependence, a slope of tune to beam energy, is known, crossing speed is determined as the product of slope and energy gain per turn. Sidebands of betatron oscillation were measured with Fast Fourier Transform (FFT) of BPM signal. However, after many revolutions, a coherent dipole oscillation decays because of nonlinear detuning. Therefore, after acceleration, rf knock out (RFKO) method was used to excite dipole oscillation. In horizontal direction, the accelerating rf cavity is substituted. Since dispersion function is not zero at the center of straight section where rf cavity is located,

acceleration and deceleration correspond to horizontal displacements. For vertical tune measurements, exclusive RFKO electrode to excite vertical oscillation was used.

Fig. 3-5 shows measured and calculated betatron tunes. FD ratio of 2.43 is selected to cross third integer resonance  $3\nu_x=7$ . Here FD ratio is simply a ratio of focusing field to defocusing field. The detail of tune calculation using RK tracking is in Appendix B. The resonance of  $3\nu_x=7$  is excited by the 7th harmonics of normal sextupole component.

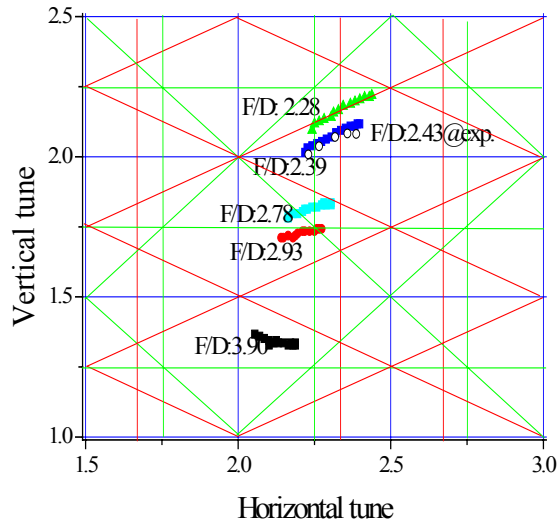


**Figure 3-5. Betatron tune after remodeling.**

Calculation results are shown for various FD ratios. Open circles show measurement results. FD ratio of 3.9 is nominal operation condition (without iron plates).

Figure 3-6 shows the energy dependencies of betatron tune on beam energy.

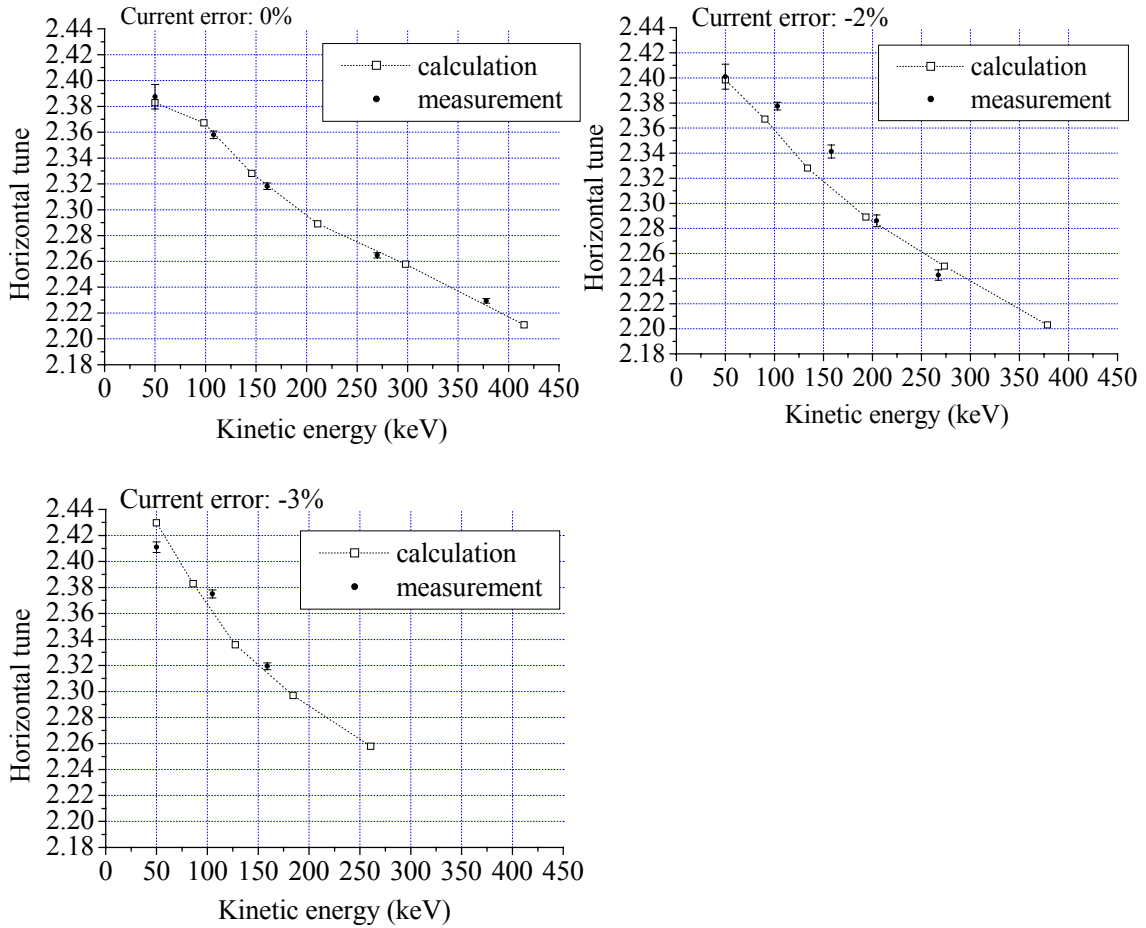


**Figure 3-6. Measured and calculated betatron tune.**

“Current error” is the parameter for driving term described in Sect 3.1.5. The error bars of measurement data are due to the resolution of FFT analysis.

As shown in Fig. 3-6, horizontal tune crosses the resonance of  $3v_x=7$  around 130 keV. The machine radius corresponding to this energy is about 0.89m.

### 3.1.4 Longitudinal beam handling

Crossing speed is one of the important parameters in dynamics of resonance crossing. However, it is impossible to give the same speed to all particles in a bunched beam because of synchrotron oscillation. For an unambiguous observation, the fluctuation of crossing speed was controlled to be as small as possible. The longitudinal beam handling is a key factor of the experiment. Two efforts were made to suppress the fluctuation of crossing speed. One is to make bunch length as short as possible, and the other is to inject beam to the center of rf bucket. Beam chopper was tuned to chop out a short bunch of less than 100ns. This length corresponds to rf phase of 20 degrees, which is equivalent to a bunching factor of 0.06, at injection energy. In order to inject a beam into the center of rf bucket, a mountain view plot was used for tuning. Figure 3-7 shows an example of mountain view plot. During data acquisition, mountain view plot was always checked to confirm that the dipole oscillation is small enough.

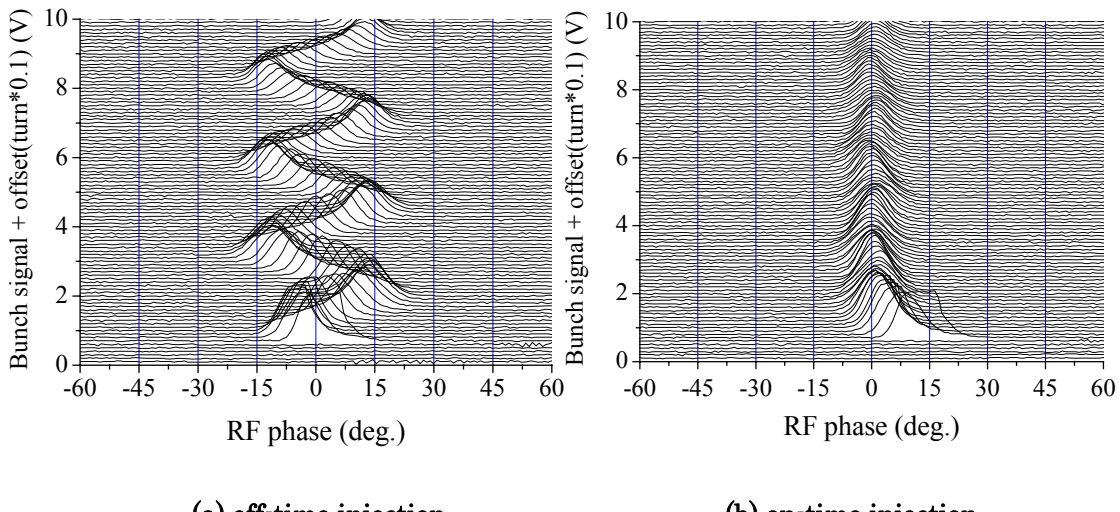


**Figure 3-7. Examples of mountain view plot.**

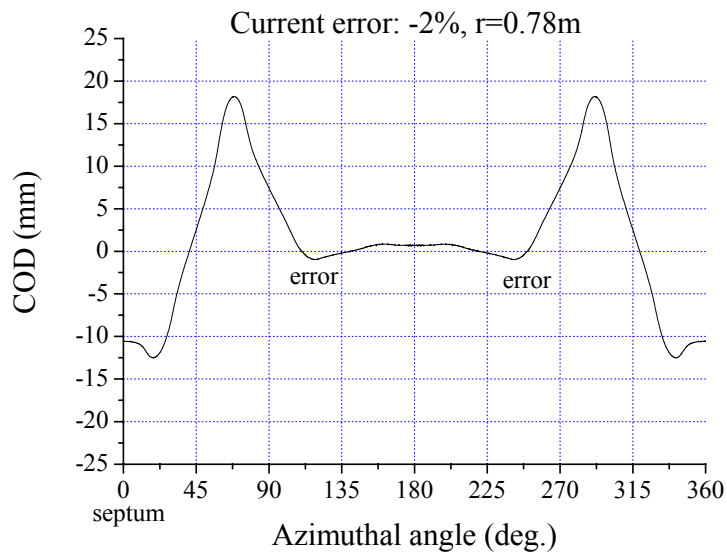
Mountain view plot is drawn ordering turn-by-turn bunch signal as a function of rf phase. It visualizes synchrotron oscillation, since a bunch signal is the projection of longitudinal distribution of particles. These examples are from injection tuning; injection timing is out of synchronization in (a), and (b) is after tuning.

### 3.1.5 Driving term and nonlinear detuning

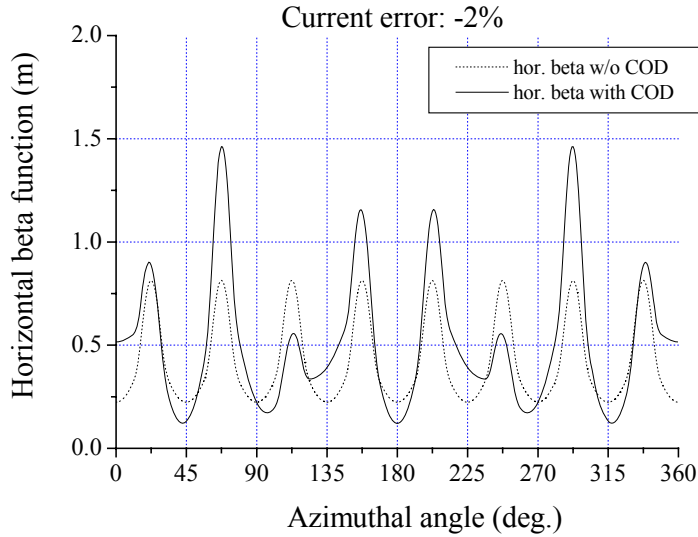
A driving term was introduced with closed orbit distortion (COD). COD induces driving term of resonance. There are two COD sources, a variable term actively introduced by changing of magnetic field and the other an offset term induced by rf cavity.

Two magnets separated by three cells were selected to be variable COD sources. Coil current of focusing magnet of these two magnets was set at a different value from the one for the other six magnets. Figure 3-8 shows a calculated COD and horizontal beta function along COD with a coil current error of -2% .

For a successful beam injection, the angle between COD and the injection septum is important. In Fig. 3-8(a), the angle of COD at the injection septum remains unchanged, which is the reason for using a pair of magnets, instead of one, to be the error sources. As a consequence, the angle of COD is kept but the position is changed. At the same time, strength of magnet excitation is reduced at the same ratio in all eight magnets to keep the position of COD unchanged. Another possible choice of location of the injection septum is at azimuthal angle of 180degrees in Fig. 3-8. It is a good location since the angle of COD is unchanged and COD is almost zero at the position. But this location is not used because of the small beta function there. With a small beta function, it might be difficult to control horizontal emittance because of a beta function mismatch.



(a) COD due to current error of two focus magnets



(b) Modulation of beta function due to COD

**Figure 3-8. Variable COD and modulation of beta function.**

Vertical grid lines correspond to the center of straight section.  
The injection septum is located at azimuthal angle of zero.

The magnetic core of rf cavity installed at the center of straight section is penetrated by the fringe field of defocusing magnet. This creates a dipole error, an additional source of COD. Magnitude of dipole error is estimated by a three-dimensional field calculation. Figure 3-9 shows the estimated magnitude of dipole error.

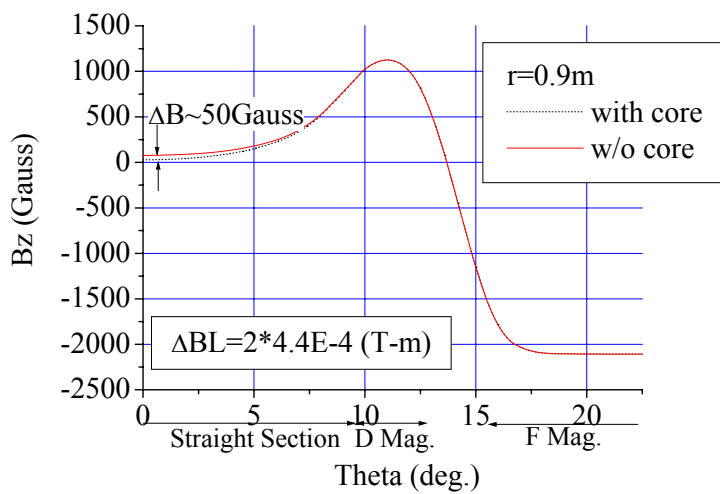


**Figure 3-9. Estimated dipole error caused by rf core.**

Due to the phase relation between the variable term and the offset term, the combined driving term is not proportional to the amount of magnet error. Driving terms for various current errors are shown in Fig. 3-10. For third integer resonance crossing, three values of current errors, 0%, -2% and -3% were examined.

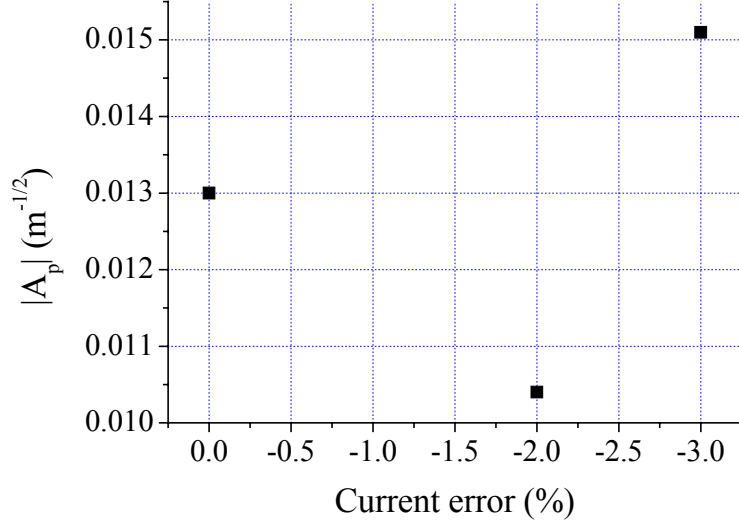


**Figure 3-10. Driving term with the combination of offset and variable term.**

Nonlinear detuning is introduced by intrinsic octupole. Eq.( 3-1 ) is expanded as

$$B_F = B_{F0} \left( \frac{r}{r_0} \right)^k = B_{F0} \left[ 1 + \frac{k}{r_0} x + \frac{k(k-1)}{2!r_0^2} x^2 + \frac{k(k-1)(k-2)}{3!r_0^3} x^3 \dots \right], \quad (3-4)$$

where  $x$  is

$$x \equiv r - r_0 . \quad (3-5)$$

As shown in Eq.( 3-4 ), magnetic field has octupole component in principle. Since nonlinear detuning is mainly determined by the octupole components in focusing magnets, amplitude dependent tune shift is positive. Nonlinear detuning for three current errors are shown in Fig. 3-11.

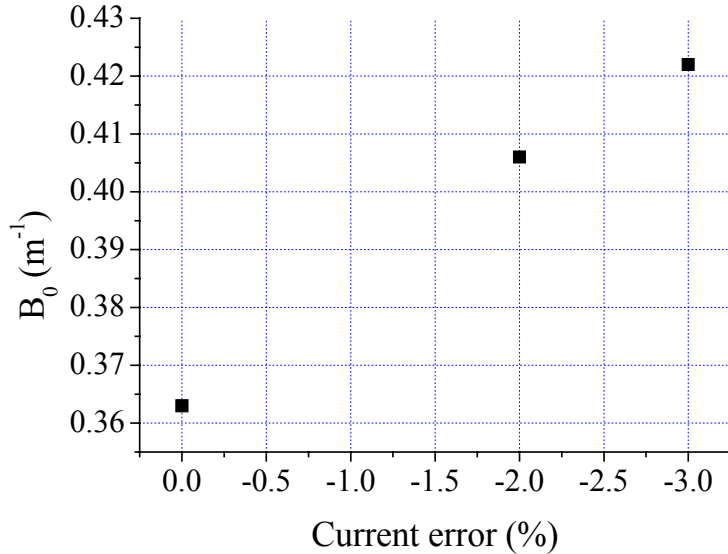


**Figure 3-11.** Nonlinear detuning for various current errors.

Since closed orbit is change with current error, nonlinear detuning is varied as shown in Fig. 3-11.

Driving term and nonlinear detuning are not purely determined by sextupole and octupole alone. In Fig. 3-10 and Fig. 3-11, the contributions of other components are included. Details of calculation of driving term and nonlinear detuning are described in Appendix C.

### 3.1.6 Beam injection

Tuning of beam injection determines transverse emittance, which is an important parameter for resonance crossing. In order to find a suitable strength of injection bumps, beam position is measured over many revolutions to observe amplitude of betatron oscillation for various bump strength. Figure 3-9 shows typical results of the measurement.

In Fig. 3-12, it is seen that amplitude of coherent dipole oscillation changes as the bump voltage is changed. When a bump voltage is not right, a coherent dipole oscillation is detected as shown in Fig. 3-12. A bump voltage was selected so that dipole oscillation is at the minimum.

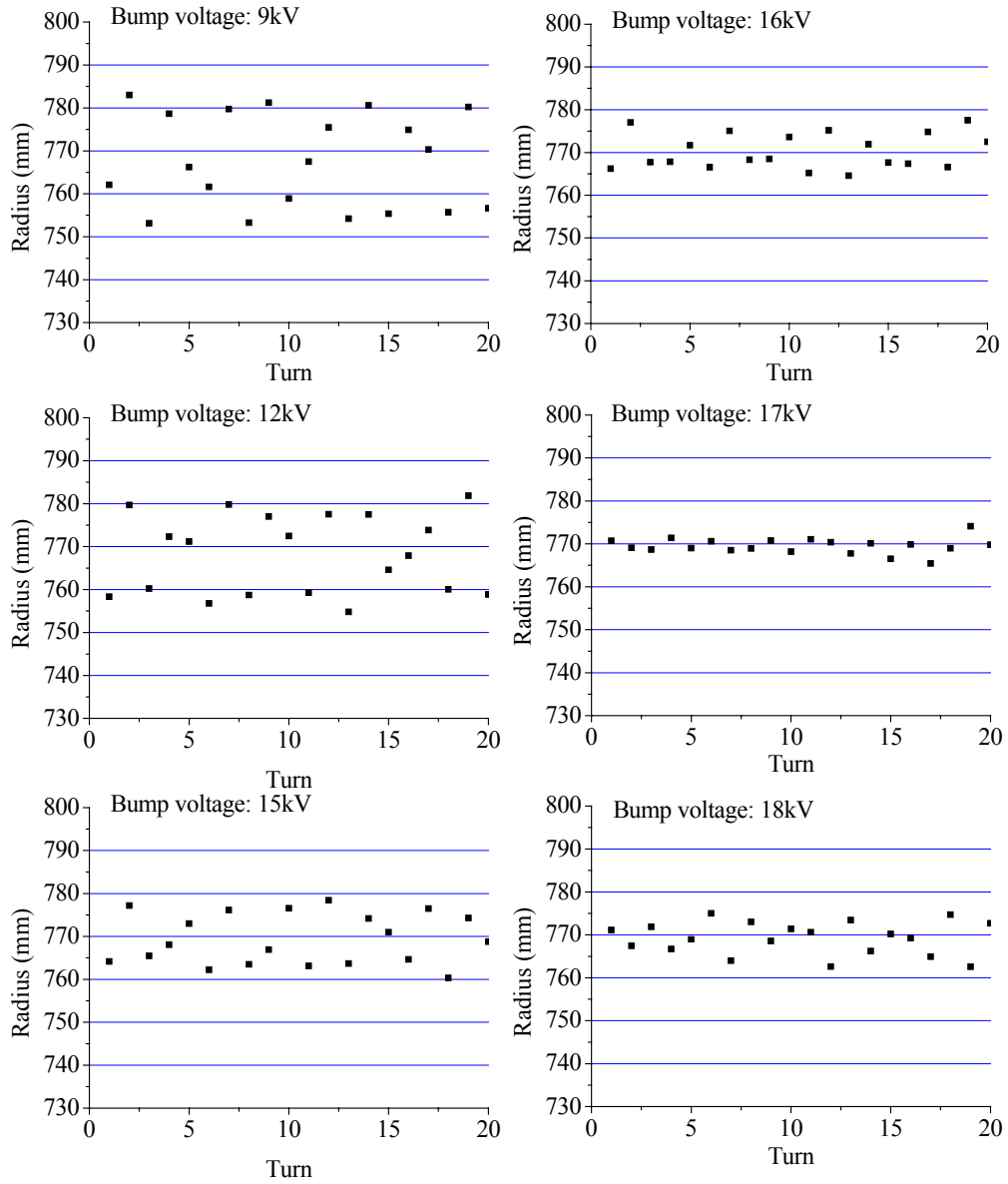
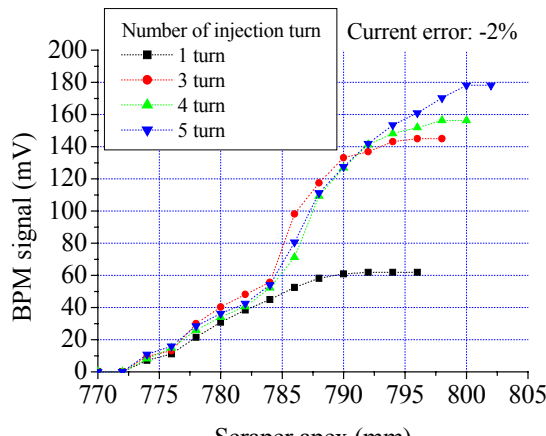


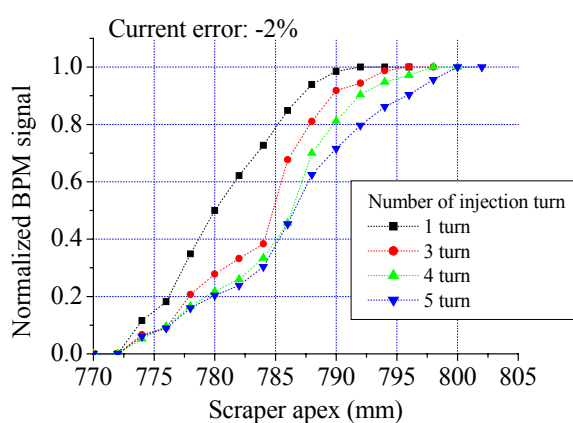
**Figure 3-12. Beam position measurement for injection tuning.**

It is seen that amplitude of betatron oscillation changes depending on the bump voltage. Bump voltage of 17kV is optimum in this measurement.

It is difficult to observe the effect of resonance crossing clearly when the beam emittance is too small. By varying the number of turns of multi-turn injection, horizontal emittance was increased to an appropriate value. Then the time separation between each chopped beam was chosen to be the revolution period. Injection beam size was measured using the scraper and BPM. When the apex of scraper is at the closed orbit, injected beam will be totally scraped off in several revolutions. The scraper position and signal level of BPM were recorded. Figure 3-13 shows typical result of injection beam size measurement.



(a) BPM signal versus scraper position



(b) Normalized BPM signal

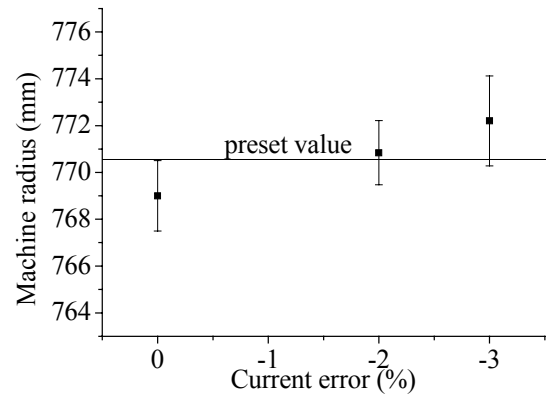
Figure 3-13. Injection beam size measurement using scraper.

It is seen that beam size becomes larger with multi-turn injection. Four-turn injection was selected, for  $-2\%$  current error, so that  $87\%$  emittance becomes about  $800\pi \text{ mm-mrad}$ .

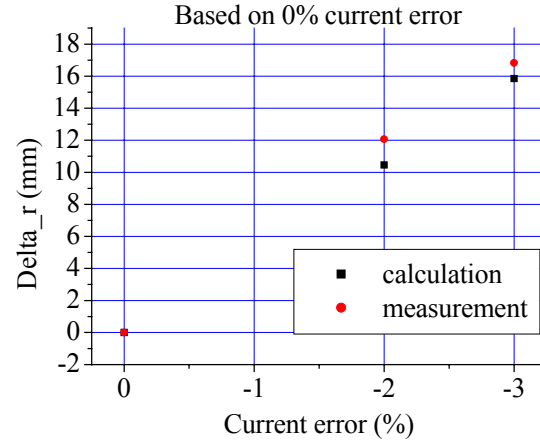
Once the beam size is measured, an emittance of the beam can be evaluated. Since it is difficult to measure beta function, the calculated value is used here. Horizontal 87% emittance was set to be about  $800\pi$  mm-mrad at injection for third integer crossing. As a consequence of adiabatic damping, horizontal emittance would shrink to about  $500\pi$  mm-mrad when the resonance is crossed around 130keV. Vertical full emittance is estimated to be approximately  $150\pi$  mm-mrad from the geometrical structure of ion source.

### 3.1.7 COD confirmation

After beam injection, the position of distorted closed orbit was measured at two azimuthal locations of scraper and BPM to verify that COD is formed as expected. Figure 3-14 shows measurement results.



(a) COD measurement using scraper



(b) COD measurement using BPM

Figure 3-14. COD measurement.

As shown in Fig. 3-14, measured CODs are in good agreement with preset values.

### 3.1.8 Measurement of beam before and after crossing

Figure 3-15 shows the basic idea of beam measurement. With a scraper inserted from outside of the ring, the particle distribution was measured before and after crossing. During acceleration, the beam orbit shifts toward outer radius and the beam is scraped gradually by the scraper preset at an observation position. A decreasing curve of the beam intensity contains information of the particle distribution. Note that it is not in real space but in the amplitude of betatron oscillation. Also a decreasing curve of beam intensity can be converted to beam size. This measurement provides the main data of resonance crossing.

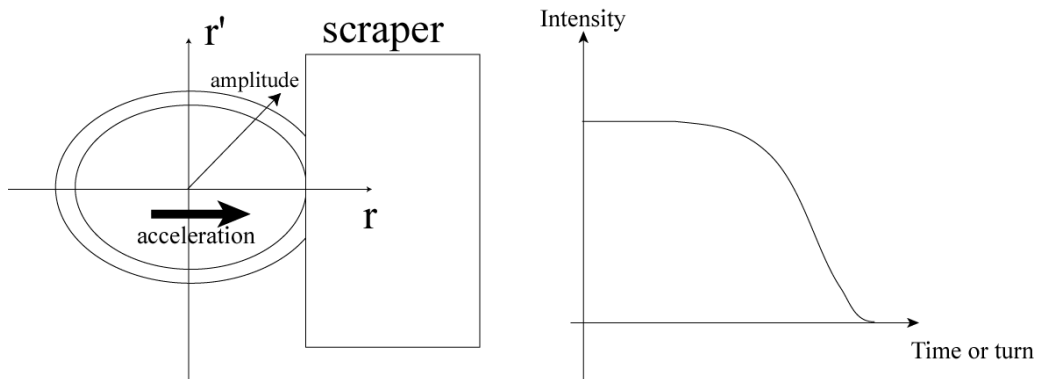


Figure 3-15. Concept of beam measurement of accelerating beam.

### 3.1.9 Data analysis

Data analysis was carried out with following procedures.

- I. Finding beam intensity during scraping from BPM signals
- II. Correcting beam loss due to residual gas
- III. Obtaining particle distribution in beam emittance

## I. Finding beam intensity during scraping from BPM signals

Since no intensity monitor is in PoP, BPM is used instead to find the beam intensity. To detect beam position, BPM has two pairs of electrodes, one for horizontal and the other for vertical positions. A pair of electrodes for horizontal position is used to measure the beam intensity. Beam orbit shifts to outer radius during acceleration, therefore a signal obtained with inner electrode decreases during acceleration while that of outer electrode increases. Even then the summation of outer and inner electrode signals is equivalent to bunch signal. A turn-by-turn integral of bunch signal becomes beam intensity of each turn. With this procedure, beam intensity curves are obtained from BPM signals. Figure 3-16 is an example of intensity curves obtained from BPM raw data.

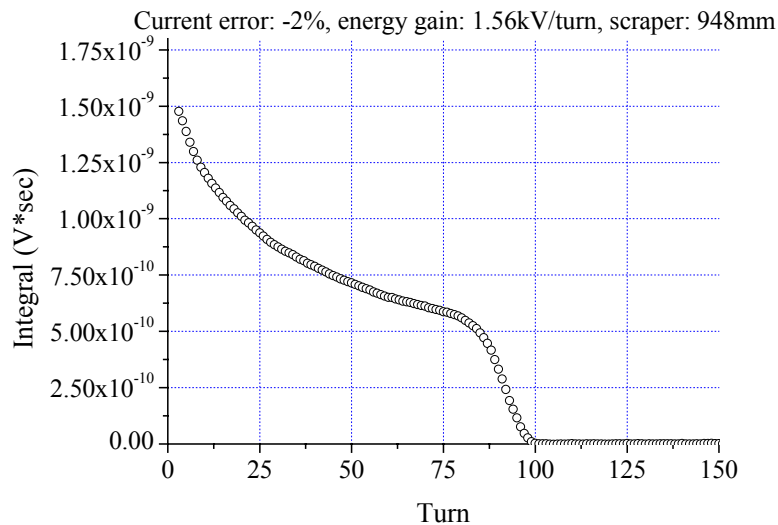


**Figure 3-16. Intensity curve obtained from BPM signal.**

## II. Correcting beam loss due to residual gas

Since the energy range of PoP is low, beam loss due to residual gas is not negligible, especially near injection energy. A correction of beam loss is necessary because beam loss continues during beam scraping. The dominant process of beam loss is a charge transfer in which a charged particle loses its charge and is lost through single process, therefore the beam emittance does not change in the process although the intensity decreases. Beam intensity curves are corrected considering a charge transfer. Detail of

the correction is described in Appendix D. After the correction, normalized intensity curve, which decrease from one to zero with scraping, is obtained. Figure 3-17 shows the corrected result of Fig. 3-16.

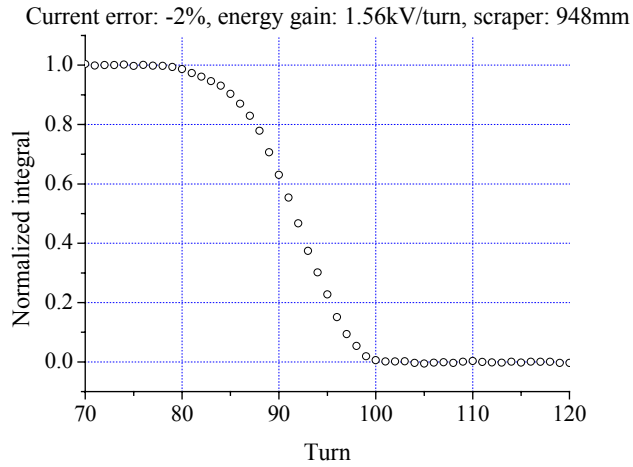


**Figure 3-17. Normalized intensity curve.**

### III. Obtaining particle distribution in beam emittance

In order to obtain the particle distribution in beam emittance, horizontal axis is transformed. First, number of turn is converted into the length of orbit shift during acceleration. The relation between beam energy and the machine radius is given by RK tracking and is confirmed experimentally using the scraper. Therefore, the length of orbit shift in each turn is known. Once horizontal axis becomes the length in real space, the particle distribution can be obtained by differentiating normalized intensity curve with respect to the beam emittance. Then beta function is also given by RK tracking. Figure 3-18 shows an example of the particle distribution obtained with normalized intensity curve of Fig. 3-17.

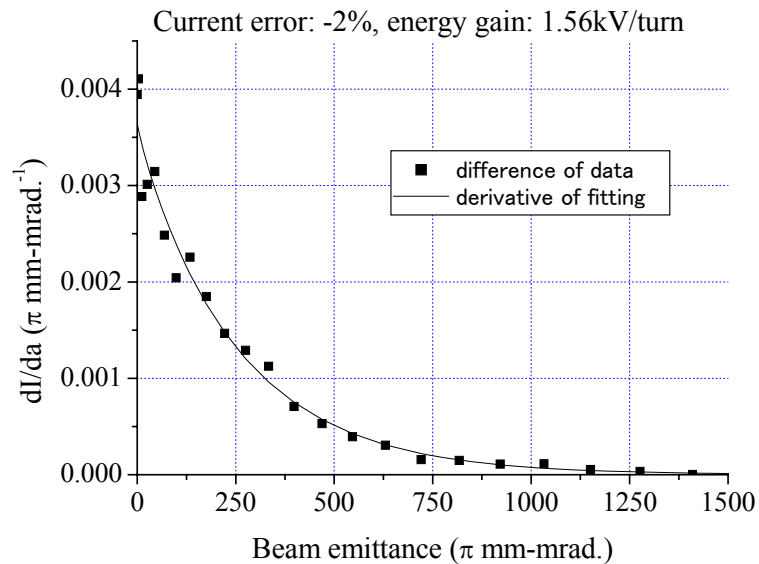


**Figure 3-18. Particle distribution in beam emittance.**

### 3.1.10 Beam emittance just before crossing

From the normalized intensity curve during beam scraping, the beam size immediately before crossing resonance is evaluated and this is used to estimate the beam emittance. Beta function necessary for this procedure is calculated using RK tracking. The beam size is determined by a fitting of intensity curve, and then a Gaussian distribution is assumed. Figure 3-19 shows results of fitting and Table 3-2 lists 87% beam emittance at injection and just before crossing resonance.

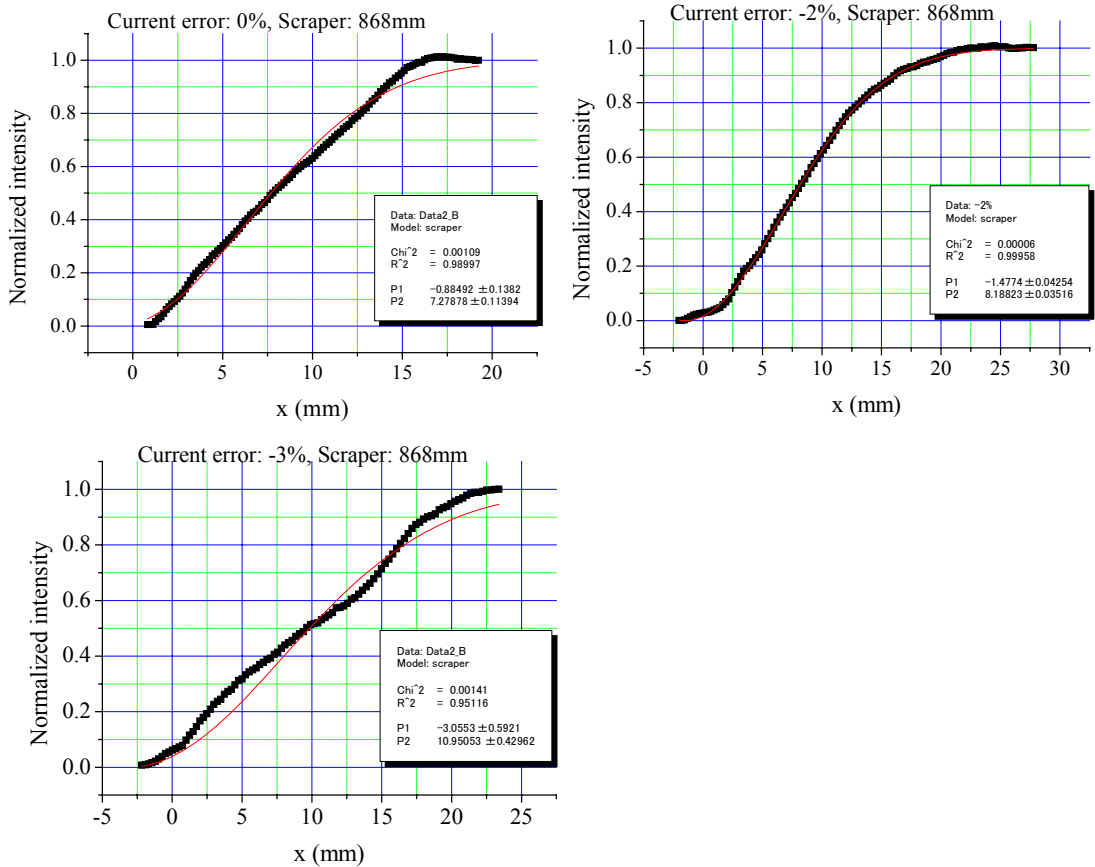


**Figure 3-19. Beam size just before crossing.**

The horizontal axis is transferred from turn number to beam position of each turn, where the origin is arbitrary determined for the convenience of fitting.

**Table 3-2. Obtained beam emittance.**

Current error	87% emittance ( $\pi$ mm-mrad.)	
	at 50keV (inj.)	around 110keV
0%	880±60	830±7.7
-2%	770±80	660±2.1
-3%	580±44	790±33

Beam emittance is likely to have an ambiguity in beam studies. A beam emittance just before crossing resonance is more important than the injected beam emittance. Since nonlinear components of magnetic field are significant in FFAG accelerators, 87% beam

emittance may increase or decrease because of smearing. Figure 3-20 shows normalized intensity in beam emittance for -2% current error.

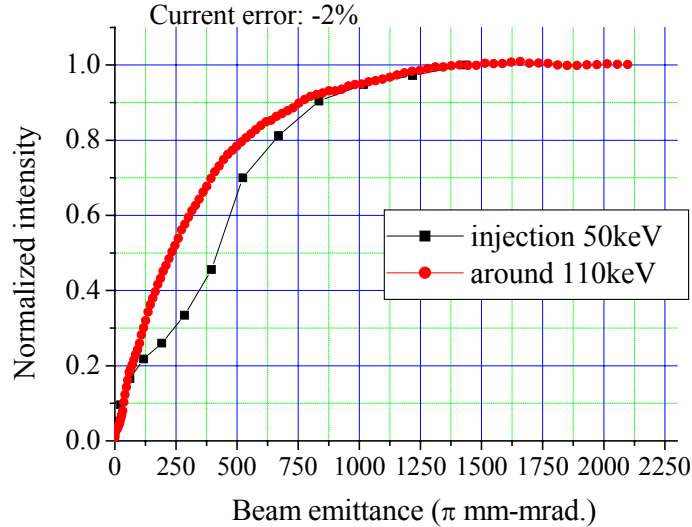


Figure 3-20. Normalized intensity in beam emittance.

Since a structure due to multi-turn injection becomes smooth after acceleration up to around 110keV as shown in Fig. 3-20, 87% beam emittance does not obey adiabatic damping exactly.

When the current error is -3%, injection beam emittance was limited due to the maximum turn number of multi turn injection. Beam emittance of -3% current error around 110keV is larger than that of injection. This is quite different from other current errors. One of the reasons for this might be that beta functions at injection energy in the experiment are different from the calculated values. As shown in Fig. 3-6, the calculated betatron tune is larger than the measured one. Since horizontal tune at injection is close to half integer, beta function is sensitive to tune. In Chapter 4, we will discuss trapping efficiency using obtained beam emittance just before crossing.

### 3.1.11 Results

Three driving terms and five crossing speeds for the total of 15 parameters were examined to study third integer resonance crossing. Data of normalized intensity for a current error of -2% with various crossing speeds are displayed in Fig. 3-21. Data for 0% and -3% current errors are in similar tendency.

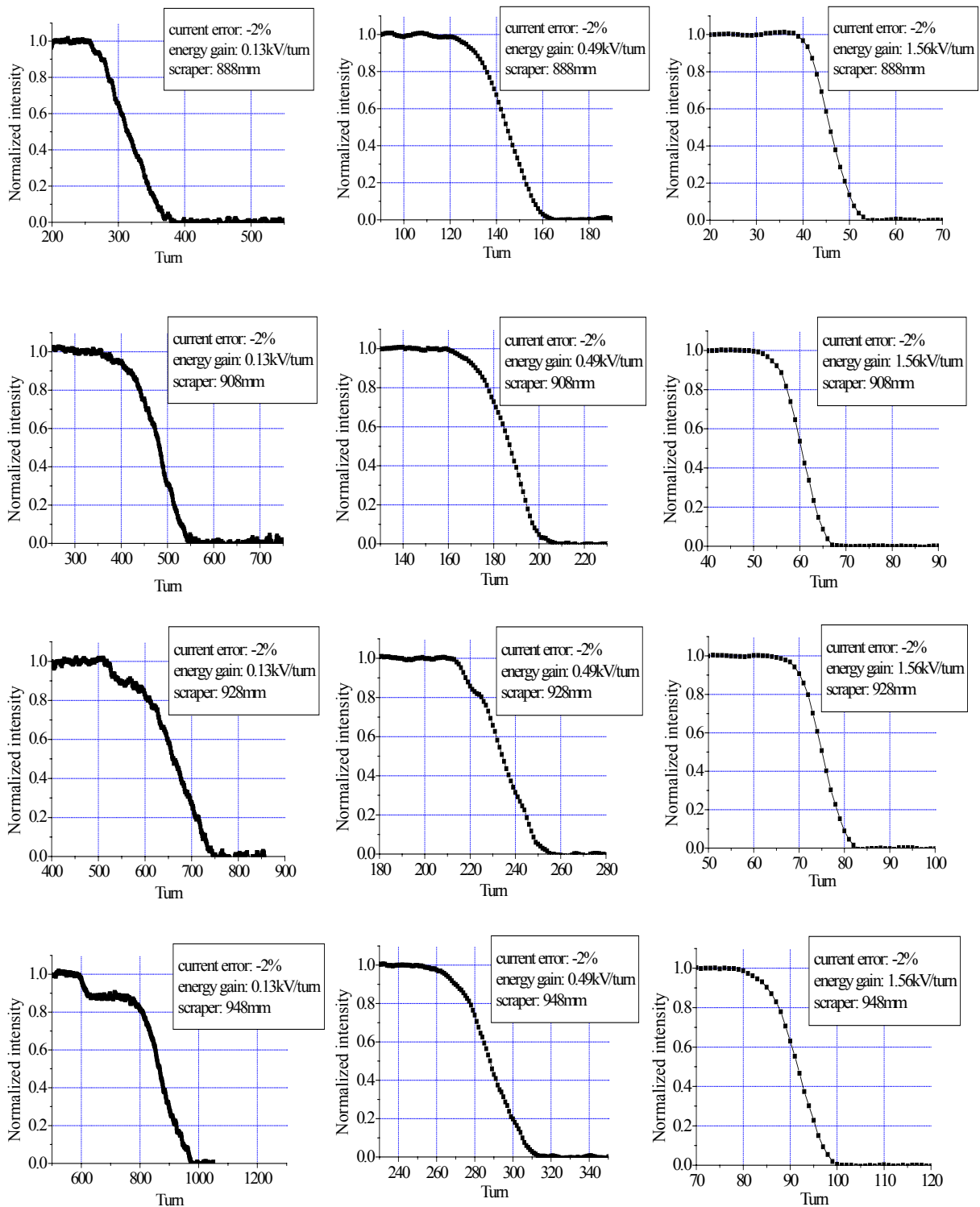
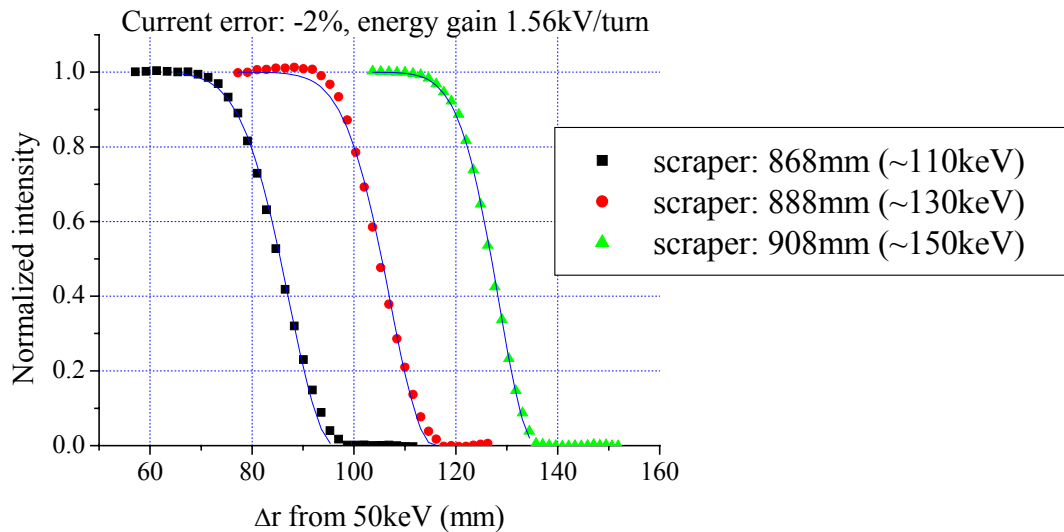
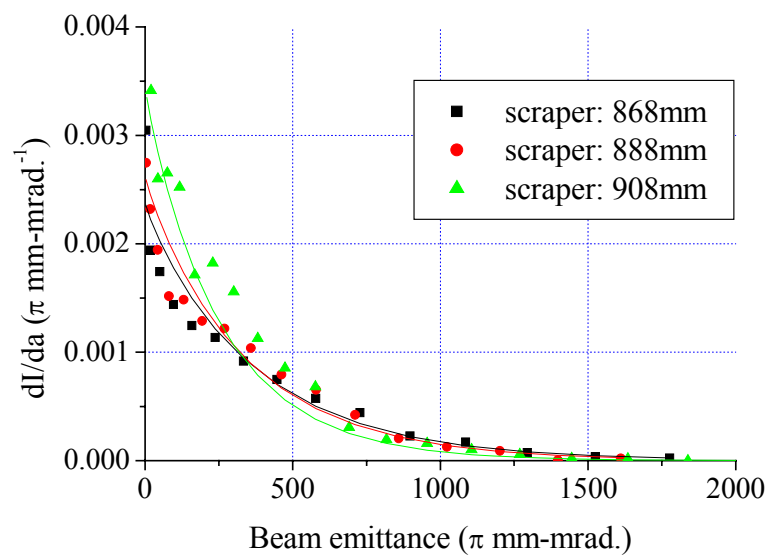


Figure 3-21. Normalized intensity curves.

In Fig. 3-21, the normalized intensity seems almost similar in shape when energy gain is large. Figure 3-22 shows normalized intensity curves for largest energy gain and those particle distributions.



(a) Normalized intensity curve for largest energy gain



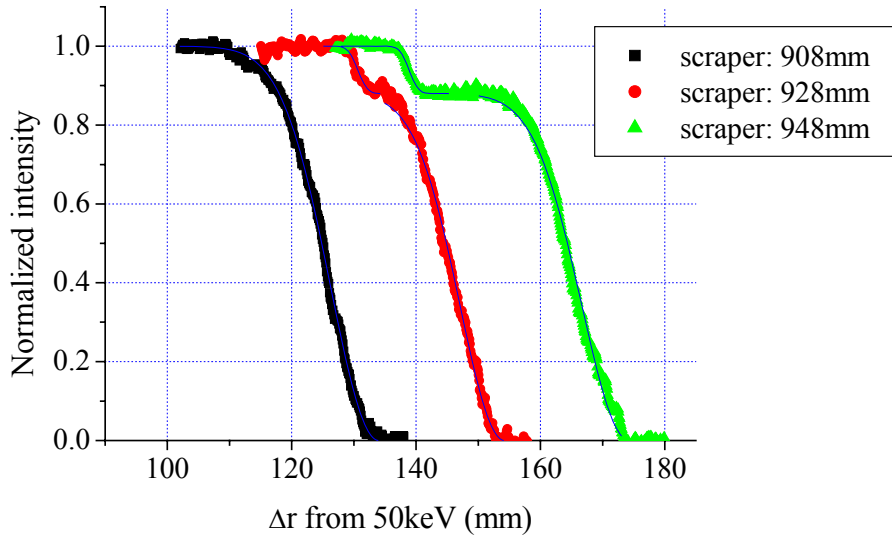
(b) Particle distribution in beam emittance for largest energy gain

Figure 3-22. Analysis result (largest energy gain).

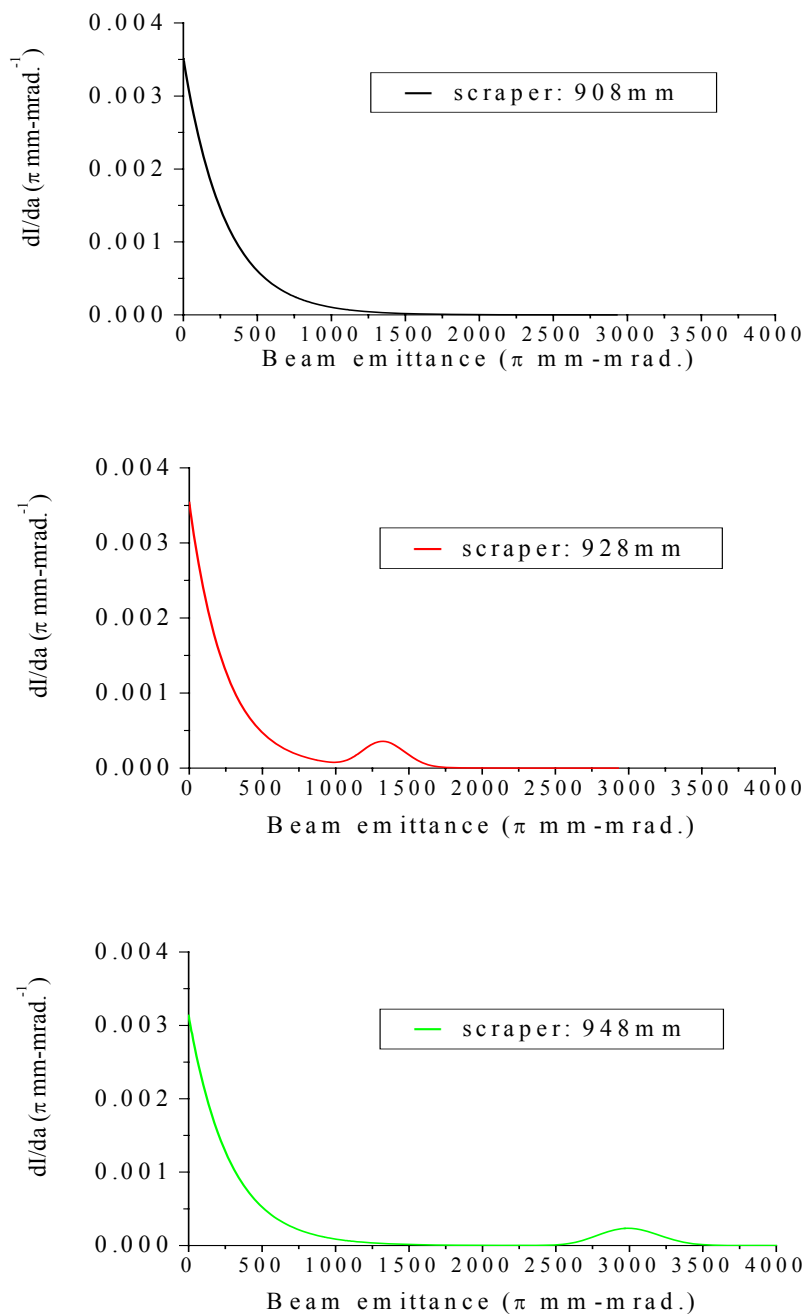
In Fig. 3-22, three scraper positions correspond to just before (868mm), in the vicinity (888mm) and right after (908mm) crossing. The particle distributions in beam emittance are concentrating on beam center in the same way during crossing because of adiabatic damping. Therefore, there must not be considerable effect due to resonance crossing when a crossing speed is fast enough.

On the other hand, a two-tier structure is clearly observed after crossing when energy gain is small. It must be due to a particle trapping because particles trapped in islands have larger amplitude than those in the beam core, thereby reaching the scraper earlier. Therefore, a decreasing curve becomes a tow-tier structure. After crossing resonance, the island center moves out. Therefore it is another evidence of particle trapping that the separation of tiers gets larger when the scraper position is varied.

This becomes clearer with the particle distribution in beam emittance. Figure 3-23 shows normalized intensity curves for smallest energy gain and those particle distributions.



(a) Normalized intensity curve for smallest energy gain



(b) Particle distribution in beam emittance for smallest energy gain

Figure 3-23. Analysis result (smallest energy gain).

As shown in Fig. 3-23, trapped particles are transported to large amplitude after crossing. This picture is the same to the model of “particle trapping”.

With normalized intensity of two-tiers structure, a trapping efficiency, which is the ratio of the number of trapped particles to the total number of particles, is obtained as shown in Fig. 3-24. The decrease in ratio in the first tier is the trapping efficiency.

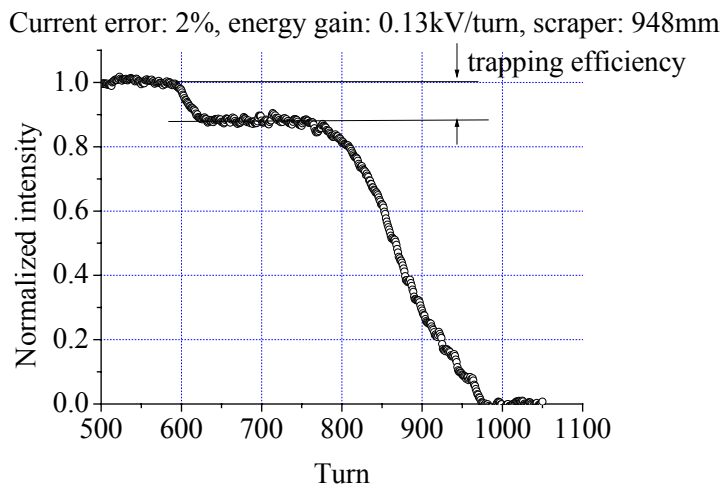


**Figure 3-24. Trapping efficiency obtained from normalized intensity curve.**

Table 3-3 shows obtained trapping efficiency.

**Table 3-3. Experimental results of trapping efficiency.**

Exp. results					
Energy gain(kV/turn)		0.13		0.21	
Current error		Efficiency (%)	Error (%)	Efficiency (%)	Error(%)
-2%		12.0	3.7	8.0	1.5
0%		17.0	1.3	11.9	1.5
-3%		22.3	2.4	15.3	3.4

In Table 3-3, trapping efficiency can be understood at least qualitatively. That is, larger driving term and slower crossing results in larger trapping efficiency. For acceleration speed more than 0.49kV/turn, we did not observe two-tier structure in normalized intensity curve. The errors in Table 3-3 are evaluated from the ambiguity in the flat part of two-tier structure. Quantitative comparison of the observed trapping efficiency with theoretical prediction and simulation results will be given in Chapter 4.

## 3.2 Resonance crossing experiment at HIMAC synchrotron

Third integer resonance crossing has also been studied at HIMAC (Heavy Ion Medical Accelerator in CHIBA) synchrotron [ 27 ] in NIRS (National Institute of Radiological Sciences). Compared with PoP beam studies, we have two advantages when we use HIMAC synchrotron. One is that it is possible to cross third integer resonance in both directions with varying quadrupole strength. The other is that beam profile can be observed directly with a gas sheet monitor.

### 3.2.1 HIMAC Accelerator

The HIMAC synchrotron is an accelerator mainly for the study of cancer therapy with heavy ion beams like He, C, Ne, Si, Ar. HIMAC synchrotron is composed of two almost identical rings called upper and lower rings. We used the lower ring for resonance crossing experiments. Figure 3-25 shows the layout of HIMAC and Fig. 3-26 shows linear lattice parameters in one super-period.

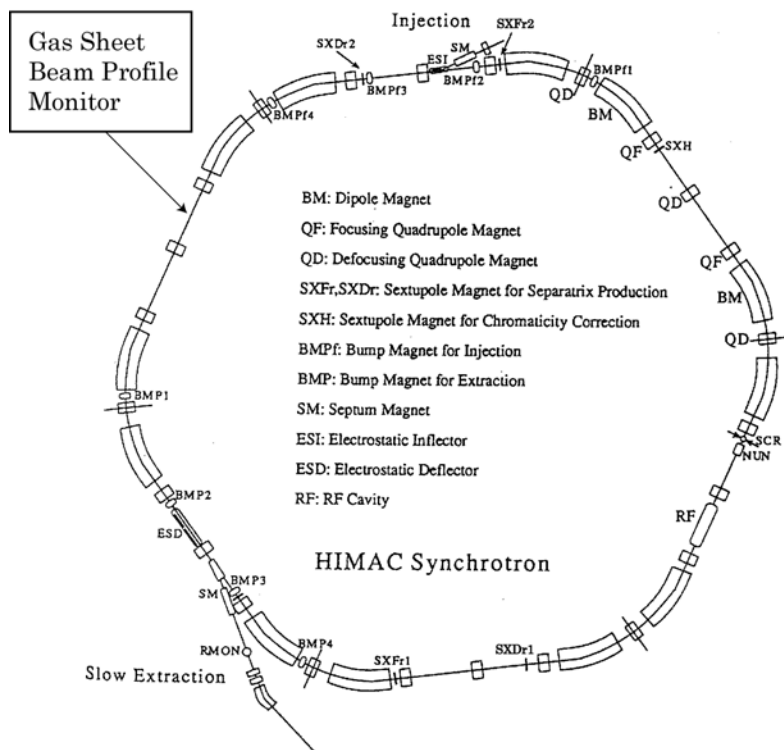
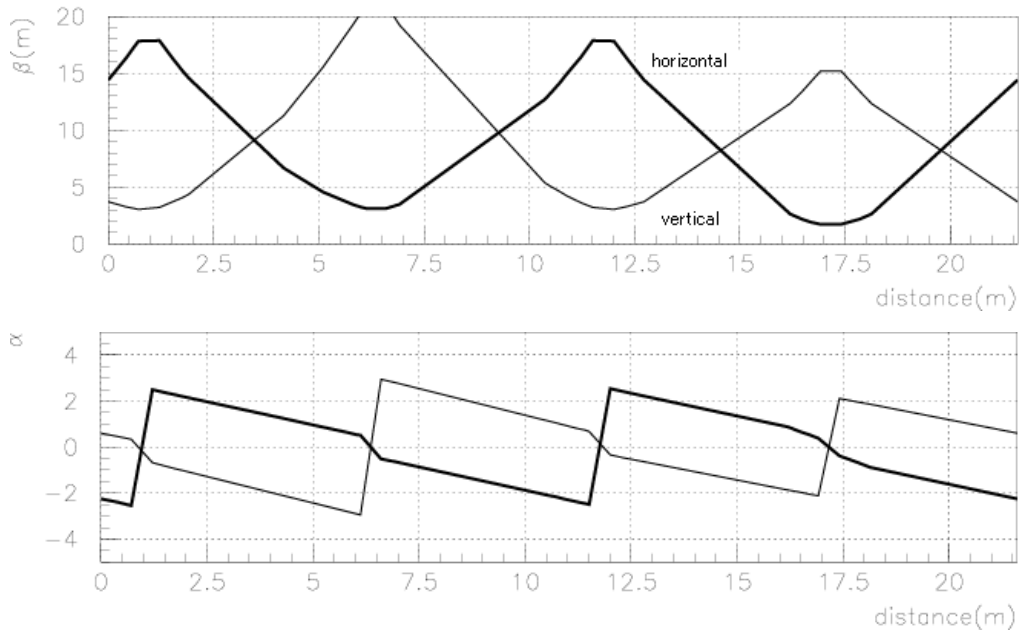


Figure 3-25. Layout of HIMAC synchrotron.

(taken from Ref.[ 27 ] and added the location of the gas sheet monitor)

As shown in this figure, the machine has six super-periods.



**Figure 3-26. Linear lattice parameters for a super-period.**

The experiment was carried out in its basic operational mode. The magnetic field strength was fixed (except for QF magnets used to change tune) and the rf cavity was not excited. Betatron tunes were close to their nominal operating values (3.69, 3.13) when crossing of horizontal resonance,  $3\nu_x=11$ , were studied.

### 3.2.2 Observation of beam profile

In order to observe the beam profile, which is a particle distribution in real space, a gas sheet beam monitor (GSBM) [ 28 ] was used. Particles of circulating beam interact with atoms in a gas sheet that is formed in the vacuum pipe. Generated electrons are transported to micro channel plates and transferred to a beam profile. We can observe beam profile directly with this monitor. The viewing field of the monitor is  $\pm 50\text{mm}$ .

### 3.2.3 Driving term and nonlinear detuning source

In order to excite driving term, 11th harmonics of sextupole, a sextupole magnet of

SXFr used for slow extraction, which is based on a third integer resonance, was employed. Unfortunately, there is no octupole as a source of nonlinear detuning. Therefore we must depend on the second order effect of sextupole component. It is known that nonlinear detuning is introduced by sextupole in the second order [ 29 ]. Chromaticity correction sextupole magnets SXH were used for this purpose. Sextupole magnets SXH are located in each super period, that is, the fundamental harmonic component excited by SXH is the six-th. It does not contribute to the driving term of resonance of  $3\nu_x=11$ . Since horizontal tune is close to and less than the structure resonance of  $3\nu_x=12$ , amplitude dependence of tune is positive.

### 3.2.4      **Tune variation**

In order to let horizontal tune cross resonance, the strength of focusing quadrupole magnets QF were varied in time and mainly the horizontal tune was changed. Crossing speed can be varied from zero to  $5.86 \times 10^{-6}$ /turn. The maximum speed of crossing is limited by the quadrupole power supply.

### 3.2.5      **Parameters for the beam study**

Typical four major parameters, i.e., crossing speed, driving term, nonlinear detuning and beam emittance are shown in Table 3-4.

**Table 3-4. Typical parameters of experiment.**

K2L of sextupole for injection energy is  $4.1/m^2$ /magnet with current of 130A.

Parameter	
Crossing speed	4.6e-6/turn
Nonlinear detuning (SXH curr.)	$2.52m^{-1}$ (5A)
Driving term (SXFr curr.)	$0.019m^{-1/2}$ (0.32A)
Average emittance	$30\pi mm \cdot mrad.$
Average beam size at monitor	17.3mm(half)

The emittance at injection is chosen to be within the monitor range. The strength of nonlinear detuning due to sextupole SXH is limited because of dynamic aperture and beam injection efficiency. Too strong a sextupole may make dynamic aperture small and to interfere with efficient beam injection.

### 3.2.6      **Experimental results**

#### **I. Crossing in the direction of tune decreasing**

Figure 3-27 shows successive beam profiles during crossing. The parameters are those given in Table 3-4.

The crossing direction of tune decreasing is the one of “particle trapping” because amplitude dependence of tune is positive. In Fig. 3-27, we can see clearly that some part of the beam is trapped and carried out of monitor range.

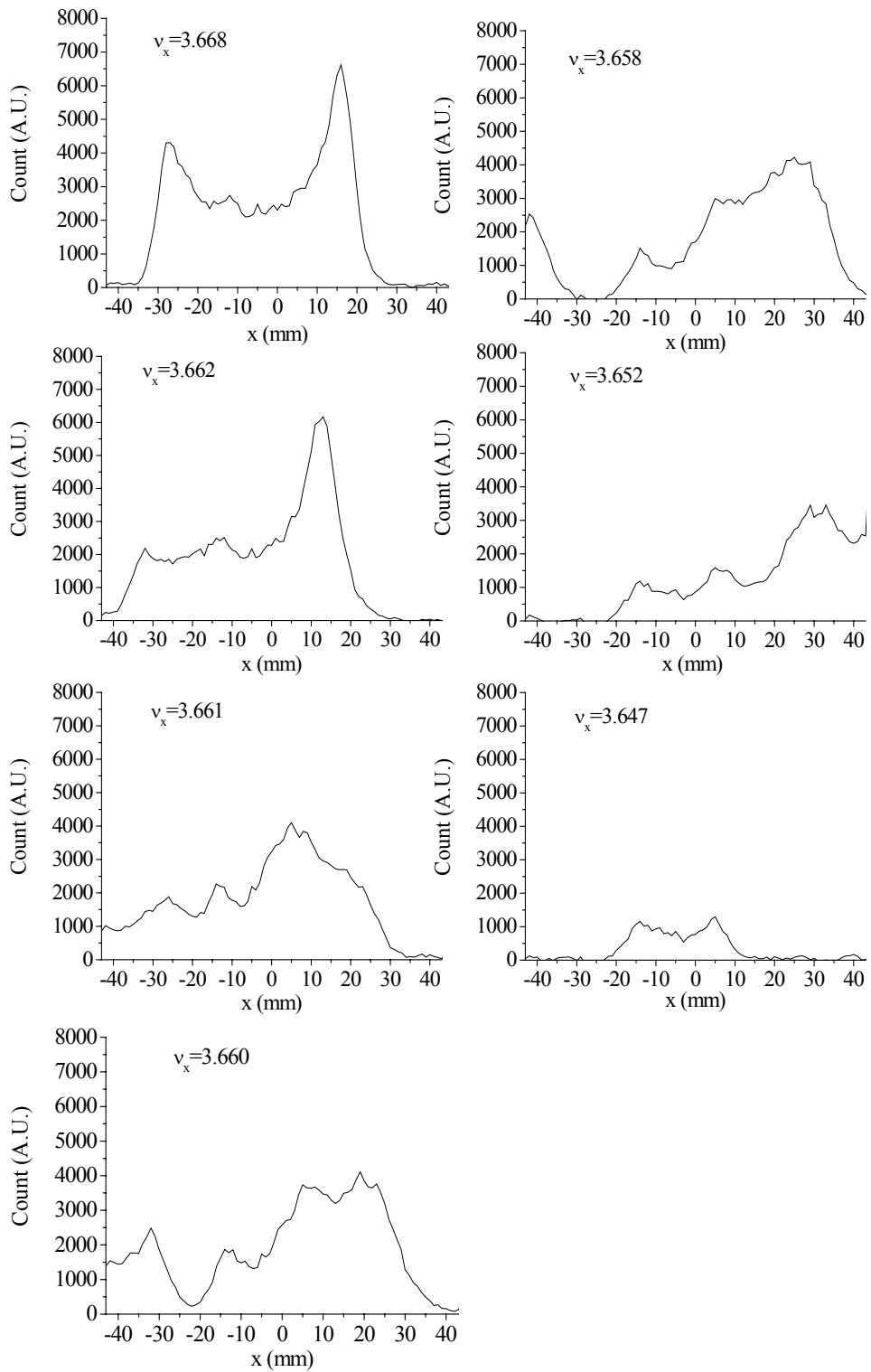


**Figure 3-27. Successive beam profiles during crossing (tune increasing).**

After crossing resonance, beam profile starts to deform. When tune becomes 3.660, we can see a left part of beam disengages from beam core and finally get out of monitor range. The right part of beam also disengages. Only beam core remains after crossing resonance.

## II. Crossing in the direction of tune increasing

Resonance crossing in the direction of tune increasing was also carried out. Crossing direction was reversed keeping all other parameters the same as in the direction of tune decreasing. Figure 3-28 shows successive beam profiles during crossing.

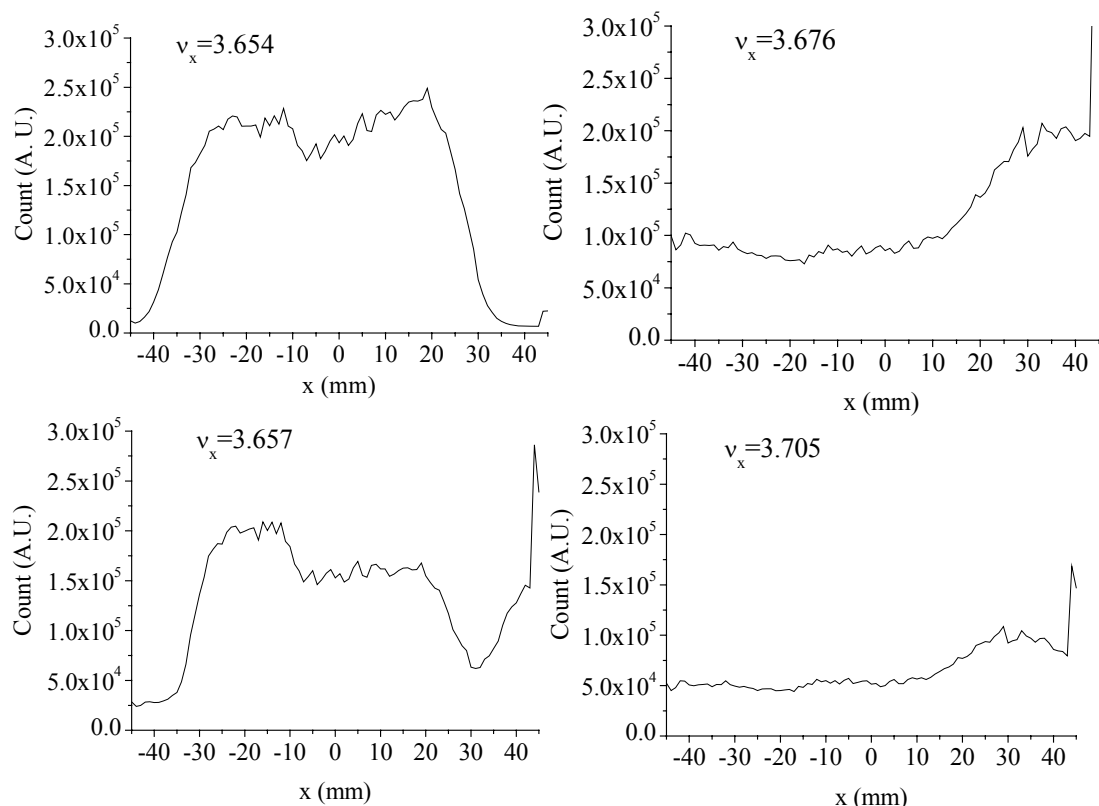


**Figure 3-28. Successive beam profiles during crossing (tune decreasing).**

In Fig. 3-28, the beam profile after crossing is qualitatively different from crossing in the direction of tune decreasing. In this direction, beam size grew beyond monitor range and a growth in beam emittance but no clear sign of trapping was observed. These results will be closely discussed in Chapter 4.

## Chapter 4

# Discussion and Conclusion

As described in Chapter 3, third integer resonance crossing was examined at PoP FFAG and HIMAC. We discuss the experimental results comparing them with theoretical predictions or simulation results or with both. Finally, the summary of the main conclusions of this study is presented.

### 4.1 Discussion on experimental results at PoP FFAG

In the experiment at PoP FFAG, various driving terms and crossing speeds were examined for a third integer resonance. We observed “particle trapping” clearly with relatively slow crossing and no damage with relatively fast crossing. Qualitatively speaking, the dependence of trapping efficiency on crossing speed and driving term is understandable quite well. That is, stronger driving term and slower crossing result in larger trapping efficiencies. In order to understand experimental results quantitatively, theoretical calculation and simulations are performed to estimate trapping efficiency.

In Sec.2.4.1, we got theoretical trapping efficiency (see Eq.( 2-51 ))

$$P_t = \frac{\pi}{\sqrt{2}} \kappa^{-1/2} \alpha_s^{-1/4} \exp(-\alpha_1), \quad (4-1)$$

where

$$\alpha_s^{1/2} \approx \begin{cases} \alpha_1^{1/2}, & \text{if } \alpha_1 > 1, \\ 1, & \text{if } \alpha_1 < 1 \end{cases}. \quad (4-2)$$

$\alpha_1$  is the adiabatic parameter,

$$\alpha_1 = \left( \frac{\varepsilon}{4\pi\Delta_{NL}\Delta_e} \right)^{\frac{2}{3}}, \quad (4-3)$$

and  $\kappa$  is

$$\kappa = 3\Delta_{NL}/4\Delta_e . \quad (4-4)$$

Furthermore,  $\kappa$  is expressed with the driving term  $|A_p|$ , the nonlinear detuning  $B_0$  and the average emittance  $a_0$ ,

$$\kappa = \frac{3B_0 a_0^{1/2}}{|A_p|} . \quad (4-5)$$

Driving term and nonlinear detuning can be obtained numerically as described in Appendix C. Table 4-1 lists them for three current errors.

**Table 4-1. Driving term and nonlinear detuning.**

Current error	0%	-2%	-3%
Driving term $ A_p $ ( $m^{-1/2}$ )	$1.30*10^{-2}$	$1.04*10^{-2}$	$1.51*10^{-2}$
Nonlinear detuning $B_0$ ( $m^{-1}$ )	$3.63*10^{-1}$	$4.06*10^{-1}$	$4.22*10^{-1}$

The symbol  $\varepsilon$  in Eq.( 4-1 ) is the crossing speed, that is, the change of tune per revolution. It is obtained with the relation between betatron tune and beam energy shown in Fig. 3-6.

Once energy dependence, a slope of tune to beam energy, is known, crossing speed is determined as the product of this slope and energy gain. The betatron tune is assumed to be linear dependent on energy in the neighborhood of crossing point. We then find all parameters in Eq.( 4-1 ) for the trapping efficiency.

Simulations are carried out with RK tracking, which is described in Appendix B. The initial particle distribution is assumed to be Gaussian distribution. Average emittance is determined from the estimated beam emittance just before crossing. The motion is confined on the median plane and the energy gain is constant so as to exclude vertical and longitudinal motions. Although the effects of these motions are not included in the theory, they are nevertheless important since a beam must have a finite emittance in vertical as well as longitudinal phase space. They will be discussed later respectively. The simulation results have statistical error. As described in Ref.[ 18 ], it is evaluated as

$$\Delta P_T = \pm \frac{\sqrt{m(1-m/n)}}{n}, \quad (4-6)$$

where  $n$  is the number of total particle and  $m$  is the number of trapped particle. For  $n=350$ , the statistical error is expected to be less or comparable to the error of experiment results. Figure 4-1 and Table 4-2 show the summary of trapping efficiencies.

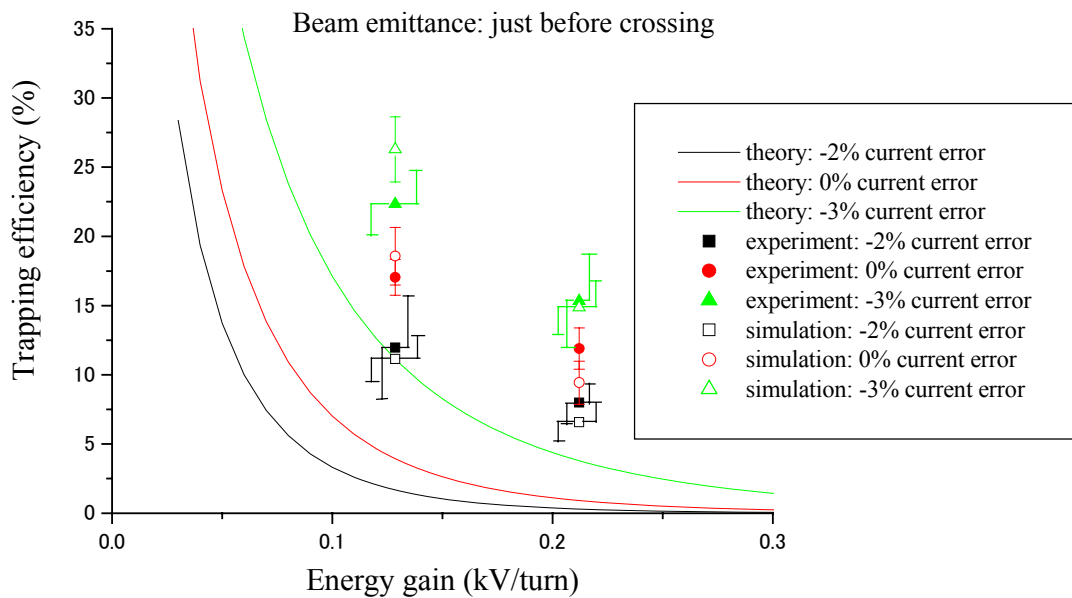


**Figure 4-1. Summary of obtained trapping efficiencies.**

**Table 4-2. Summary of obtained trapping efficiencies.**

Experimental results			
Energy gain(kV/turn)	0.13	0.21	
Current error	Efficiency (%)	Error (%)	Efficiency (%)
-2%	12	3.7	8
0%	17	1.3	11.9
-3%	22.3	2.4	15.3

Simulation			
Energy gain (kV/turn)	0.13	0.21	
Current error	Efficiency (%)	Error (%)	Efficiency (%)
-2%	11.1	1.7	6.6
0%	18.6	2.1	9.4
-3%	26.3	2.4	14.9

The trapping efficiency obtained in experiment shows a good agreement with simulation when the beam emittance just before crossing is used. The theoretical predictions are much lower. It is believed that this is due to the fact that  $\kappa$  in 2.4.1 does not satisfy the assumption  $\kappa \gg 1$ .  $\kappa$  is in the range from 1.6 to 2.1 in this experiment.

We discuss the uncertainty in the obtained efficiency due to ambiguity of following factors.

- I. Crossing speed: effect of synchrotron oscillation
- II. Driving term: accidental driving term caused by magnet misalignments
- III. Nonlinear detuning: effect of vertical motion
- IV. Beam emittance: emittance of the beam in the experiment

These four factors are naturally major parameters of resonance crossing. In the following investigations, parameters listed in Table 4-3 are used as representative one.

With the parameters, trapping efficiency by theoretical prediction becomes 9%.

**Table 4-3. Representative parameters for investigation.**

The 87% emittance is based on the measurement of beam emittance. Considering adiabatic damping, beam emittance around crossing energy of 130keV is obtained from one around 110keV.

Current error	-3%
Driving term $ A_p $	$1.51 \times 10^{-2} (\text{m}^{-1/2})$
Nonlinear detuning $B_0$	$4.22 \times 10^{-1} (\text{m}^{-1})$
Excitation width	$-7.16 \times 10^{-4}$
Tune shift at $a_0$	$-1.27 \times 10^{-3}$
87% emittance $a_0$	$720\pi (\text{mm-mmrad.})$
Crossing speed	$8.83 \times 10^{-5}$
Energy gain	0.13 (kV/turn)

## I. Crossing speed

Crossing speeds for individual particles in a bunched beam are not the same because of synchrotron oscillation. A variation of crossing speed may or may not cause a net change in trapping efficiency effectively. If the period of synchrotron oscillation is very much shorter than the period for particle trapping, the effect of synchrotron oscillation should not be significant because the average crossing speed for any particle would nearly be the same as the speed of synchronous particle. If, on the other hand, the period of synchrotron oscillation is much longer, different particles would have different crossing speed depending on their phase at the time of crossing. In the latter case, trapping efficiency should increase because the dependence of efficiency is not inversely proportional to the acceleration speed and its second derivative with respect to the energy gain is positive as seen in Fig. 4-1. Figure 4-2 shows a mountain view plot during crossing.

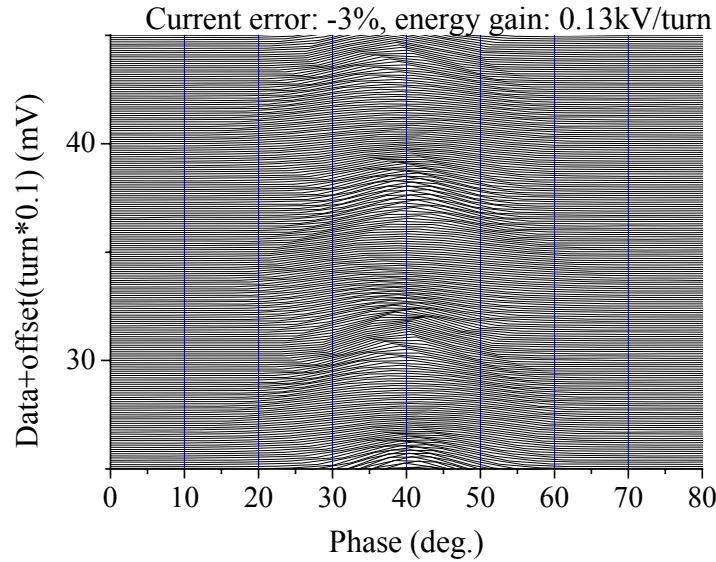


**Figure 4-2. Mountain view plot during crossing.**

We can see that the maximum range of rf phase is approximately  $\pm 15\text{deg}$  with ignoring the tail of bunch and a quadrupole mode of synchrotron oscillation is prominent. The maximum estimate is obtained numerically by taking average integral of trapping efficiency over the maximum range. Theoretical efficiency for representative parameter is increased from 9.0% to 10.4% by taking average integral. Therefore the maximum estimate says a possibility of 16% relative increase in trapping efficiency. Table 4-4 shows an estimate of how much the phase of synchrotron oscillation advances during trapping process.

**Table 4-4. Estimate of synchrotron phase advance during crossing process.**

Synchrotron tune	$1.5 \times 10^{-2}$
$\Delta_L$ for $\alpha_s=3$	$4.4 \times 10^{-3}$
Number of turn during trapping	44
Phase advance during trapping	240deg.

We find that the period of synchrotron oscillation is shorter than the time in which the stable fixed points reach  $\alpha_s=3$ . Therefore the effect of synchrotron oscillation may increase trapping efficiency but it might be less than the maximum estimate.

The effect is also evaluated with RK tracking simulation more precisely. In order to clarify the dependence of efficiency upon synchrotron oscillation phase, initial longitudinal condition is chosen as shown in Fig. 4-3. Table 4-5 lists result of tracking simulation.

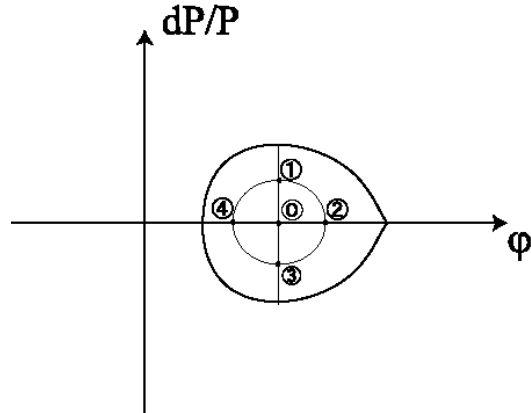


Figure 4-3. Initial condition for simulation.

Table 4-5. Simulation results for longitudinal motion.

The amplitude of synchrotron oscillation is set  $\pm 10\text{deg}$ . It is typical oscillation amplitude.

Initial condition	Trapped	Total	Efficiency (%)	Error(%)
0	92	350	26.3	2.4
1	90	350	25.7	2.3
2	87	350	24.9	2.3
3	96	350	27.4	2.4
4	107	350	30.6	2.5
Average 1-4	380	1400	27.1	1.2

It is seen that the trapping efficiency varies with the initial phase. However, the efficiency averaged over phase is almost the same to that of synchronous initial condition. Even when the quadrupole mode of synchrotron oscillation is strong, the averaged efficiency should not vary much because particles in anti-phase balance each other. We can neglect the effect of synchrotron oscillation, at least when the bunch

length is less or equal to that of this experiment.

However, we have to note a possibility of multiple crossing. When synchronous phase is very small so that the rf bucket covers a region of negative rf voltage, a particle with a large amplitude may experience not only acceleration but also deceleration. Then there is a possibility to cross resonance more than twice. It may then be a totally different situation from the one we have discussed here.

## II. Driving term

Figure 4-4 shows a dependence of trapping efficiency on driving term.

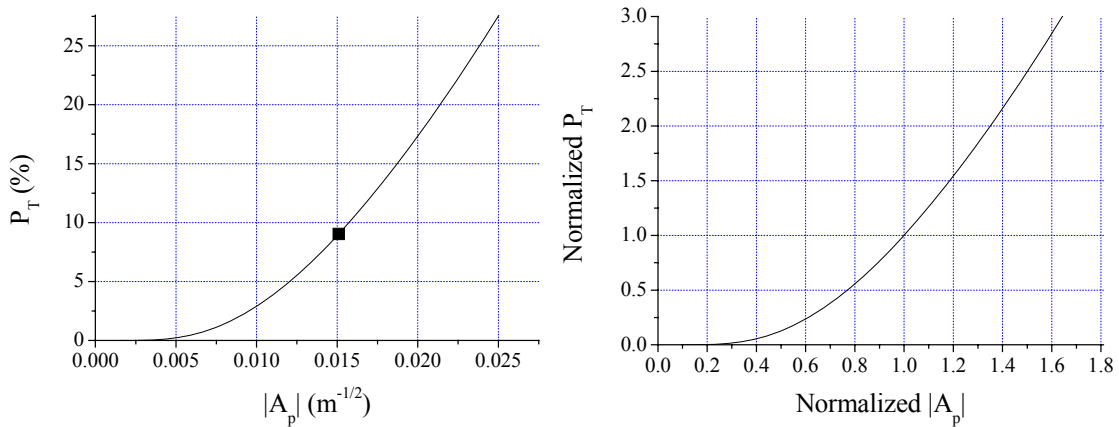


**Figure 4-4. Dependence of trapping efficiency on driving term.**

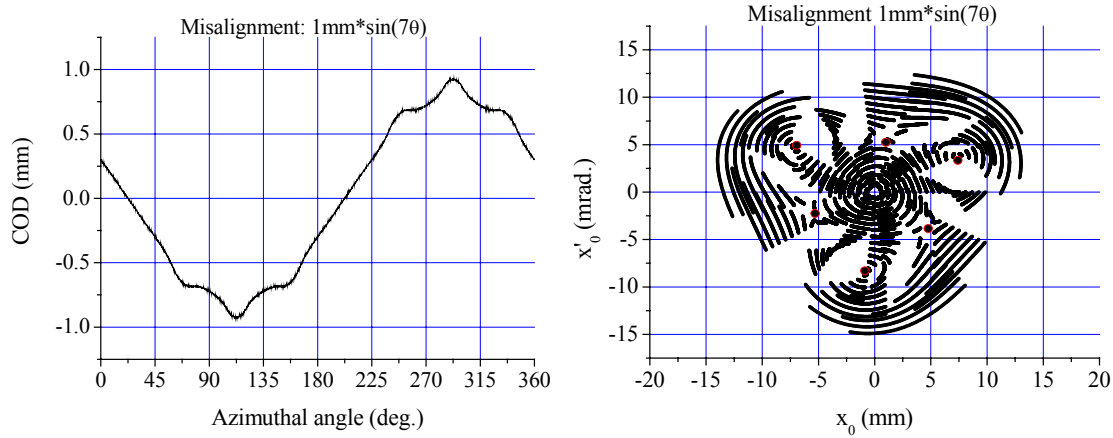
The right side figure is normalized by the value of representative parameter (Black square in the left figure).

Figure 4-4 is obtained from the theoretical trapping efficiency Eq.( 4-1 ) and the slope of normalized trapping efficiency to driving term is 2.5. This means, for example, trapping efficiency changes 2.5% relatively when driving term changes 1%. In the figure, a stronger driving term naturally leads to a larger efficiency. In theory and simulation, trapping efficiencies are calculated excluding accidental driving term. If there is a large accidental driving term, the estimated trapping efficiencies in theory and simulation change considerably.

We assume that the accidental driving term is mostly caused by magnet misalignments. In order to evaluate the maximum possible magnitude, a distribution of misalignments

is chosen artificially. When magnets are shifted along  $\sin(p\theta)$ , the driving term of p-th harmonics will be induced most strongly. The driving term with a displacement of  $1\text{mm} \cdot \sin(7\theta)$  is calculated. Since it is difficult to compute a driving term that is too small, an artificially large magnitude of misalignment is examined. Once the driving term with 1mm amplitude is known, one with reasonable amplitude can be approximately obtained by an interpolation. Figure 4-5 shows COD and motions in phase space with this misalignment.

With 1mm alignment error, the driving term is  $3.43 \cdot 10^{-3} \text{m}^{-1/2}$ . If we assume that an alignment error of 0.1mm and that the accidental driving term is proportional to the magnitude of alignment error, accidental driving term is only 2.3% relative to that of representative parameter. It is only 3.3% even compared with the smallest driving term for -2% current error. Since the alignment error should be random, the accidental driving term should be much smaller than the present estimate. Therefore, the accidental driving term must be negligible and it should change trapping efficiencies only slightly. Actually, this situation was anticipated in the planning of experiment by introducing a large COD to create the driving term.



**Figure 4-5. COD and motions in phase space with misalignment.**

### III. Nonlinear detuning

Figure 4-6 shows a dependence of trapping efficiency on nonlinear detuning and the slope of normalized trapping efficiency to nonlinear detuning is 1.5.

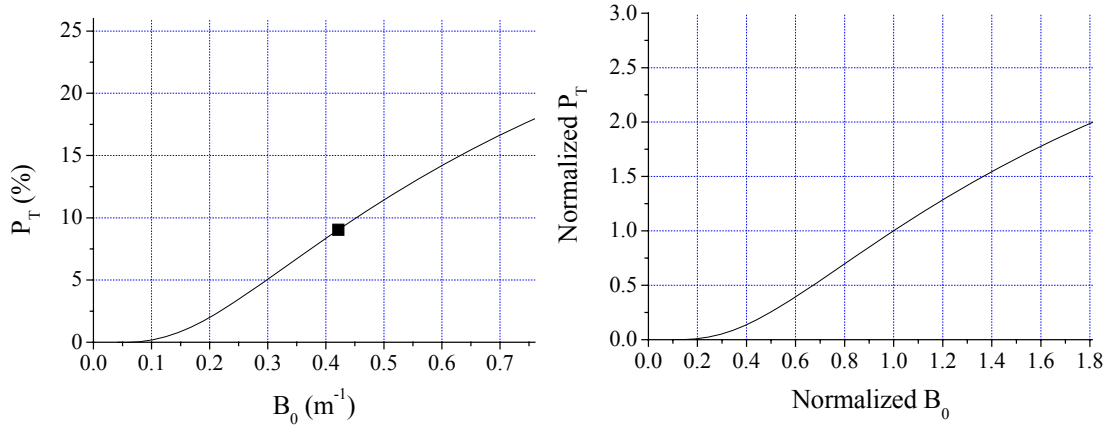


**Figure 4-6. Dependence of trapping efficiency on nonlinear detuning.**

As described above, accidental driving term is negligible. Nonlinear detuning may be more insensitive to misalignment since it is zero-th harmonics. A possible factor to change nonlinear detuning is vertical motion. When the octupole field off the median plane is taken into account, a perturbation Hamiltonian of octupole is

$$H_{oct}^{(1)} = O(\theta) \left( \frac{3}{8} a_x^2 \beta_x^2 - \frac{3}{2} a_x a_y \beta_x \beta_y + \frac{3}{8} a_y^2 \beta_y^2 \right), \quad (4-7)$$

where  $a$  is the canonical variable for oscillation amplitude,  $\beta$  is the beta function of Courant-Snyder and subscripts  $x$  and  $y$  denote horizontal and vertical motion respectively.

Taking a partial differentiation of Eq.( 4-7 ) with respect to  $a_x$ , we get

$$\varphi'_x = \frac{\partial H_{oct}^{(1)}}{\partial a_x} = O \left( \frac{3}{4} a_x \beta_x^2 - \frac{3}{2} a_y \beta_x \beta_y \right), \quad (4-8)$$

where  $\varphi_x$  is the canonical variable paring with  $a_x$  and  $\varphi'_x$  is the derivative with respect to  $\theta$ .

This equation shows that the nonlinear detuning is a combination of  $a_x$  and  $a_y$  terms. Since  $a$  and  $\beta$  are always positive, pure horizontal nonlinear detuning (the first term) is weakened by the second term or, if the second term is larger than the first term, its sign is reversed.

We evaluate approximately the effect of vertical motion represented by the second term. Assume that the  $a_x$  and  $a_y$  are  $720\pi$  and  $30\pi$  mm-mrad. They are the 87% emittance and the average emittance, respectively, at the crossing energy (about 130keV). In the theory of “particle trapping”, “typical trapping amplitude” is defined as in Eq.(2-50). “Typical trapping amplitude” of representative parameter is about  $1,000\pi$  mm-mrad. Since the ratio of particles included more than  $1,000\pi$  mm-mrad is only 6%,  $1,000\pi$  mm-mrad seems too large to be the typical particle amplitude. Therefore, the 87% emittance for horizontal is used instead of “typical trapping amplitude”.

The octupole component may be mainly in the main body of focusing and defocusing magnet. Figure 4-7 shows the beta function (without COD).

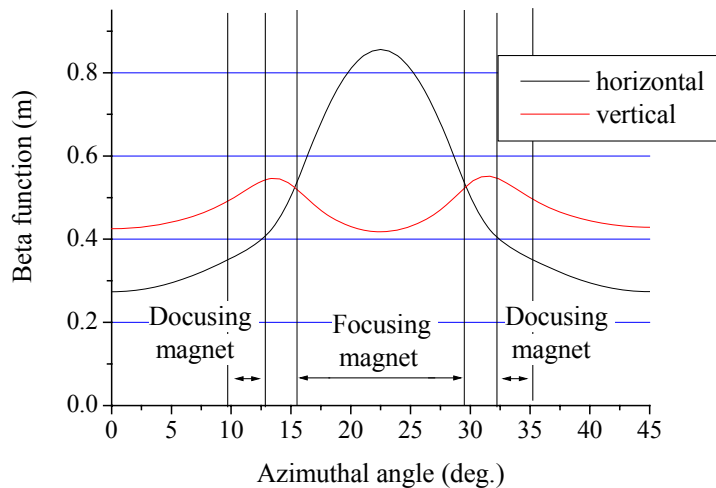


Figure 4-7. Beta function (without COD).

In the region of focusing and defocusing magnet, average beta function are ( $\beta_x$ ,  $\beta_y$ )=(0.73m, 0.46m) and ( $\beta_x$ ,  $\beta_y$ )=(0.38m, 0.52m) respectively.

Table 4-6 summarizes this estimation.

Table 4-6. Estimation of the effect of vertical motion.

	First term	Second term	abs(Second/First)
Focus	1	-0.05	0.05
Defocus	-0.11	0.012	0.11
Sum	0.89	-0.038	0.042

In Table 4-6, the values are normalized at the first term of focusing magnet. Note that FD ratio, that is, the ratio of focusing field to defocusing field is now 2.43, that is, integrated octupole component in focusing magnet is 2.43 times larger than defocusing magnet. As shown in Table 4-6, the effects of vertical motion in focusing and defocusing magnet cancel each other. Trapping efficiency is decreased about 6.3% relatively due to the effect of vertical motion.

#### IV. Beam emittance

Figure 4-8 shows a dependence of trapping efficiency on beam emittance and the slope of normalized trapping efficiency to beam emittance is 2.7. Table 4-7 lists obtained beam emittance (see Tab. 3-2).

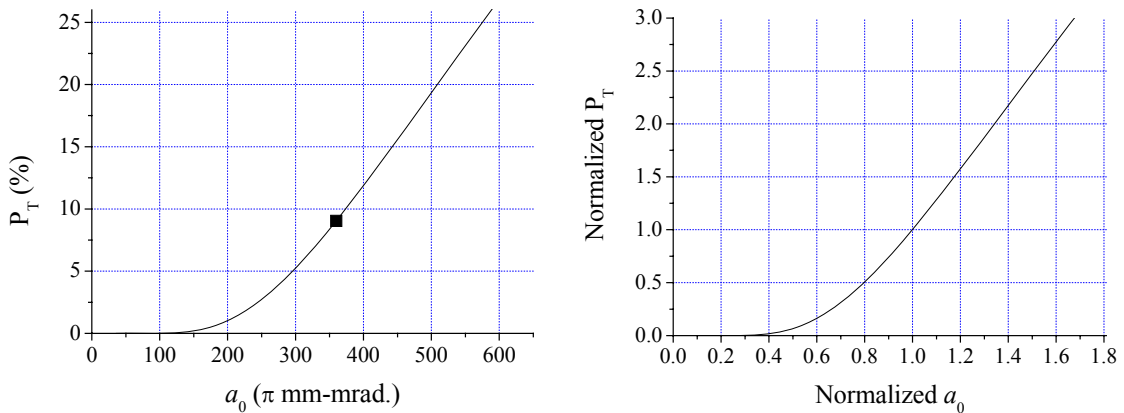


**Figure 4-8. Dependence of trapping efficiency on beam emittance.**

**Table 4-7. Beam emittance just before crossing.**

Current error	87% emittance ( $\pi$ mm-mrad.)	
	at 50keV (inj.)	around 110keV
0%	880±60	830±7.7
-2%	770±80	660±2.1
-3%	580±44	790±33

When the error of beam emittance is assumed to be  $\pm 4\%$  (corresponding to  $-3\%$  current error, 110keV), trapping efficiency has an relative ambiguity of  $\pm 11\%$ . Therefore beam emittance is largest factor to affect the estimation of trapping efficiency.

Summarizing the above investigation, we can conclude that the most sensitive parameter for trapping efficiency in this experiment is the beam emittance and that the trapping efficiency is changed relatively about 10%. Nevertheless the trapping efficiency obtained in experiment shows a good agreement with simulation when the errors in experiment and simulation are also about 10%.

Figure 4-9 shows the dependency of the trapping efficiency on adiabatic parameter.

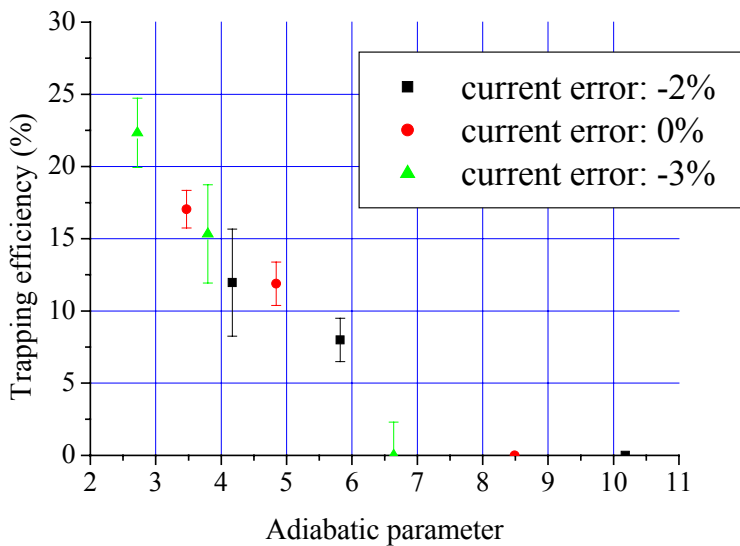


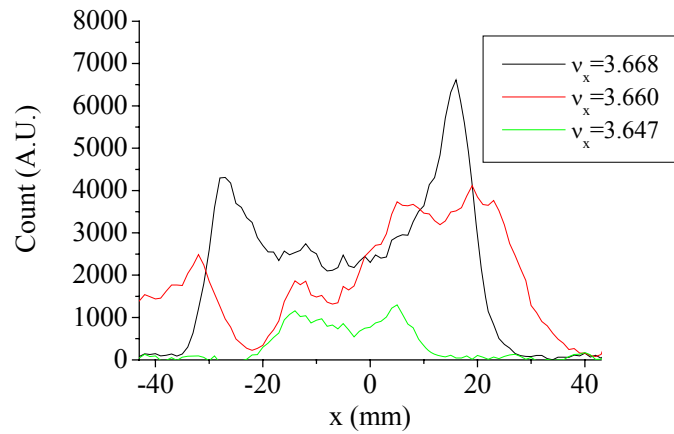
Figure 4-9. Dependence of trapping efficiency on adiabatic parameter.

In the experiment, it was observed that there was no trapped particle when energy gain is more than 0.49kV/turn. It corresponds to adiabatic parameter of 6.6 for  $-3\%$  current error (current error of  $-3\%$  leads smallest adiabatic parameter among three current errors for the same energy gain).

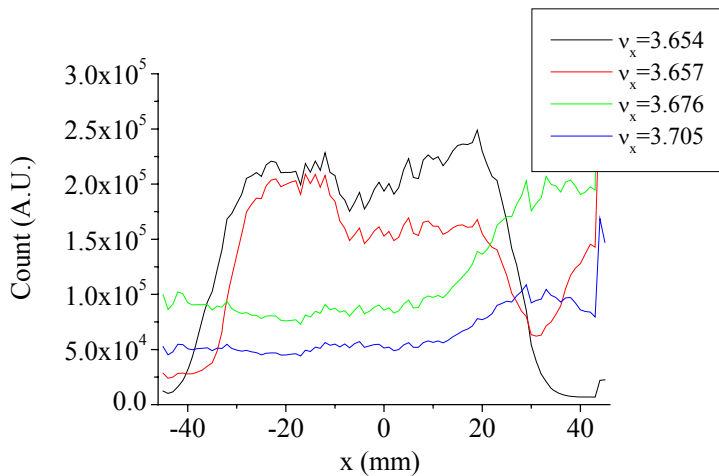
Adiabatic parameter means how fast the center of islands move compared with a speed of particle moving in oscillation amplitude and contains all major parameters, crossing speed, driving term, nonlinear detuning and beam emittance. Therefore it is general parameter to estimate how crossing is fast. In general, smaller adiabatic parameters might be permitted since  $\kappa$  in Eq.( 4-1 ) would be larger than this experiment. Therefore, a crossing with adiabatic parameter of more than 7 must be quite harmless.

## 4.2 Discussion on experimental results at HIMAC

In HIMAC experiment, beam profiles during crossing were obtained for both crossing directions. The results are shown again in Fig. 4-10.



(a) Beam profiles in the direction of tune decreasing



(b) Beam profiles in the direction of tune increasing

Figure 4-10. Results of HIMAC experiment.

It was clearly observed that a qualitative difference in two directions of crossing, that is, only beam core remains in one direction and a beam size grows in the reverse direction. In order to understand the experimental results, the crossing of  $3v_x=11$  in HIMAC is reproduced. A method of simulation is a tracking in one degree-of-freedom using transfer matrix described in Appendix E. In the simulation, the lattice of HIMAC is reconstructed and the parameters are set to be the same in the experiment. Figure 4-11 shows simulation results of the particle distributions in phase space and beam profiles during crossing in the direction of tune decreasing.

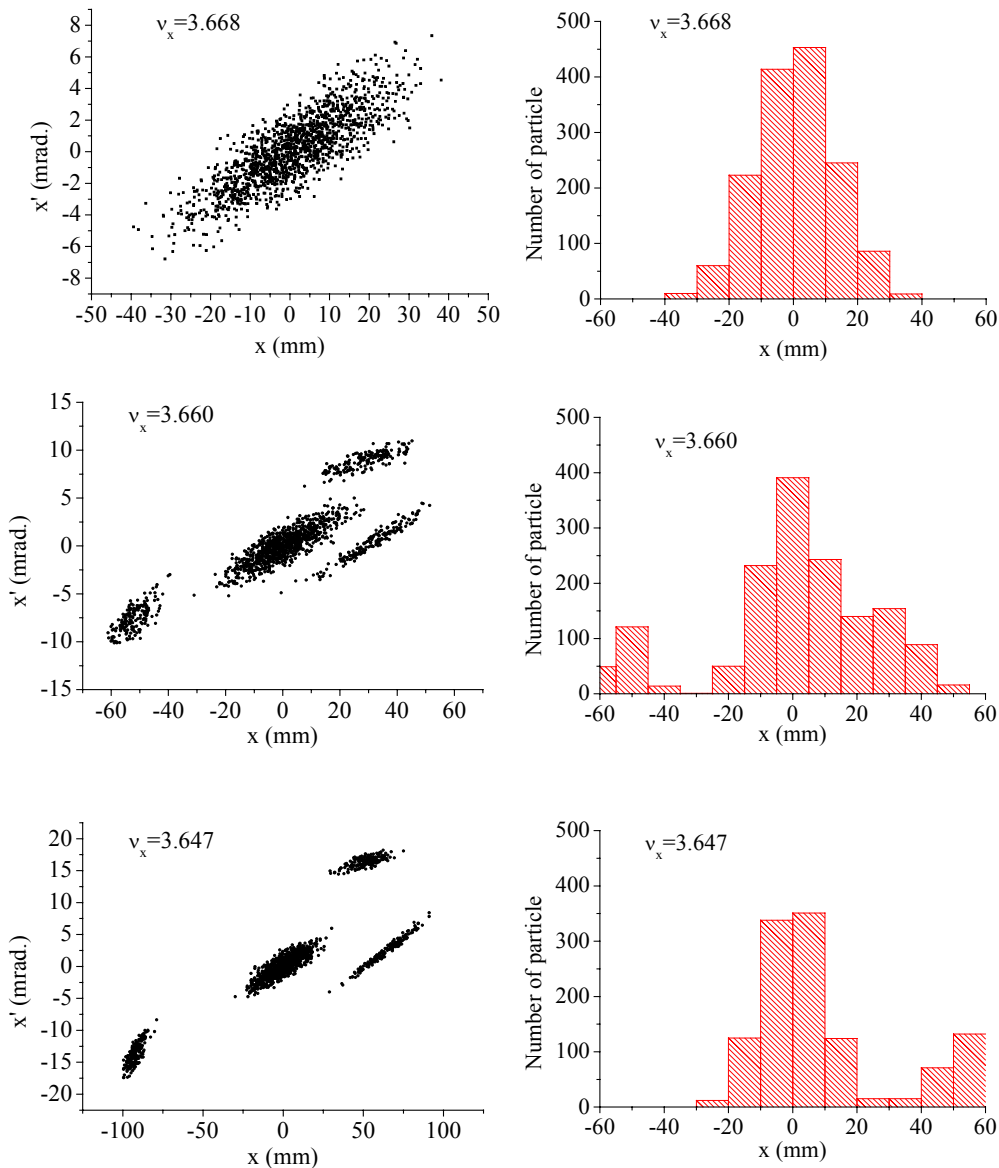


**Figure 4-11. Simulation results of the direction of tune decreasing.**

The observed beam surviving in Fig. 4-10(a) was about 15% and much smaller than simulation, which is about 65% in Fig. 4-11. The reasons for the discrepancy are considered as follows.

In the experiment, crossing speed is almost constant even for particles with different momentum because tune is varied with changing of the field in quadrupole magnet QF. Then, the remaining factors are driving term, nonlinear detuning and beam emittance.

Since nonlinear detuning is limited by the dynamic aperture and beam injection requirements, the driving term should also be correspondingly small if the trapping model is to be applied. The actual driving term tends to be larger than what the model requires. This is contrary to PoP experiment. Since the maximum field strength of sextupole driving term is a few Gauss, one possible source of accidental driving term is the remnant field of sextupole magnet SXH. Sextupole field excited as an allowed pole of bending magnets may also contribute to the accidental driving term.

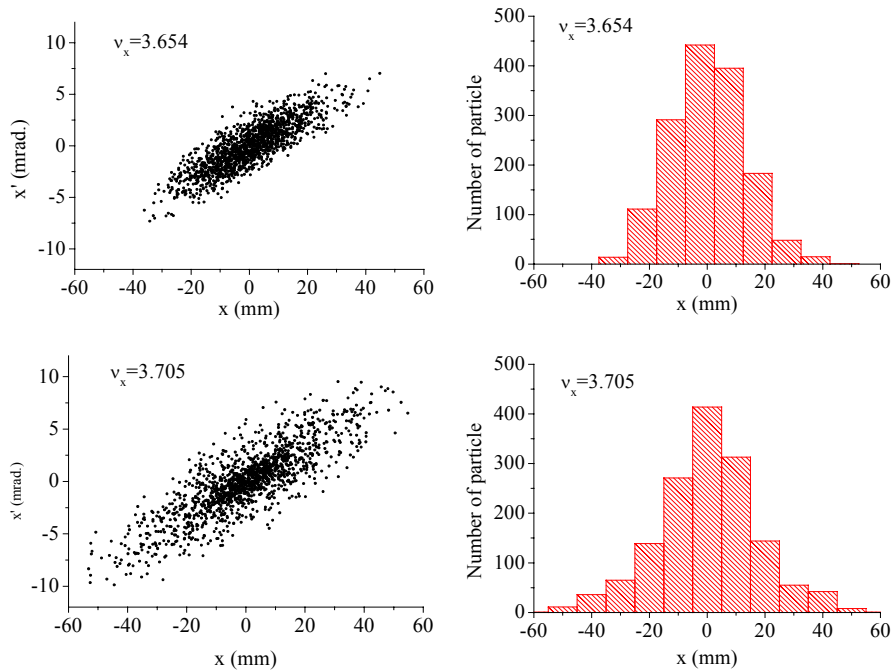
Nonlinear detuning is introduced as a second order effect of sextupole component. It is not straightforward and may create an ambiguity in the detuning strength.

As shown in Fig. 4-10(a), the initial particle distribution seems quite different from Gaussian.

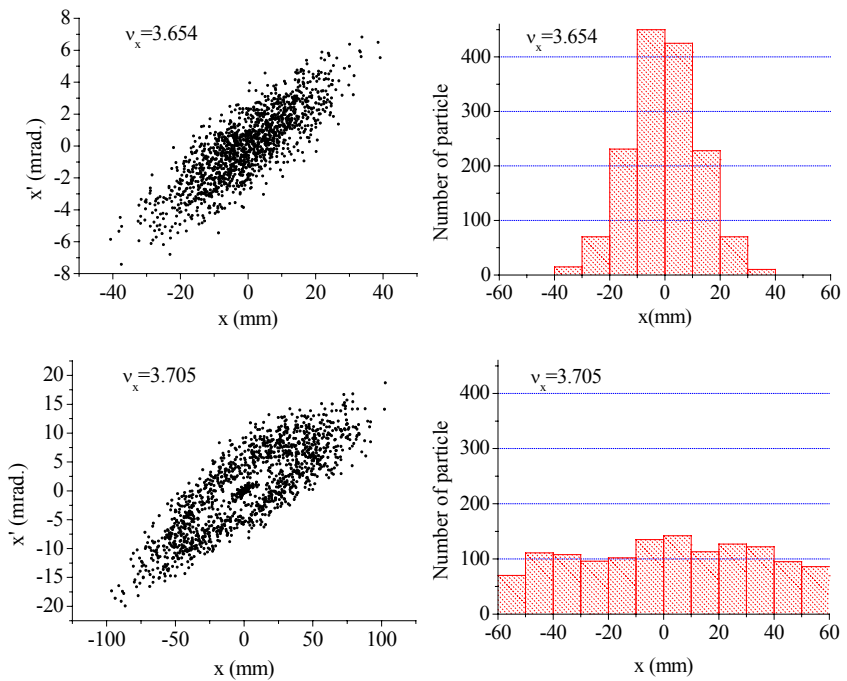
Because of the reasons described above, the beam surviving was unexpectedly small but it is difficult to understand quantitatively. However, obtained beam profiles are quite similar to those of simulation in which the particle distribution in phase space shows “particle trapping”. Therefore we can conclude that “particle trapping” was observed in the direction of tune decreasing.

Figure 4-12 shows simulation results of the particle distributions in phase space and beam profiles during crossing in the direction of tune increasing.

In Fig. 4-12, beam profile changes only slightly due to crossing in this direction. If we assume the five times large driving term, as shown in Fig. 4-13, beam emittance grows much larger. The beam profiles before and after crossing is qualitatively similar to Fig. 4-10(b). We can conclude that emittance growth was observed in the direction of tune increasing. With HIMAC experiment, it becomes evident that the effect of resonance crossing depends on crossing direction when nonlinear detuning is dominant, that is, “particle trapping” in one direction and emittance growth in the reverse direction.



**Figure 4-12. Simulation results of the direction of tune increasing (1).**



**Figure 4-13. Simulation results of the direction of tune increasing (2).**

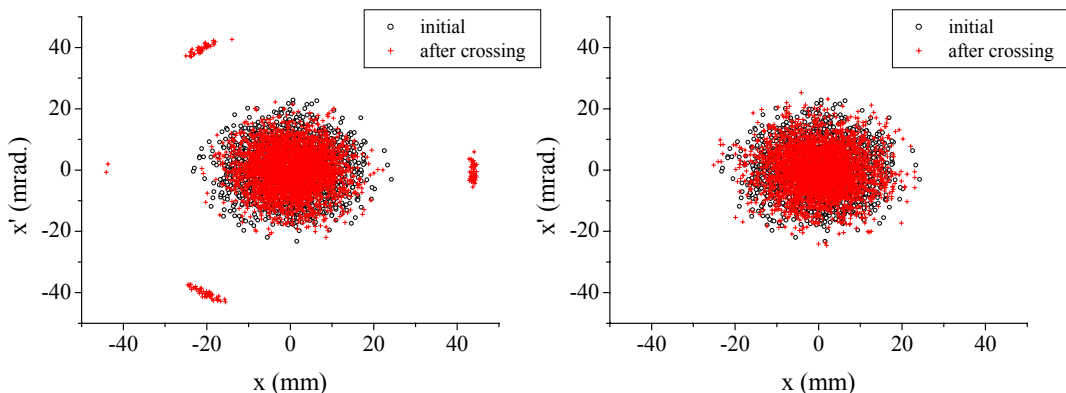
In order to discuss reverse crossing closely, systematic simulation results are shown in the followings.

For simulation, we chose basic parameter listed in Table 4-8.

**Table 4-8. Basic parameters for simulation.**

Crossing Resonance	$3v_x=11$
Crossing Speed	$2.15 \times 10^{-8}$
Nonlinear Detuning ( $\Delta_{NL}$ )	$4.77 \times 10^{-4}$
Excitation Width ( $\Delta_e$ )	$3.58 \times 10^{-6}$
$\kappa$	100
Twiss Parameter at Observation Point	$\alpha=0$ $\beta=1(m)$
Number of Test Particle	3000
Average Emittance	$100\pi$ (mm-mrad.)

The parameters are chosen such that the trapping efficiency with analytical expression become less than 10% when tune crosses in the direction of “particle trapping”. With the parameters, both crossing directions are examined by reversing tune variation. The result is shown in Fig. 4-14.



(a) Crossing in the direction of “particle trapping”      (b) Crossing in the reverse direction

**Figure 4-14. Comparison of crossing direction.**

In (a) and (b), only the direction of tune variation is reversed.

As shown in Fig. 4-14, it appears that the particle distribution before and after crossing in the reverse direction does not change at all whereas some particles are trapped in other direction. This means that reverse crossing is less harmful than “particle trapping” in which trapped particles are brought to large amplitudes and will be lost eventually.

In order to observe clearly the behavior during crossing, the strength of sextupole is increased in a great deal and uniform distribution in  $\alpha^{1/2}$ - $\psi$  space is employed instead of Gaussian distribution. Figure 4-15 shows snapshots of particle distribution during reverse crossing with increased sextupole strength. In Fig. 4-15, crossing speed is slow enough to be adiabatic. We can see the particle distribution during crossing as described in Sec.2.4.2.

If the initial amplitude of each particle is identified as shown in Fig. 4-16, we can see that, after crossing, the initial distribution in amplitude is just shifted in adiabatic crossing.

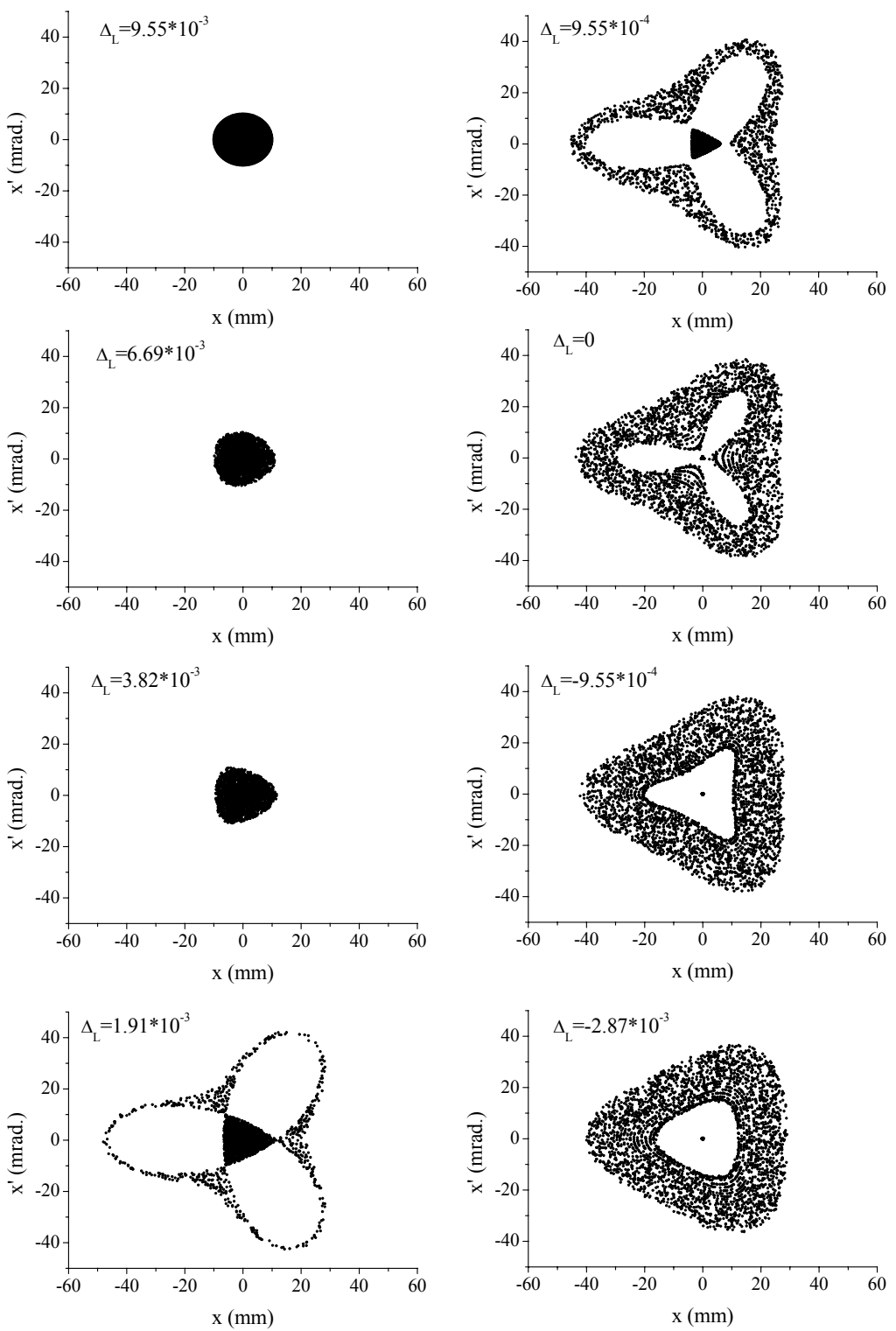


**Figure 4-15. Particle distribution during reverse crossing.**

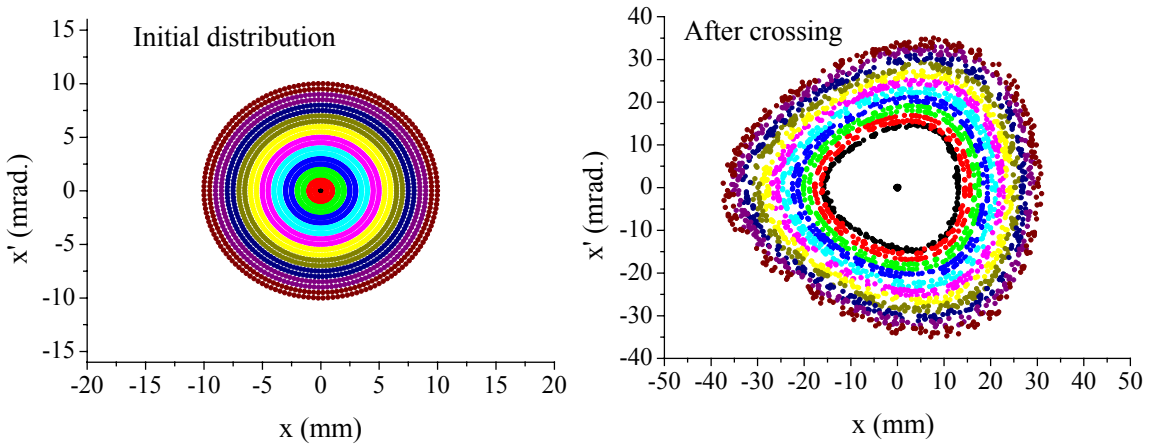


**Figure 4-16.** Particle distribution in amplitude.

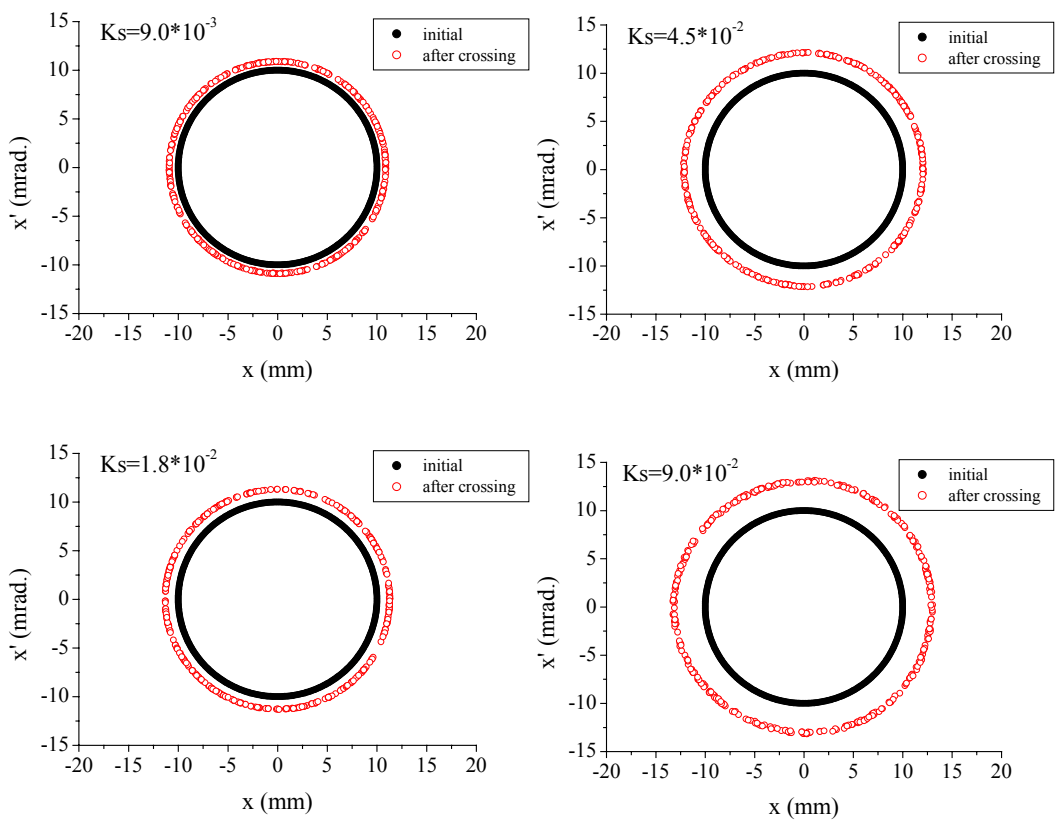


**Figure 4-17.** Reverse crossing for various sextupole strength.

The excitation width in Table 4-8 corresponds to  $K_s = 9.0 \times 10^{-3} \text{ (m}^2\text{)}$ .

We now proceed to verify Eq.( 2-53 ), that is, an analytic expression of the relative emittance growth. Various sextupole strengths are examined with adiabatic crossing speed. Figure 4-17 shows tracking results.

In order to save simulation time, test particles are initially located only at amplitude corresponding to beam emittance of  $100\pi$  mm-mrad. This is justified from the result of Fig. 4-16. In fact, a particle having the maximum amplitude in the initial distribution is also in the maximum amplitude in the distribution after crossing.

In Fig. 4-17, the particle distributions after crossing are transferred beam emittance. It is computed by an average of amplitude defined by linear lattice parameters. They are compared to analytical expression in Fig. 4-18.

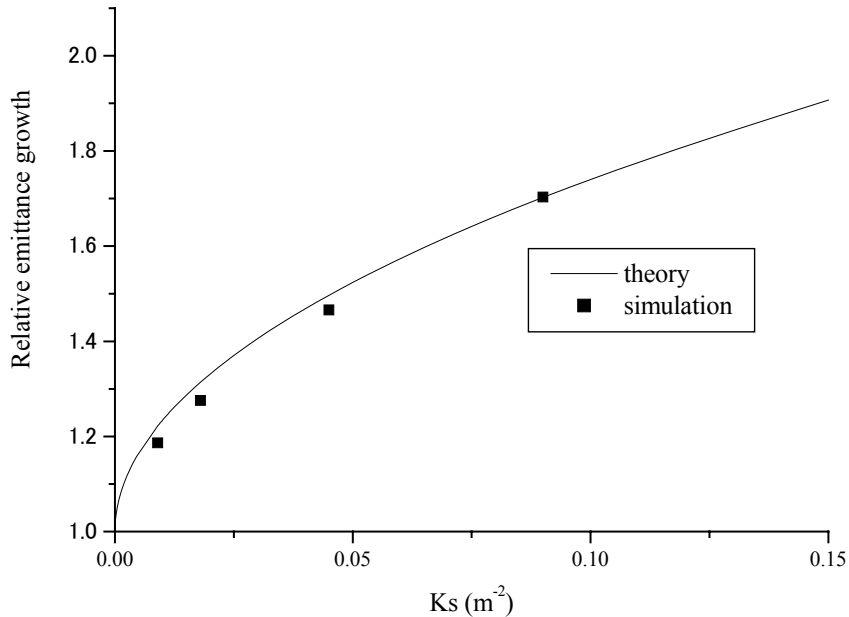


**Figure 4-18. Relative emittance growth.**

In Fig. 4-18, we see a very good agreement between theory and simulation. The analytical expression, Eq.( 2-53 ), is thus verified with the simulation study.

Crossing speed dependence of emittance growth is also examined by simulation. Gaussian distribution is employed again and a root-mean-square (RMS) emittance is evaluated for various crossing speed. Figure 4-19 shows the dependence of relative RMS emittance growth on crossing speed.

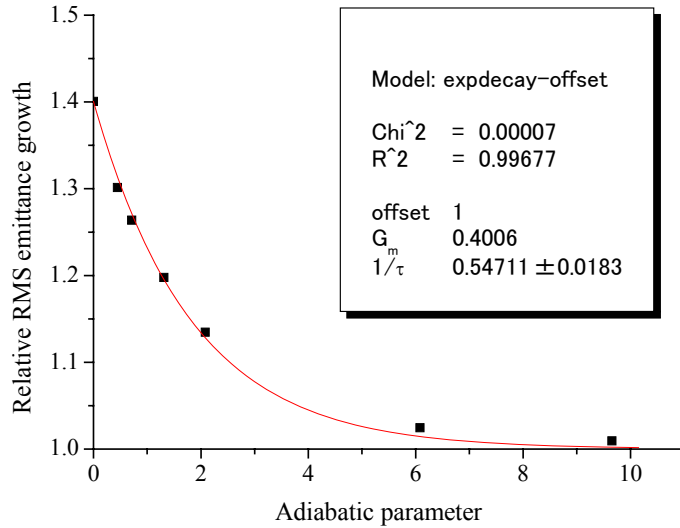


Figure 4-19. Speed dependence of relative RMS emittance growth.

In Fig. 4-19, we find that the relative RMS emittance growth can be expressed as an exponential function of the adiabatic parameter,

$$G_{RMS}(\alpha) = 1 + G_m \exp(-\alpha/\tau), \quad (4-9)$$

where  $\alpha$  is the adiabatic parameter,  $G_m$  is the maximum growth with adiabatic crossing and  $\tau$  is the parameter of exponential decay. In Fig. 4-19, the relative RMS emittance growth is a few percent when adiabatic parameter is 7. Since the growth is proportional to  $\exp(-\alpha)$ , adiabatic parameter more than 7 must be harmless.

### 4.3 Conclusions

Dynamics of “resonance crossing” is studied for FFAG, especially when nonlinear detuning is dominant.

In summary, we have found that:

1. With theoretical works, beam studies and simulations, it has become evident that the damage to beam due to resonance crossing depends upon the direction of crossing.

Crossing in one direction:

“Particle trapping” occurs as was predicted in Ref. [ 18 ]. It was confirmed experimentally in PoP FFAG and HIMAC. These experiments and another study at CERN-PS in Ref. [ 19 ] performed at about the same time are the first experimental observations of “particle trapping”. In PoP FFAG experiment, a third integer resonance crossing was examined. The efficiency of trapping was understood quantitatively. The results were consistent in simulation and experiment. Furthermore, we observed that no particle was trapped when crossing was sufficiently fast. We are convinced that it is possible to cross a resonance, without seriously affecting the beam by “particle trapping”, when adiabatic parameter is more than 7.

Crossing in the reverse direction:

It was evident that an emittance growth occurs in “reverse crossing”. In HIMAC experiment, we observed an emittance growth due to reverse crossing whereas “particle trapping” occurred due to crossing in one direction. On reverse crossing, there has been only a qualitative description by Sturrock. However, the emittance growth is not discussed in a quantitative manner. In this study, we have developed an analytical expression of the relative emittance growth assuming infinitely slow crossing. It is the maximum estimation of possible emittance growth. The dependence of crossing speed is studied and it is found that the relative RMS emittance growth is proportional to the exponential function of adiabatic parameter when initial distribution is Gaussian. The emittance growth is not considerable when adiabatic parameter is more than 7.

2. We have confirmed that the unexpected third integer resonance crossing in 150MeV FFAG is harmless since it is “reverse crossing” and the relative emittance growth is only slightly larger than unity. (Appendix A.4)

## Acknowledgements

I am deeply grateful to Prof. Yoshiharu Mori to be the adviser over the years of my graduate student days. He gave me not only the chance to study the field of accelerator but also a lot of advices throughout this work and many other valuable things to my research activities.

I am also very grateful to Dr. Shinji Machida. He provided me with his wide knowledge of beam dynamics. I often bothered him with trivial questions but he always answered kindly.

I would like to thank Dr. Shoroku Ohnuma for the guidance throughout this work. He gave me many useful comments and corrected this thesis patiently.

Also, I wish to express my appreciation to Drs. Masahiro Yoshimoto, Yuujiro Yonemura and Akira Takagi. From them, I have gained much knowledge and learnt a variety of techniques. It has always been a pleasure for me to work with them.

I should like to express my sincere gratitude to Drs. Takeichiro Yokoi, Kiyomi Koba, Chihiro Ohmori, Masahito Yoshii, Izumi Sakai, Kiyoshi Ikegami, Chikashi Kubota, Ryousaku Muramatsu, Miho Fujieda, Masanobu Yamamoto, Akiyoshi Yamazaki, Joe Nakano, Yasuo Sato, Yoshimasa Yuasa, Atsutoshi Mutoh, Masahiro Sugaya, Eiichi Yanaoka and Ryuichi Ueno. It was productive days for me to construct PoP-FFAG and 150MeV FFAG with them. I believe that the commissioning of FFAG was an exciting experience for us all.

I would like to thank Drs. Tomonori Uesugi and Yoshinori Hashimoto. They worked with me on many all-night machine shifts of HIMAC. I thank Dr. Koji Noda who gave me the chance to carry out the beam study at HIMAC and I also thank members of the Accelerator Engineering Corporation who supplied us with beams in response to our requests.

I also thank Francois Meot who helped me with PoP beam studies during his stay at KEK.

Last but not least, the support and encouragement given to me by Ms Kimiyo Ikeda, our group secretary, is greatly appreciated.

## Bibliography

- [ 1 ] T. Ohkawa, Symposium on Nuclear Physics of the Physics Society of Japan, private communication (1953).
- [ 2 ] E. D. Courant et al., "The Strong-Focusing Synchrotron-A New High Energy Accelerator", Phys. Rev., Vol.88, No.5, p1190 (1952).
- [ 3 ] E. D. Courant et al., "Theory of the Alternating-Gradient Synchrotron", Ann. Phys., Vol.3, p1 (1958).
- [ 4 ] F. T. Cole et al., "Electron Model Fixed Field Alternating Gradient Accelerator", Rev. Sci. Instrum., Vol.28, No.6, p403 (1957).
- [ 5 ] K. R. Symon et al., "Fixed-Field Alternating-Gradient Particle Accelerators", Phys. Rev., Vol.103, No.6, p1837 (1956).
- [ 6 ] T. Sakai, informal meeting material, private communication
- [ 7 ] Y. Mori et al., "A NEW TYPE OF RF CAVITY FOR HIGH INTENSITY PROTON SYNCHROTORON USING HIGH PERMEABILITY MAGNETIC ALLOY", Proc. of EPAC'98, p299 (1998).
- [ 8 ] M. Aiba et al., "DEVELOPEMENT OF A FFAG PROTON SYNCHROTRON", Proc. of EPAC'00, p581, (2000).
- [ 9 ] Y. Yonemura et al., "COMMISIONING OF 150MeV FFAG SYNCHROTRON", Proc. of EPAC'04, p2673 (2004)
- [ 10 ] M. Tanigaki et al., "CONSTRUCTION OF FFAG ACCELERATOR IN KURRI FOR ADS STUDY", Proc. of EPAC'04, p2673 (2004).
- [ 11 ] A. Sato et al., "FFAG AS PHASE ROTATOR FOR THE PRISM PROJECT", Proc. of EPAC'04, p713 (2004)
- [ 12 ] J. S. Berg et al., "FFAGS FOR MUON ACCELERATION", Proc. of PAC'03, p3413 (2003).
- [ 13 ] R. Baartman et al., "AMPLITUDE GROWTH FROM THE RAPID TRAVERSAL OF A HALF-INTEGER RESONANCE", Proc. of Cyclotron Conference'84, p40 (1984).
- [ 14 ] W. P. Lysenko, "NONLINEAR BETATRON OSCILLATION", Part. Accel., Vol.5, p1 (1973).
- [ 15 ] P. A. Sturrock, "NONLINEAR EFFECT IN SYNCHROTRONS", Ann. Phys., Vol.3, p113 (1958).
- [ 16 ] G. Guignard, "THE GENARAL THEORY OF ALL SUM AND DIFFERENCE RESONANCES IN A THREE-DIMENSIONAL MAGNETIC FIELD IN A SYNCHROTRON ", CERN-76-06 (1976).

- [ 17 ] S. Machida, Proc. of NuFact'04 (to be published)
- [ 18 ] A.W. Chao et al., “PARTICLE TRAPPING DURING PASSAGE THORUGH A HIGH-ORDER NONLINEAR RESONANCE”, Nucl. Instrum. Meth., Vol.121, p129 (1974).
- [ 19 ] M. Giovannozzi et al., “MULTITURN EXTRACTION BASED ON TRAPPING IN STABLE ISLANDS AT CERN PS: RECENT MEASUREMENT ADVANCES”, Proc. of EPAC'04, p173 (2004)
- [ 20 ] S. Y. Lee, “Accelerator Physics”, World Scientific Publishing (1999).
- [ 21 ] H. Wiedemann, “Particle Accelerator Physics”, Springer (1993).
- [ 22 ] M. Yoshimoto, “Study of Beam Dynamics in Fixed Field Alternating Gradient Accelerator”, Ph. D Thesis submitted to Graduate School of Engineering, Doshisha University (in Japanese) (2003).
- [ 23 ] K. Koba, “Two-Bunch Acceleration in FFAG”, presentation at FFAG workshop, KEK, Japan, Aug. 2000, private communication
- [ 24 ] Y. Yonemura, “Study of Beam Extraction from FFAG accelerator with ‘Mass-less Septum’ ”, Master Thesis submitted to Graduate School of Engineering, Kyushu University (in Japanese) (2001).
- [ 25 ] T. Uesugi, “Beam Acceleration with Fixed Frequency RF Bucket”, presentation at FFAG workshop, LBL, USA, Nov. 2002, private communication
- [ 26 ] S. Machida, “Radial Sector FFAG with Triplet Lattice”, Proc. of the Workshop of High Intensity Secondary Beam with Phase Rotation, p36 (in Japanese) (1999).
- [ 27 ] Y. Hirao et al., “Heavy Ion Medical Accelerator in Chiba — A Design Summary and Upgrade —”, NIRS-M-89 HIMAC-001 (1992).
- [ 28 ] Y. Hashimoto, “Oxygen gas-sheet beam profile monitor for the synchrotron and storage ring”, Nucl. Instrum. Meth. In Phys. Research A527, p289 (2004).
- [ 29 ] R. D. Rush, “SINGLE-PARTICLE DYNAMICS IN CIRCULAR ACCELERATOR”, AIP 153, p152
- [ 30 ] W. H. Press et al., “Numerical recipes in FORTRAN 2nd ed.”, Cambridge university press (1992).
- [ 31 ] L. H. Toburen et al., “Measurement of High-Energy Charge-Transfer Cross Sections for Incident Protons and Atomic Hydrogen in Various Gases”, Phys. Rev., Vol.171, No.1, p114 (1968).
- [ 32 ] See “T-2 Nuclear Information Service”, <http://t2.lanl.gov/data/>
- [ 33 ] R. Bartolini et al., “TUNE EVALUATION IN SIMULATIONS AND EXPERIMENTS”, CERN SL/95-84(AP) (1995).

## **Appendix**

### **A Overview of 150MeV FFAG synchrotron**

The FFAG currently in its commissioning stage is a prototype proton accelerator of scaling type to investigate possibilities for various applications such as high power proton drivers, proton therapy and accelerator driven sub-critical reactors. The design final energy is 150 MeV with D-F-D triplet lattice. One unique feature of the machine is a new type of magnet, which may be called “yoke-free magnet”. During commissioning, it was found out that resonance crossing of  $3v_x=11$  occurs unexpectedly. However, it has become evident from our studies on resonance crossing that this is not at all critical. In this appendix, we will present the general features of the 150MeV FFAG and discuss its resonance crossing.

#### **A.1 Design**

##### **A.1.1 Basic Parameters**

Machine parameters of 150MeV FFAG are listed in Table A-1. One of our goals is to achieve a rapid cycle of more than 250Hz to generate high beam current. Energy range of 10 to 125MeV will be tried first with a lower magnetic field and this will be followed by 150MeV mode.

##### **A.1.2 Yoke-free magnet**

In radial sector type FFAG, a direction of focusing magnet field is opposite to that of defocusing magnet field so as to realize alternating gradient focusing. Therefore a normal bending magnet and reversed field magnets on both sides, that is triplet D-F-D, can be combined together without any return-yoke. Figure A-1 shows the magnetic circuit representing the concept of yoke-free magnet.

**Table A-1. Machine parameters of 150MeV FFAG.**

Type of magnet	Triplet Radial (DFD)
Number of sector	12
k-value	7.6
Energy (MeV)	12→150 (10→125)
Average radius(m)	4.47→5.20
Betatron tune	Hor.: 3.69~3.80 Ver.: 1.14~1.30
Maximum field (T) (on orbit)	F: 1.63 D: 0.78
Repetition (Hz)	250

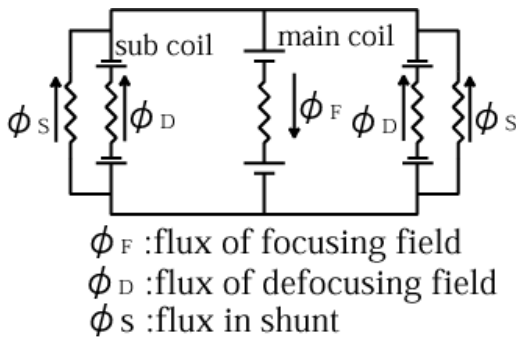


**Figure A-1. Magnetic circuit of “yoke free magnet”.**

The magnetic flux excited mainly by the coils attached to the poles of focusing magnet makes a loop that goes through the gap of focusing magnet and returns through the gap of defocusing magnet. Total flux of the normal bend must be larger than that of reversed bend so that orbits can close. In order to realize this, there are four “shunt yokes” at the corner of the magnet not only to adjust the magnetic flux but to support upper and lower poles as well. The small coils attached to defocusing magnet play the role of a knob for fine tunings of the field. This new type of FFAG magnet is called “yoke-free magnet”. The yoke-free magnet makes it possible to inject a beam into or extract even from a magnet region. Another practical side benefit is the weight reduction because of no solid block of return yoke.

### A.1.3 Linear model

Basic parameters such as cell number and k-value are determined with a linearized model. The model is made up with combined function magnets including edge focusing and evaluates linear focusing force. Figure A-2 shows the geometry of linearized model for D-F-D triplet lattice. In the model, a closed orbit has a constant curvature in each magnet and the magnetic field contains bending and quadrupole components only. This model has been found to give an approximate but reliable value of the transverse tune.

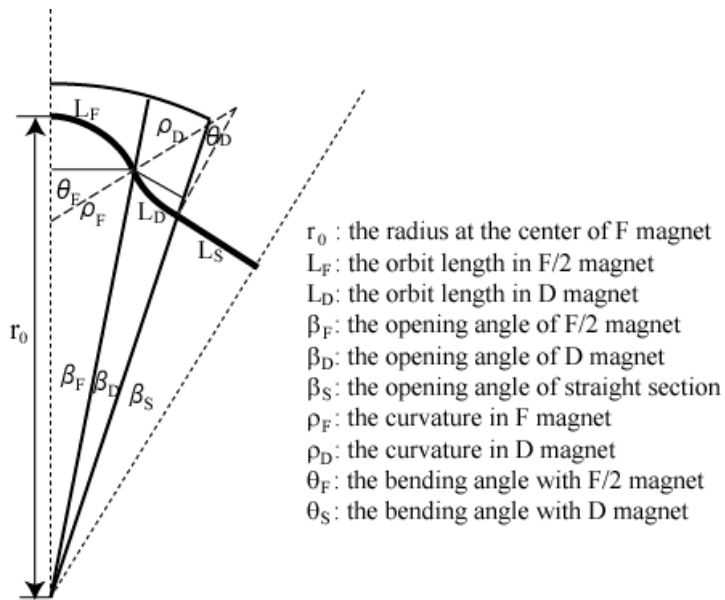


**Figure A-2. Linearized model for triplet D-F-D (half cell).**

### A.1.4 3-dimentional field calculation

Based on basic parameters obtained with linearized model, FFAG magnet was designed using three-dimensional field calculation code TOSCA, which is a reliable code widely used in the accelerator field. The structure of magnet is yoke-free and the large gradient of magnetic field is realized by pole shaping.

In principle, betatron tunes are constant in a scaled type of FFAG. However, because of fringe field and field saturation, it is difficult to make the field that satisfies the zero chromaticity condition. A goal of the design is to reduce the variation of betatron tunes as much as possible.

Basic strategy of magnet design is to maintain the same k-value in focusing and

defocusing magnets including fringe field. Magnet pole shapes are initially determined by the  $k$ -th power of radius. To balance the influence of fringe field, the pole shape is modified as follows. By integrating the field, including the fringe field, on median plane along a constant radius,  $k$ -values are estimated in focusing and defocusing magnets separately. The integrated values are adjusted such that they are proportional to the  $(k+1)$ -th power of machine radius. For pole shapes at inner side, tangential line is adopted for the inner side to prevent the gap from becoming too large with the index function. For outer side, additional piece analogous to Logowsky's cut is attached to the end of focusing pole to relieve field saturation. Since field saturation cannot be avoided completely with this method, the outside gap of defocusing magnet is slightly widened to balance the residual field saturation of focusing pole. Figure A-3 shows a plan of the designed magnets and the equations of pole shape. Figure A-4 shows calculated betatron tune with designed magnets.

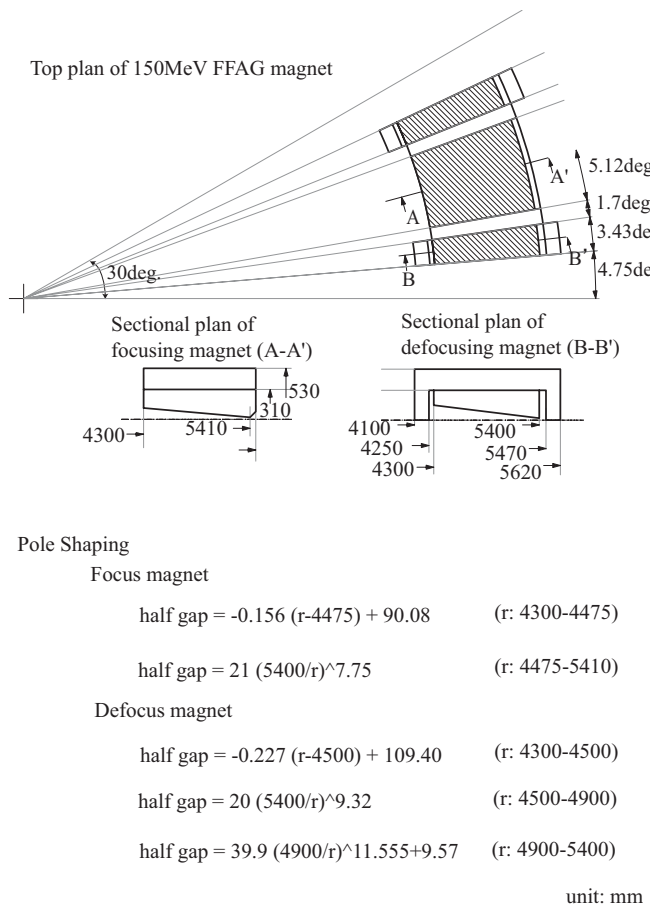


**Figure A-3 Drawing of 150MeV FFAG Magnet.**

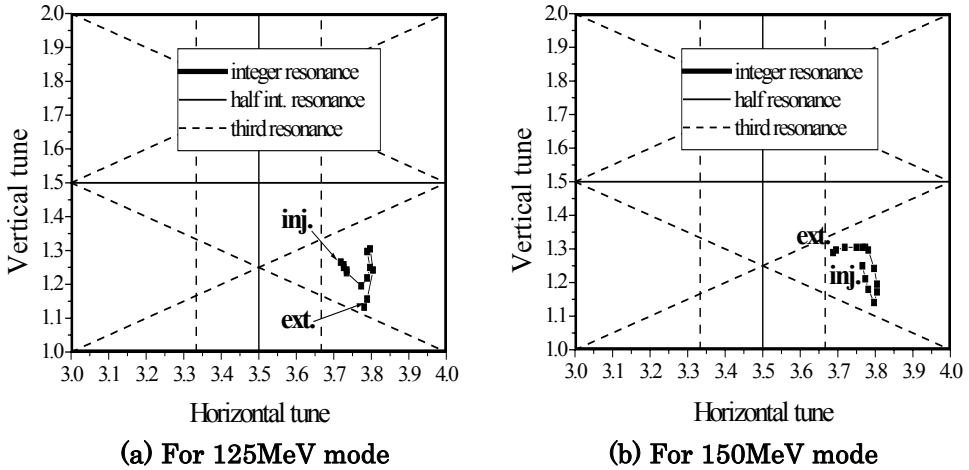


**Figure A-4. Betatron tunes.**

The resonances up to third order excited by normal components of magnetic field are avoided.

### A.1.5 Injector cyclotron

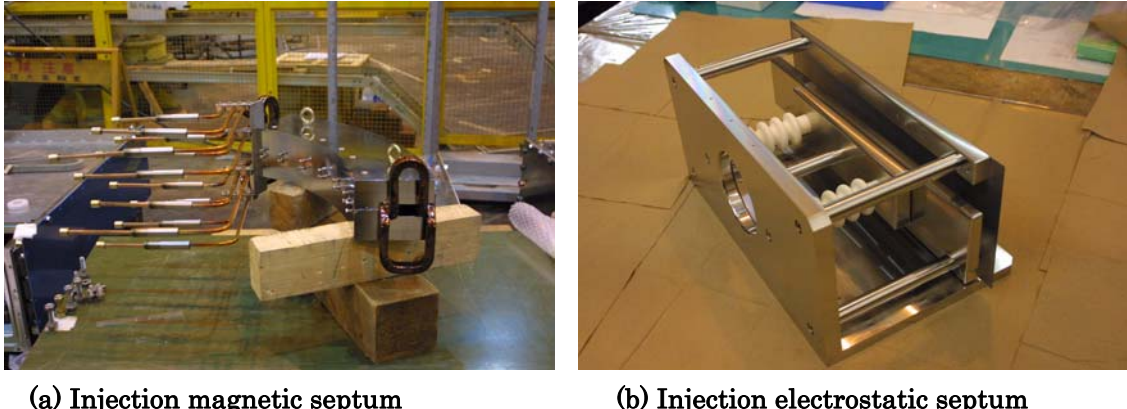
Injector cyclotron is used for a proton beam of 10 or 12MeV. The cyclotron has a small diameter of 1.4m. The compactness is suitable for placing it inside of the FFAG ring. As a result, the injection line has no bending magnet. In order to match the time structure of FFAG operation, the cyclotron is in pulsed mode corresponding to the repetition rate of FFAG. The beam pulse length is approximately 100  $\mu$ s.

### A.1.6 Injection and extraction

The injection system consists of a septum magnet, an electrostatic septum, and a pair of bump magnets. Proton beam from the injector cyclotron is inflected by the magnetic septum and lead to the electrostatic septum. Injection septa are shown in Fig. A-5.

Fast extraction is done with a kicker and an extraction magnetic septum. Beam is extracted from a region of focusing magnet, taking advantage of yoke-free design. This considerably relieves the requirement for extraction devices. Figure A-7 shows the design extraction orbit.

Figure A-6 shows a closed orbit with the bump section and injection hardwares.



(a) Injection magnetic septum

(b) Injection electrostatic septum

Figure A-5. Injection septa.

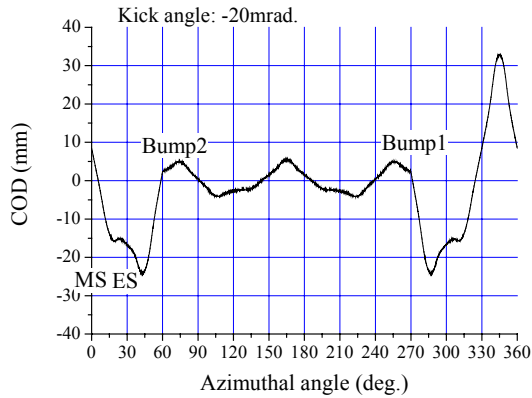


Figure A-6. Injection bumped orbit.

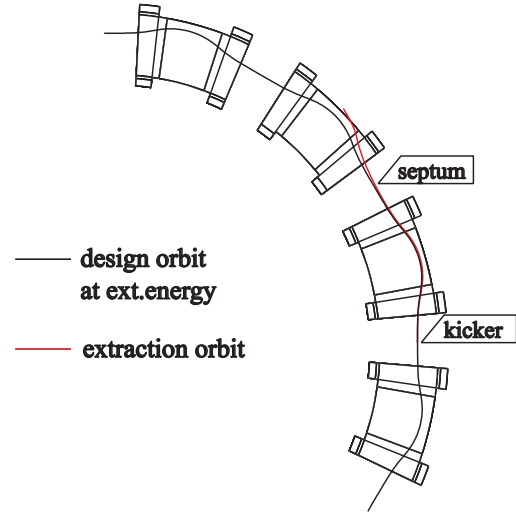


Figure A-7. Extraction orbit.

Figure A-8 shows the power supply for kicker magnet. It employs an array of IGBT and can generate a pulse current with rise time of 130ns. The maximum voltage and current is 70kV and 2000A, respectively. The kicker power supply has been specially developed for the rapid cycling of 250Hz.



**Figure A-8. Power supply for extraction kicker.**

#### A.1.7      rf cavity

Table A-2 lists the specification of rf system and Fig. A-9 shows rf cavity and main rf amplifier. The cavity has two MA cores separated by 30mm. The water-cooled metal plates are adopted on one side of cores sandwiching a thermal conductive sheet.

**Table A-2. Specification of RF system.**

RF frequency	1.5 ~ 4.5 MHz
Acceleration voltage	10 kVpp
RF output power	55 kW
Class	B class, Push-pull
Power tube	4CW25000A x 2
Core material	FINEMET (FT-3M)
Number of core	2
Outer size	1700x950mm
Inner size	980x230mm
Aperture of metal frame	940x190mm
Core thickness	25mm

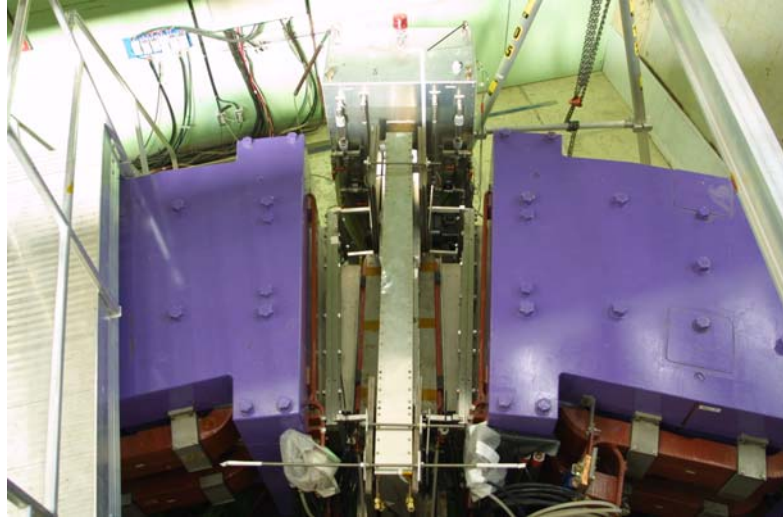


**Figure A-9. RF cavity and main amplifier.**

## A.2 Construction

### A.2.1 Field measurement

Magnetic field measurement was carried out to confirm that expected field can be obtained in magnets and that the magnet-to-magnet fluctuation of the field is within the allowed range. Three hole-probes were mounted with probe heads perpendicular to each other so as to measure three field components. A three-dimensional moving table was used to move probe heads, and a field map covering injection to extraction was obtained.

Before taking data, the optimum combination of coil currents in focusing and defocusing magnets was searched. We found that a slightly lower current in focusing magnet was optimum while some 30% more current was needed in defocusing magnet in order to realize the design field intensity. Since the field intensity in defocusing magnet is sensitive to field saturation (magnetic resistance) in shunt yoke, the difference of coil current is believed to be caused by an overestimate of field saturation. A 30% difference seems large. However it may be reasonable if one notes that the turn number of coil for focusing magnet is larger by one digit than that of defocusing magnet. Mapping data was acquired with the combination of coil currents found from searching and this was compared with the calculated field. A good agreement can be seen in Fig. A-10 except for a small difference in fringe field around injection orbit. This may be

due to the larger defocusing coil current.

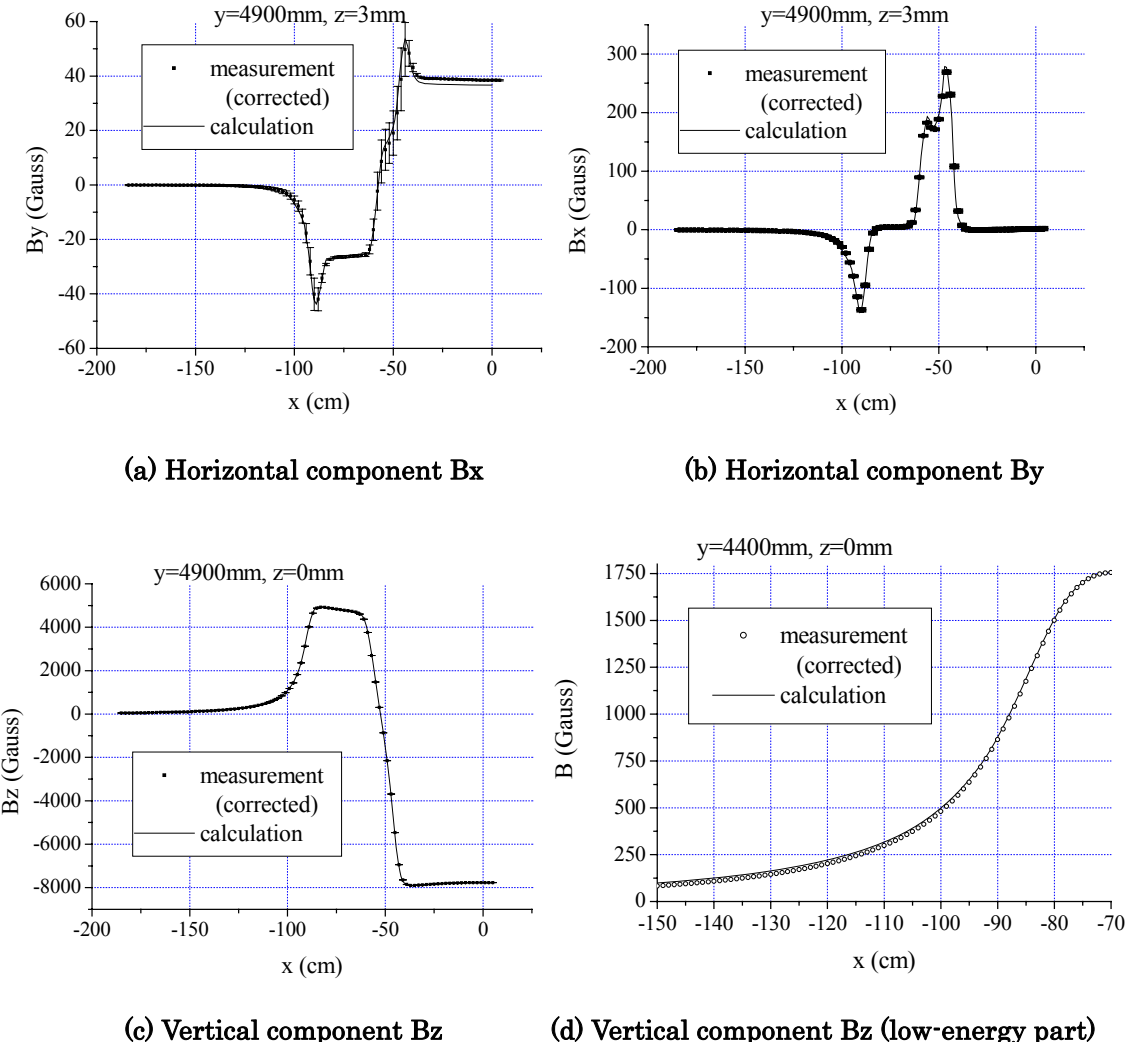


**Figure A-10. Result of field measurement (1).**

All three components show an excellent agreement between measurement and calculation although the low-energy part has a small difference. In (d), the picture of fringe field is enlarged and measurement error is less than plot point. Coordinate is such that the origin is machine center and  $y$ -axis is the radial line of focusing magnet center.

Figure A-11 shows the difference between arbitrary two randomly selected magnets. Relative error diverges at a point where vertical component  $B_z$  crosses zero. However, the difference in main body is at most 0.1 %. Systematic alignment error of

measurement is approximately 0.03%. Therefore, the relative error may be of the order of  $10^{-4}$ . It is small enough to make a shuffling of magnets unnecessary.

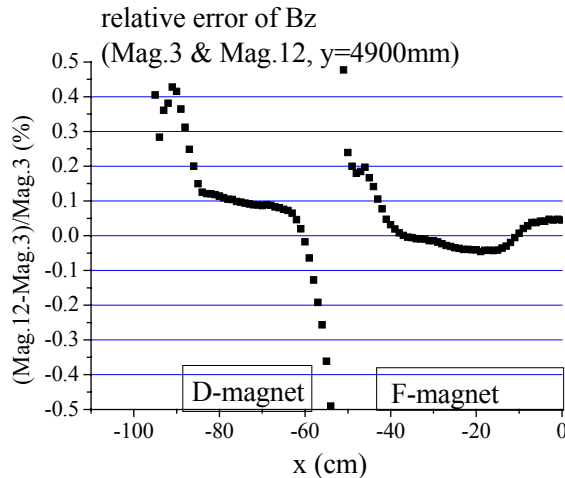


Figure A-11. Result of measurement (2).

### A.2.2 Alignment

Alignment of FFAG magnets was performed with two theodolites and a high precision ruler. The ruler has the accuracy of 0.1mm and is made of metal having a negligibly small thermal expansion coefficient. The injector cyclotron was set first as the baseline of alignment. A dodecagon with 1.9m arms was marked using theodolite and the ruler with an accuracy of less than 0.1mm. Based on the dodecagon, twelve magnets were aligned with an accuracy of less than 0.2mm. The median plane of FFAG ring was adjusted to that of injector cyclotron. Figure A-12 schematically shows how the alignment was done.

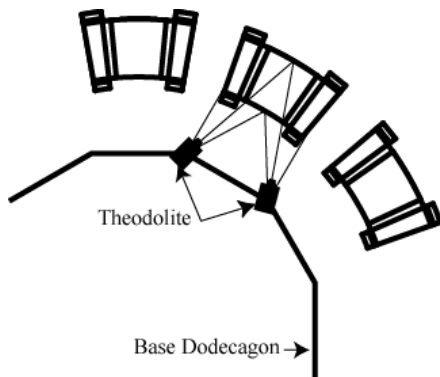


Figure A-12. Alignment of FFAG magnet.

All devices, except for extraction hardwares were assembled in March 2002. Figure A-13 is a picture of the constructed machine and Fig. A-14 is a top plan of the machine.

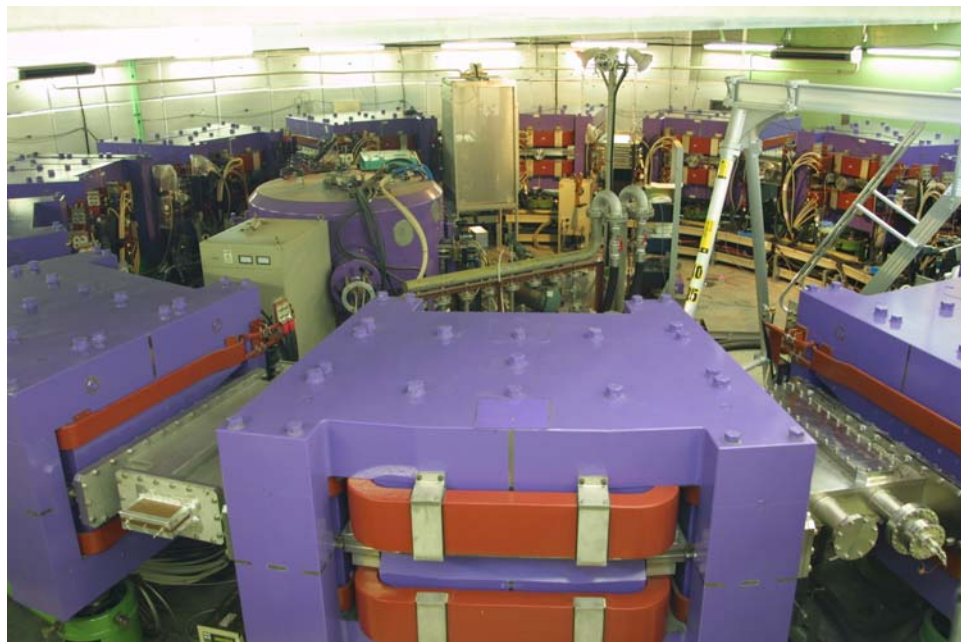


Figure A-13. Picture of the constructed machine.

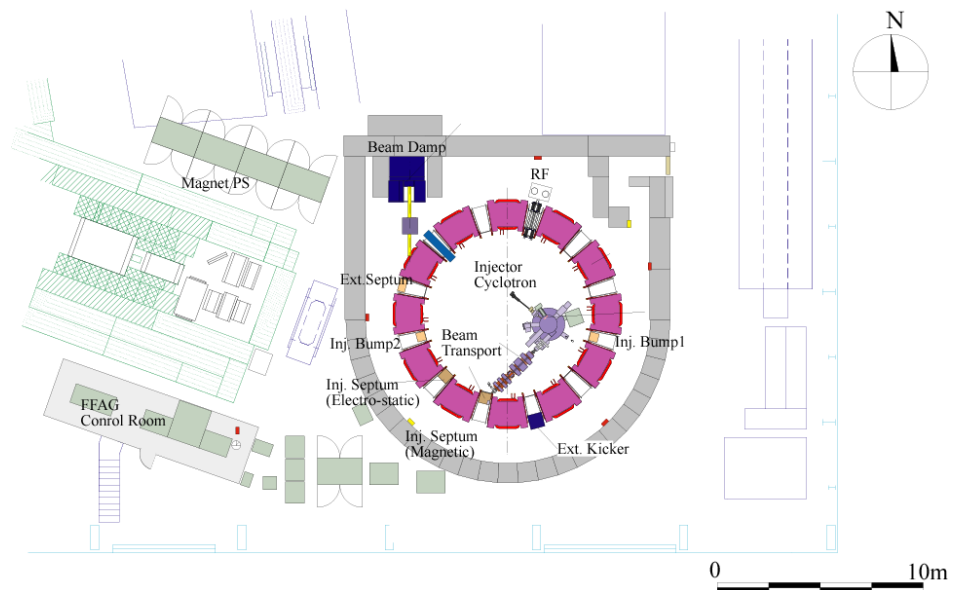


Figure A-14. Top plan of the machine.

## A.3 Commissioning

### A.3.1 Beam injection

For injection tuning, two moving thin plates are installed outside of two septa in order to observe beam positions. They are destructive beam monitors for a direct detection of beam current. When bump magnets are not excited, the horizontal acceptance of the machine is large enough for multi-turn injection of  $\sim 10$  revolutions. Turn-by-turn positions can be observed clearly until beam hits the septum. Figure A-15 shows the measured beam position of the first successful injection. Measured beam positions can be transferred to beam locations in phase space. Injected beam must be parallel to the design orbit with a separation corresponding to the bump orbit at the septum. In Fig. A-15, it is seen that injected beam was close to the ideal position. After tuning was finished, bump magnets are excited to pull in closed orbit from inside of septum.

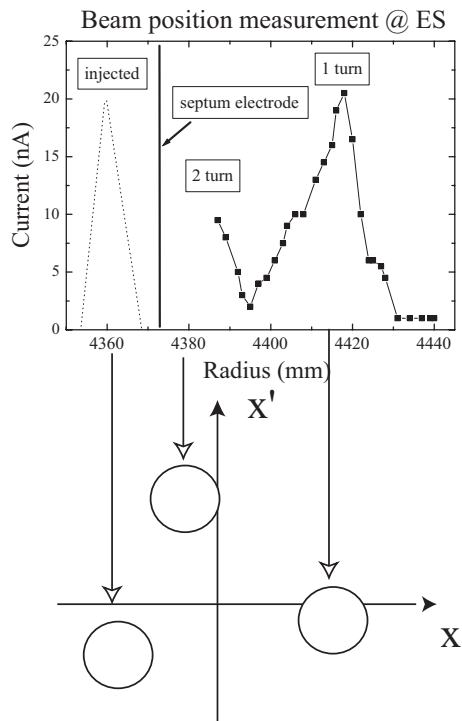


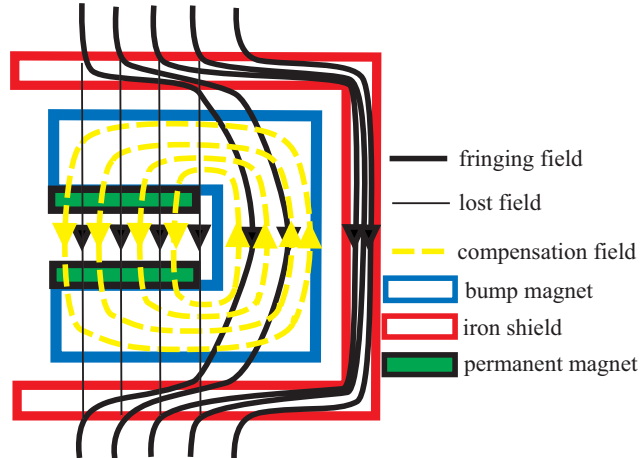
Figure A-15. Beam position in first succeed of injection.

### A.3.2 COD sources and compensation

The large gap for gradient magnetic field is responsible for a few hundred Gauss of fringe field in straight section. Any magnetic materials installed in straight section interfere with the fringe field and affect beam orbit. Injection bump magnets and the

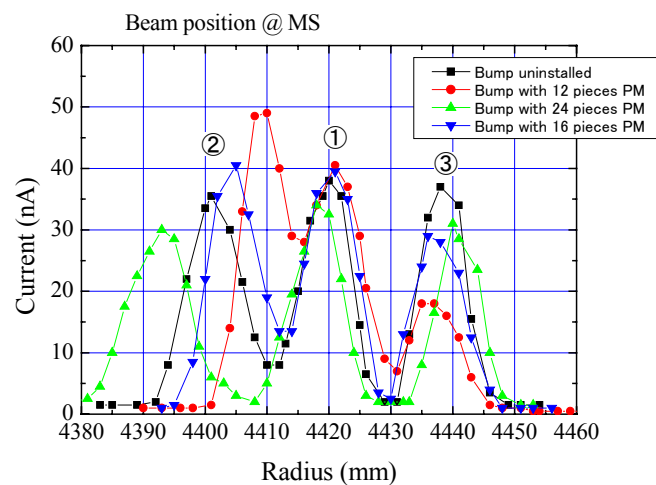
core of rf cavity are the known sources of COD. The magnetic septum seems to be negligible as a source of COD since it does not cover beam orbit. The COD due to bump magnets and rf cavity are compensated for, respectively, with permanent magnet and extra bending magnets.

Figure A-16 is a schematic view of the bump magnet with permanent magnet to compensate static dipole field. Strength of the dipole was adjusted iteratively by varying number of attached piece (5\*40\*60mm) of permanent magnetic material. Fig.A-16 illustrates beam positions with and without bump magnets.



**Figure A-16. Schematic view of bump magnet.**

Dipole field of the permanent magnet compensates lost field. Iron shield is added to avoid saturation in the return yoke of bump magnet.



**Figure A-17. COD source compensation (Bump).**

A set of dipole magnets were installed near rf cavity and their excitation strengths were adjusted by the observed beam positions. Figure A-18 shows observed beam position for various dipole fields.

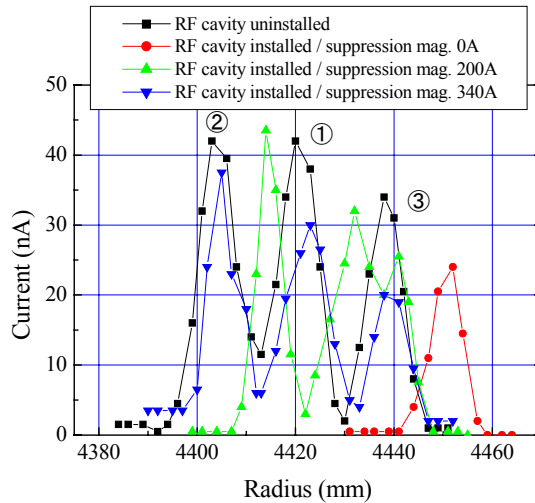


**Figure A-18. COD source compensation (rf cavity).**

### A.3.3 Betatron tune measurement

Betatron tunes at injection energy were measured for various defocusing coil currents, that is, for different FD ratios. With varying FD ratios, mostly the vertical tune can be controlled. Figure A-19 shows the result of tune measurement.

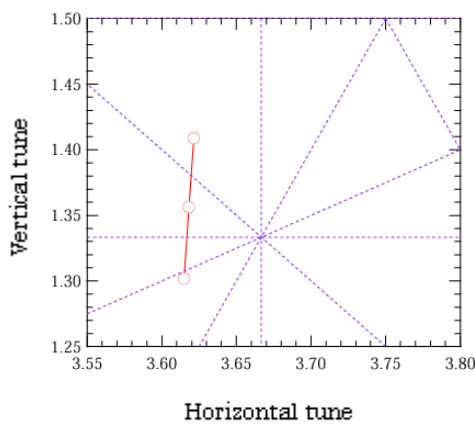


**Figure A-19. Tune measurement.**

Betatron tune was measured by varying coil current of defocusing magnet with 100A steps.

The slope of measured vertical tune is 0.11 per defocusing magnet coil current of 200A. This agrees with calculation. The slope of horizontal tune is also as expected. However, while the design value of horizontal tune at injection is 3.72, the measured value is 3.62. Following reasons might cause this difference. One is that the magnet design was based on stand-alone magnet. In reality, twelve magnets are assembled to make a ring and there should be magnetic interaction among them. The other is that coil current of defocusing magnet is increased by 30% or so compared with the design value.

#### A.3.4 Beam acceleration

Figure A-20 shows bunch monitor signal for adiabatic capture and acceleration. Adiabatic capture and beam acceleration was successfully achieved as shown. Even though the horizontal tune crossed third integer resonance of  $3v_x=11$ , no beam loss was observed with the bunch monitor.

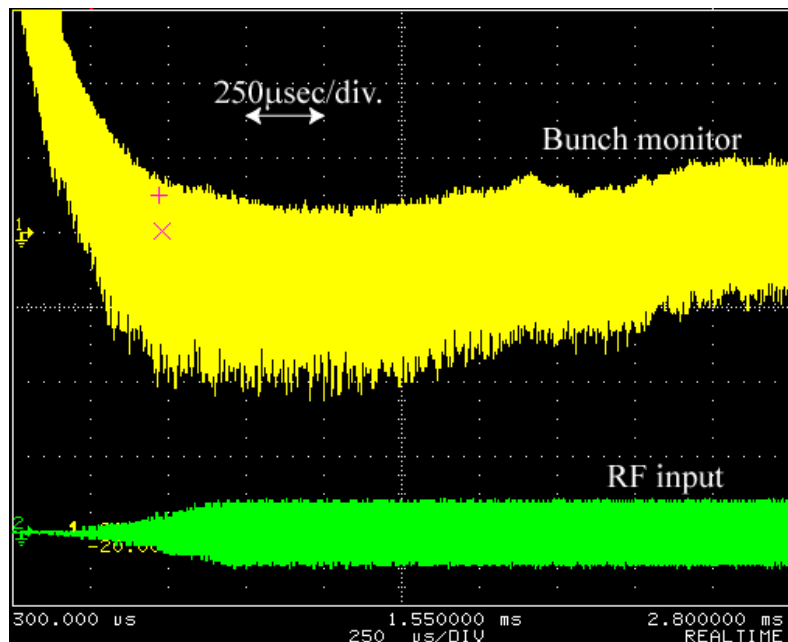


**Figure A-20. Beam acceleration.**

There is adiabatic capture process of 1ms in which rf voltage is increasing gradually. After that, beam is accelerated.

### A.3 Resonance crossing

The measured horizontal tune at injection was found to be lower than the design value. The unexpected discrepancy is only a few percent but the horizontal tune crosses third integer resonance  $3\nu_x=11$  when beam is accelerated a few MeV.

As shown in Fig. A-21, the crossing of resonances up to the third order excited by normal components of magnetic field is avoided in the design. Crossing of  $3\nu_x=11$  will be a serious issue if the beam quality is affected by it. However, in an acceleration study, practically no effects on the beam were observed with a bunch monitor.

The sign of zero-th harmonics of octupole component determines whether nonlinear detuning is positive or negative. Octupole component in focusing magnet is dominant and it results in positive nonlinear detuning. Since horizontal tune is less than  $3\nu_x=12$  (third order structure resonance), the second order effect of sextupole also results in positive nonlinear detuning. On the other hands, tune increases and crosses  $3\nu_x=11$ . Therefore the direction of crossing  $3\nu_x=11$  is the reverse direction. In “reverse crossing”, there is no beam loss due to particle trapping. A possible effect of reverse crossing is not a beam loss but just an emittance growth depending on the strength of driving term. Figure A-21 shows simulation result of crossing  $3\nu_x=11$ . After crossing, there seems no adverse effect as the driving term is too small for an emittance growth.

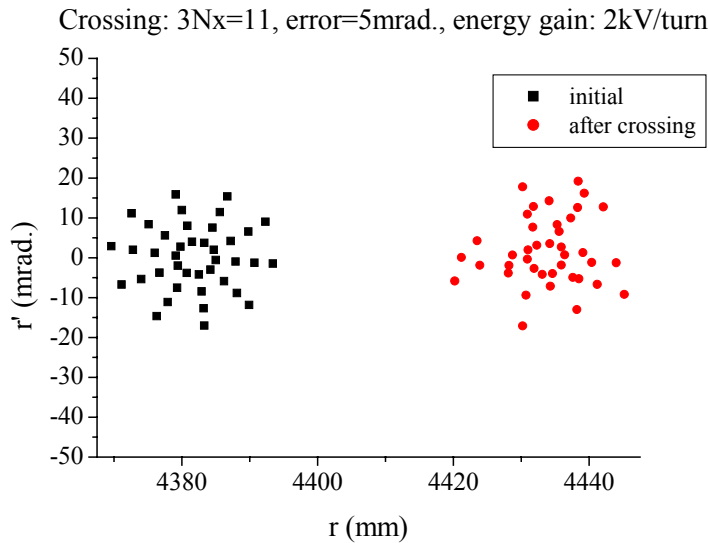


**Figure A-21. Simulation result of crossing  $3\nu_x=11$ .**

## B Particle tracking in three-dimensional magnetic field

For a design of magnet and simulation study of FFAG, particle tracking in three-dimensional field is employed. Three-dimensional magnetic field is generated by a calculation code such as TOSCA. Field map is extracted from calculated field as a table containing three-dimensional positions and field data. Field of a point where particle passes in each calculation step is obtained by a linear interpolation. A particle is simply traced by a numerical integration with fourth order Runge-Kutta method [ 30 ].

Equations of motion of a charged particle in magnetic field are,

$$\frac{d\vec{Q}}{dt} = \vec{v}, \quad (\text{B-1})$$

$$m \frac{d\vec{v}}{dt} = q\vec{v} \times \vec{B}, \quad (\text{B-2})$$

where  $\vec{Q}$  is the position vector,  $\vec{v}$  is the velocity vector,  $\vec{B}$  is the magnetic field,  $m$  is the relativistic mass,  $q$  is the charge of particle and  $t$  is time, which is the independent variable.

When the step size of the time independent variable is fixed, the number of integration steps for one revolution is varied in different momentum particles. Therefore it is convenient to change independent variable from time  $t$  to azimuthal angle  $\theta$ , so cylindrical coordinate is adopted here. It may be the optimum coordinate for a calculation in scaling FFAG accelerator. If we take the step of independent variable  $d\theta$  as  $2\pi$  divided by integer number, azimuthal periodic condition is preserved precisely.

We have six variables ( $r, \theta, z, v_r, v_\theta, v_z$ ). Equations ( B-1 ) and ( B-2 ) can be written with these variables,

$$\frac{dr}{dt} = v_r, \quad (\text{B-3})$$

$$\frac{d\theta}{dt} = \frac{v_\theta}{r}, \quad (\text{B-4})$$

$$\frac{dz}{dt} = v_z, \quad (\text{B-5})$$

$$m \frac{dv_r}{dt} = q(v_\theta B_z - v_z B_\theta) + \frac{mv_\theta^2}{r}, \quad (\text{B-6})$$

$$m \frac{dv_\theta}{dt} = q(v_z B_r - v_r B_z) - \frac{mv_r v_\theta}{r}, \quad (\text{B-7})$$

$$m \frac{dv_z}{dt} = q(v_r B_\theta - v_\theta B_r). \quad (\text{B-8})$$

Using the second equation, we can change the independent variable from  $t$  to  $\theta$ . Above simultaneous differential equation is solved with Runge-Kutta method. It must be carefully determined how small integral step size should be to keep the desired precision of calculation. Typically, a few ten thousands per cell seems sufficient.

What we do first is to find closed orbit in an iterative way, that is, finding closed orbit by varying particle energy, initial radius and initial angle. Once closed orbit is known, test particle is traced to obtain betatron tune, linear lattice parameter and others.

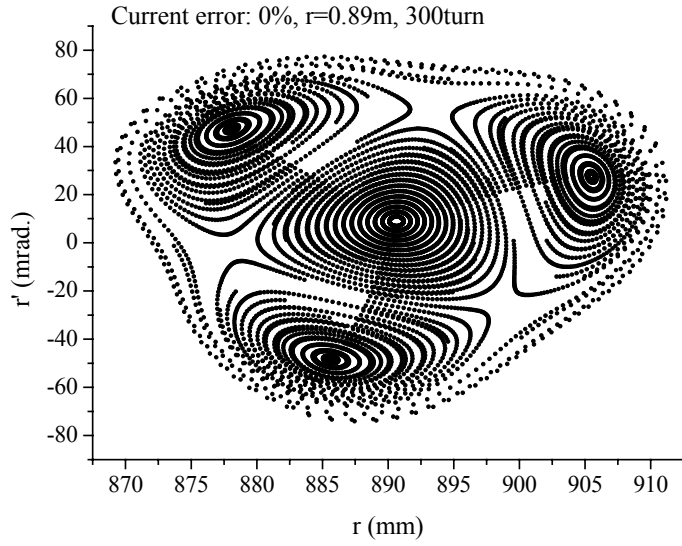
Betatron tune is calculated using Fast Fourier Transform (FFT) analysis of particle position over many revolutions. Since particle position can be recorded whole through a ring, not only fractional part but also the integer part of tune is computed. In order to obtain the tune with a good resolution in short calculation time, “interpolated FFT” is employed [ 33 ].

If necessary, beam acceleration is introduced by step-function energy gain. It can be independent of Runge-Kutta integral. In fact, the process is inserted between integral steps. The step-function energy gain is justified since a length of rf cavity is generally negligible compared with the wavelength of betatron oscillation. (Induction acceleration is excluded here.) Since resonance crossing in FFAG is caused by a dependence of tune upon beam energy, a simulation including acceleration is necessary to study resonance crossing.

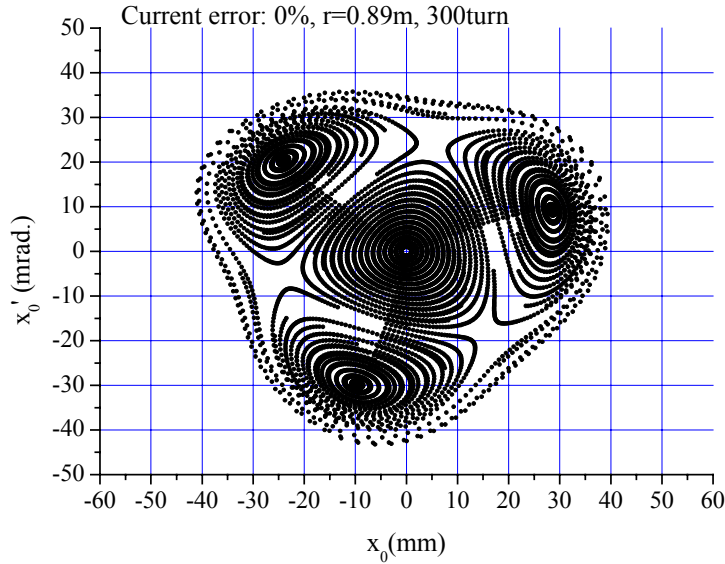
## C Driving term and nonlinear detuning

In order to compute trapping efficiency analytically, driving term and non-linear detuning must be obtained numerically. There are two methods. One is to calculate multipole coefficients directly and integrate them over magnets, and the second method is to locate fixed points in phase space and calculate driving term and nonlinear detuning from them. The first method is straightforward but we employ the second method for the following reasons. It is difficult to estimate multipole coefficient accurately in fringe field area. Furthermore, driving term and nonlinear detuning are not purely determined by sextupole and octupole alone. Driving term may include feed-down contribution from octupole and even higher order components. Furthermore, nonlinear detuning may include the second order effect of sextupole.

The method used in this study is explained for PoP analysis. Using RK tracking described in Appendix C, we find motions in phase space for various initial conditions. Figure C-1 shows a typical result of the calculation.



(a) Motion in  $r-r'$  space



(b) Motion in normalized phase space

Figure C-1. Motions in phase space.

Once fixed points are located, driving term and non-linear detuning can be obtained from the following relations (see also Sec.2.4).

As shown in Tab.2-1, stable and unstable fixed points for  $\xi < 0$  are

$$\alpha_s^{1/2} = \frac{3}{8\kappa} \left( 1 + \sqrt{1 - \frac{32\kappa}{9}\xi} \right), \quad (\text{C-1})$$

$$\alpha_u^{1/2} = \frac{3}{8\kappa} \left( -1 + \sqrt{1 - \frac{32\kappa}{9}\xi} \right). \quad (\text{C-2})$$

By subtracting Eq.( C-2 ) from ( C-1 ),

$$\alpha_s^{1/2} - \alpha_u^{1/2} = \frac{3}{4\kappa}. \quad (\text{C-3})$$

we get

$$\kappa = \frac{3}{4(\alpha_s^{1/2} - \alpha_u^{1/2})}. \quad (\text{C-4})$$

$\xi$  can be expressed in terms of  $\kappa$ ,

$$\xi = \frac{9}{32\kappa} \left[ 1 - \left( \frac{8\kappa}{3} \alpha_u^{1/2} + 1 \right)^2 \right]. \quad (\text{C-5})$$

From the definition of  $\xi$ ,  $\Delta_e$  is

$$\begin{aligned} \Delta_e &= \frac{3}{2\xi} \Delta_L \\ &= \frac{3}{2\xi} \left( \frac{7}{3} - v_x \right). \end{aligned} \quad (\text{C-6})$$

where betatron tune  $v_x$  is also found with RK tracking.

Finally,

$$\Delta_{NL} = \kappa \frac{4\Delta_e}{3}. \quad (\text{C-7})$$

If the average beam emittance is given, driving term and nonlinear detuning are determined from the definitions given in Sec.2.4.

## D Beam loss due to residual gas in PoP FFAG

The energy range of PoP is 50 to 500 keV. In this energy range, beam loss by the residual gas is not negligible especially in the vicinity of injection energy. The background vacuum pressure in PoP is about  $1 \times 10^{-7}$  Torr while the pressure during operation is about  $6 \times 10^{-7}$  Torr. Hydrogen from the iron source is the main component of the residual gas during operation. In this energy range, the dominant interaction between proton beam and hydrogen gas is a charge transfer since the cross section of an elastic scattering is negligible compared with that of charge transfer (see [ 32 ]). The cross section of charge transfer is shown in Fig. D-1.

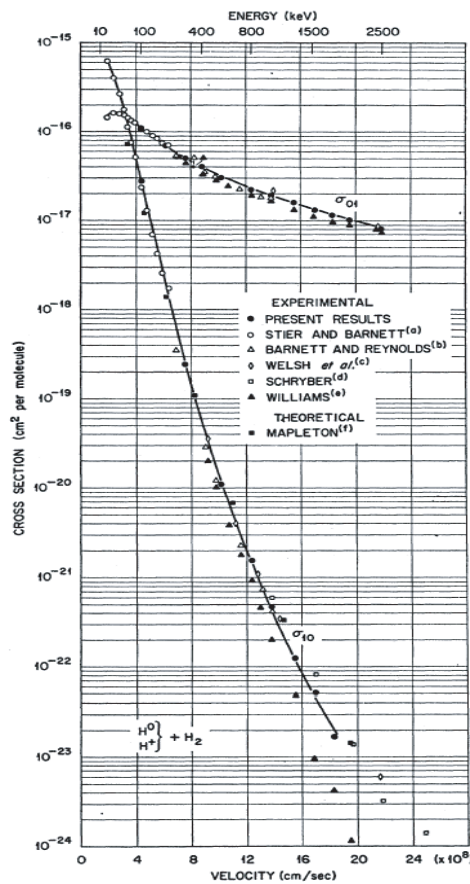


Figure D-1. Cross section of charge transfer (taken from Ref.[ 31 ]).

Through only single interaction of a charge transfer, a particle loses its charge and will be lost. Therefore, the beam emittance does not grow but the beam intensity decreases in this process. For correction, it is sufficient to normalize intensity by the beam loss rate. Specifically, the procedure is to find a suitable fitting function, to apply it to the beam intensity curve and to divide the intensity by the function.

When the beam energy is unchanged, the intensity curve should simply follow an exponential decay. However, the beam is being accelerated and a suitable fitting function is not simply exponential any more. A lifetime of exponential decay depends on beam energy. Therefore the lifetime changes during acceleration and it should be derived as a function of beam energy. Since the beam intensity was obtained as a function of turn number, a function of turn number is more convenient.

The lifetime is inversely proportional to the cross section,

$$\tau \propto \frac{1}{S(n)} , \quad (\text{D-1})$$

where  $S(n)$  is the cross section as a function of turn number  $n$ .

As shown in Fig. D-1, in the energy range of PoP, the cross section is almost proportional to the particle velocity in logarithmic scale, i.e.

$$\ln S = A_1 V , \quad (\text{D-2})$$

where  $S$  is the cross section,  $V$  is the particle velocity and  $A_1$  is a constant.

With non-relativistic approximation, the relation between the particle velocity and energy can be expressed by

$$E_k \approx \frac{1}{2} m V^2 , \quad (\text{D-3})$$

where  $E_k$  is the kinetic energy and  $m$  is the rest mass of proton . The approximation is justified because the energy under consideration is very low.

Beam energy is given by

$$E_k = E_{\text{inj}} + n E_g , \quad (\text{D-4})$$

where  $E_{\text{inj}}$  is the injection beam energy,  $n$  is the number of turns during acceleration and  $E_g$  is the energy gain per turn.

From Eq.( D-2 ), ( D-3 ) and ( D-4 ), we can obtain

$$S = \exp(A_2 \sqrt{E_{\text{inj}} + n E_g}) , \quad (\text{D-5})$$

where  $A_2$  is a constant. The lifetime is then

$$\tau = \frac{A_3}{\exp(A_2 \sqrt{E_{inj} + nE_g})}, \quad (\text{D-6})$$

and the beam intensity can be expressed as

$$I = I_0 \exp\left(-\frac{n}{\tau}\right), \quad (\text{D-7})$$

where  $I_0$  is the initial intensity.

So far, the fitting function is obtained with four fitting parameters ( $P_1, P_2, P_3, P_4$ ),

$$I = P_1 \exp\left[-P_2 n \exp(-\sqrt{P_3 + P_4 n})\right]. \quad (\text{D-8})$$

## E Particle tracking with tune varying transfer matrix

In order to study the dynamics of resonance crossing, a simulation with transfer matrix is employed. The method of simulation for third integer uncoupled resonance is as following.

In one degree-of-freedom, a linear transfer matrix of one cell in which a particle is transferred from  $s_n$  to  $s_{n+1}$  is given by

$$M_Q(s_{n+1}|s_n) = \begin{pmatrix} \cos \mu + \alpha \sin \mu & \beta \sin \mu \\ -\gamma \sin \mu & \cos \mu - \alpha \sin \mu \end{pmatrix}, \quad (\text{E-1})$$

where a length from  $s_n$  to  $s_{n+1}$  is the orbit length of one cell,  $\alpha$ ,  $\beta$  and  $\gamma$  are the linear lattice parameter and  $\mu$  is the phase advance per cell. For simplicity, we set  $\alpha=0(-)$  and  $\beta=1(m)$ .

A driving term and nonlinear detuning are introduced by thin lens sextupole and octupole, respectively,

$$M_S(\hat{s}_n|s_n) = \begin{pmatrix} 1 & 0 \\ K_s x(s_n) & 1 \end{pmatrix}, \quad (\text{E-2})$$

$$M_O(\hat{s}_n|s_n) = \begin{pmatrix} 1 & 0 \\ K_o x(s_n)^2 & 1 \end{pmatrix}, \quad (\text{E-3})$$

where  $x$  is the transverse coordinate,  $\hat{s}_n$  denotes the same position as  $s_n$  that it is downstream of thin lens sextupole or octupole,  $K_s$  is the strength of sextupole field (times the length) and  $K_o$  is the strength of octupole field (times the length).

Octupoles are located in all cells so that one cell matrix including octupole is

$$M_C(s_{n+1}|s_n) = \begin{pmatrix} \cos \mu + \alpha \sin \mu & \beta \sin \mu \\ -\gamma \sin \mu & \cos \mu - \alpha \sin \mu \end{pmatrix} \begin{pmatrix} 1 & 0 \\ K_0 x(s_n)^2 & 1 \end{pmatrix}. \quad (\text{E-4})$$

With this cell matrix, nonlinear detuning is introduced.

Number of cell is set  $N=12$  and resonance of  $3\nu_x=11$  is examined. (It is the same crossing in HIMAC and 150MeV FFAG.) Then  $n$  is from 1 to 12, but when  $n$  is 12,  $n+1=13$  is replaced by  $n+1=1$  to make a closed ring.

Only one sextupole is located in an arbitrary cell. Since Fourier expansion of the delta function (thin lens sextupole) has any order of harmonic components, it introduces the driving terms of 11th harmonics.

We get a transfer matrix for one turn,

$$M_R = M_c^{12} M_s(\hat{s}_e | s_e) , \quad (\text{E-5})$$

where the sextupole is located at  $n=e$  (arbitrary within 1 to 12).

In order to make tune cross resonance, the phase advance  $\mu$  is changed turn-by-turn in above equation.